

Carbon-nanotube enhanced piezoelectric biosensors

Xu, Ting

2010

Xu, T. (2010). Carbon-nanotube enhanced piezoelectric biosensors. Doctoral thesis, Nanyang Technological University, Singapore.

<https://hdl.handle.net/10356/46254>

<https://doi.org/10.32657/10356/46254>

CANBON-NANOTUBE ENHANCED PIEZOELECTRIC BIOSENSORS

XU TING

School of Mechanical and Aerospace Engineering

A thesis submitted to the Nanyang Technological University
in fulfillment of the requirement for the degree of
Doctor of Philosophy

2010

Abstract

Recently, biosensors with high sensitivity, compact size, rapid response and easy operation are urgently required to effectively detect, monitor and control the fast-spreading epidemics, such as influenza A (H₁N₁), dengue fever, bird flu, and hand-foot-and-mouth disease (HFMD). The micro-piezoelectric biosensor is believed to be one of the candidates to fulfill the abovementioned demands due to its compact size, high sensitivity and easy integration with analysis circuit. Among the numerous reports available in the literature, cantilever and quartz-crystal microbalance system (QCMS) type biosensors are found to be the most representative piezoelectric biosensors due to their many advantages such as high sensitivity, label-free detection, robust structure and high reproducibility; however, some drawbacks, including fragile structure, low quality factor and lack of integration limit their applications in monitoring and rapidly detecting the fast-spreading epidemics.

In this thesis, a new type of micro-piezoelectric diaphragm-based biosensor array is presented. Besides the benefits arise from the micro-piezoelectric biosensors mentioned above, this new device is able to simultaneously detect multiple biological materials, which significantly shorten the diagnosis time and lower the cost. In the theoretical analysis part, a novel analytical model for the resonant frequency of a micro-machined piezoelectric diaphragm working in a mixed mode of tension and flexural rigidity is established based on the classic plate theory. The gravimetric and mass sensitivity are derived and the theoretical calculation and finite element analysis results show that the gravimetric sensitivity

is independent of the tension and flexural rigidity and only determined by the total diaphragm thickness. By considering the sensitivity and difficulty of biomaterial immobilization, the designed diaphragm diameter varies from 600 μm to 1000 μm with a thickness of about 1 μm . After the sensor designs based on the theoretical analysis, two novel micro-piezoelectric diaphragm-based sensor chips are then developed in the first part of this project. The first square sensor array with 7 individual sensors with dimension of 500 $\mu\text{m} \times 500 \mu\text{m}$ successfully detect anti-goat immunoglobulin G (IgG) with 7 different concentrations. The gravimetric and mass sensitivity are calculated to be $-16.5 \text{ m}^2/\text{kg}$ and 6.25 Hz/ng , respectively. To increase the mass sensitivity and fabrication yield of the piezoelectric biosensors, the second circular-type sensor array is developed and demonstrated to be able to simultaneously detect HBsAg, AFP and HBcAg. A real determination of HBsAg and AFP with the limit of detection of 0.1 ng/ml in the concentration range of 0.1 to 10000 ng/ml can be confirmed by this immunochip. The mass sensitivity for detection of HBsAg and AFP are found to be 16.05 Hz/ng and 15.97 Hz/ng , respectively. Both the gravimetric ($-45.33 \text{ m}^2/\text{kg}$) and mass sensitivity are more than two times higher than those obtained from the square sensor array. These preliminary results confirm the possibility of applying these piezoelectric sensors for biosensing.

To further improve the mass sensitivity of the developed sensor array chip, the sensing surfaces are covered by carbon nanotubes (CNTs). CNTs possess very high specific surface areas and can capture more analytes to improve detection signals. As a result, the sensitivity and dynamic range of detection can be greatly increased. Hence, in the second part of this project, CNTs were incorporated with the

piezoelectric diaphragm to develop a CNT-enhanced mass-sensitive biosensor. After a systematic and comprehensive optimization on the influences of various synthesis parameters, a high quality of long CNT with length up to 380 μm was successfully synthesized.

Development of CNT-enhanced piezoelectric biosensors was implemented in the following two approaches. CNTs can be either directly grown or deposited onto the diaphragm to enhance the performance of the biosensors. In the first experiment, CNTs are directly grown on the reverse side of the sensor diaphragm; unfortunately, most of the sensors are damaged due to the high CNT growing temperature. Thus, in the second experiment, CNTs are pre-synthesized and deposited onto the sensing surface of the individual sensors. The developed CNT-incorporated immunochip is able to simultaneously detect anti-goat IgGs with 8 different concentrations and possess a detection limit of 0.1 ng/ml and a dynamic range of 0.1 to 10000 ng/ml; whereas the detection limit and dynamic range for a non-CNT enhanced immunosensor chip are 1 ng/ml and 1 to 10000 ng/ml, respectively. More importantly, the mass sensitivity of a CNT incorporated biosensor is nearly 4 times higher than that without CNT enhancement. The results demonstrate that the developed CNT-enhanced piezoelectric biosensor array has significant advantages over the conventional one. Moreover, the developed biosensor chip has more robust structure, high fabrication yield and high quality factor comparing with the micro-piezoelectric cantilever biosensors; its limit of detection is hundred times higher than the QCMS. The key advantage of the developed CNT-enhanced piezoelectric biosensor array lies in its multiple detection capability with high sensitivity; the diagnosis speed can be at least 8 times faster than the normal cantilever biosensor

Abstract

and QCMs. Furthermore, the undesired cross interactions between the biological materials caused by human errors can be maximally avoided because of the integrated diagnose processes; hence, the accuracy and reliability of the test results are increased. The preliminary results achieved in this project indicate that the CNT enhanced micro-machined piezoelectric diaphragm-based biosensor array has very compact size, high sensitivity, high quality factor, rapid response and multiple detection capability. With further calibration and optimization, it can be potentially used as low cost disposable immunosensor.

Acknowledgement

I would like to express my most sincere gratitude to all the individuals who have helped make this work possible. It is accomplished with the support of many people, who were indispensable for the realization of this thesis.

First of all, I offer my deepest gratitude and appreciation to my advisor, Professor Miao Jianmin for his trust towards me. With his deep understanding and continuous encouragement, my ever-ignored potential, both in research and daily life, has been explored. From a research perspective, his strong and sensitive feel in research provided us a long-term vision and many creative ideals to solve the technical problems encountered. I would also like to thank him for his hands-free training, in which I can work independently and freely to implement my ideas together with his sufficient research budget. Lastly, his positive thinking and hardworking style have greatly influenced my approach towards the research, as well as my life.

I would like to thank my co-supervisor Professor Li Changming for his invaluable suggestions and guidance in this project. His expertise in biosensor design and immobilization were very helpful. I also appreciate his partial financial support for this project.

I also wish to express my gratitude and indebtedness to Dr Wang Zhihong for his endless patience and invaluable teaching, vast knowledge and supervision on making this project a smooth one. His willingness to share every bit of his knowledge has been of tremendous assistance and help.

Acknowledgement

Special thanks would be given to Dr. Yu Ling and Mr. Liu Yingshuai for their kind assistances in the bio-immobilization part in this project.

I am grateful to Mr. Tan Chee Wee for his efforts in reviewing my journal papers and thesis.

I would like to thank my classmate Mohammad Olfatnia, for the valuable discussion and kindly help for the model analysis and theoretical calculations.

I also have to recognize the much-appreciated assistance given to me by Dr. Chen Xiaofeng, Dr. Pradeep Dixit, Mr. Naylin, Mr. Tan Chong Wei, Mr Pek Soo Siong, Mr Ho Kar Kiat, Mr Wong Kim Chong, Mr Hoong Sin Poh, Mr Nordin Abdul Kassim, and all those who have given me unending support and encouragement throughout the project.

Finally my special gratitude is towards my parents and my wife, for their love, encouragement and support throughout my research duration. Without them, I would not be able to conduct my project smoothly. I also thank my lovely son and daughter for bringing me every enjoyable moment.

Contents

Abstract	i
Acknowledgements	vii
Contents	viii
List of figures	xii
List of tables	xix
List of abbreviations	xx

Chapter 1 Introduction

1.1 Background	1
1.2 Motivations	4
1.3 Objective	5
1.4 Organization of the thesis	6

Chapter 2 Literature Review

2.1 Biosensors	9
2.1.1 Bio-recognition molecules	11
2.1.2 Immobilization techniques	12
2.1.3 Transducers	14
2.2 Carbon nanotubes	23
2.2.1 Physical structure of CNTs	24
2.2.2 Synthesis of CNTs by chemical vapor deposition.....	25
2.2.3 CNT Properties.....	29

Contents

2.2.4	Biological applications of CNTs	31
2.3	Proposal for CNT enhanced piezoelectric biosensors	35
2.4	Summary of this chapter	35

Chapter 3 Biosensor Design and Simulation

3.1	Sensor design and working principle.....	39
3.2	Sensor vibration analysis	41
3.2.1	Resonant frequency for circular diaphragm based sensor	42
3.2.2	Resonant frequency for square diaphragm based sensor	47
3.3	Sensitivity of the diaphragm based sensors	50
3.3.1	Gravimetric sensitivity.....	50
3.3.2	Mass sensitivity	52
3.4	Summary of this chapter	59

Chapter 4 Micro-machined piezoelectric diaphragm based immunosensor array

4.1	Background of bulk micromachining	60
4.2	Square biosensor array.....	62
4.2.1	Fabrication processes.....	62
4.2.2	Fabrication results	65
4.2.3	Biomaterial immobilization	66
4.2.4	Characterization of the immunosensor array	71
4.3	Circular biosensor array.....	80

Contents

4.3.1	Fabrication processes.....	80
4.3.2	Fabrication results	82
4.3.3	Immobilization of antigens	83
4.3.4	Characterization.....	84
4.4	Summary of this chapter	91

Chapter 5 Synthesis of Carbon Nanotubes by Thermal Chemical Vapor Deposition

5.1	Introduction	93
5.2	Experimental details	94
5.2.1	The influence of catalyst thickness and annealing time on CNT growth	97
5.2.2	The influence of temperature on CNT growth.....	103
5.2.3	The influence of growth time on CNT growth.....	108
5.2.4	The influence of gas flow rate on CNT growth	110
5.2.5	The influence of pressure on CNT growth	113
5.3	Optimized results.....	116
5.4	Summary of this chapter	119

Chapter 6 Development of CNT enhanced piezoelectric biosensor array

6.1	Introduction.....	121
6.2	Development of piezoelectric diaphragm biosensor with CNT growth.....	123
6.2.1	Fabrication processes	123
6.2.2	Device structure	125

Contents

6.2.3	Characterization of PZT diaphragm.....	126
6.2.4	Synthesis of CNT on PZT diaphragm.....	128
6.3	Development of piezoelectric diaphragm biosensor with CNT deposition	132
6.3.1	Device fabrication.....	132
6.3.2	Characterization of the sensor array.....	134
6.3.3	Optimizing immobilization method.....	136
6.4	Summary of this chapter.....	157

Chapter 7 Conclusions and Recommendations

7.1	Contributions.....	159
7.2	Future work recommendations.....	163

References	165
-------------------------	-----

Publication List	182
-------------------------------	-----

List of Figures

Figure 2. 1 Schematic of the basic components inside a biosensor	10
Figure 2. 2 Sketch of a biosensor utilizing enzymes as the specific receptor	10
Figure 2. 3. Typical schematic diagram of antibody composed of two heavy chains and two light chains	12
Figure 2. 4. Scheme of cantilever biosensors. The left one was bent due to the mass of the targeted biomolecules captured by the immobilized receptors	17
Figure 2. 5. SEM image of a classic piezoelectric cantilever ..	18
Figure 2.6. Sketches of a typical QCM sensor, a) overall view, b) cross sectional view	19
Figure 2. 7. (a) Schematic side-view of a thin film membrane (b) and its vibration behavior	21
Figure 2. 8. Piezoelectric diaphragm type biosensor array	22
Figure 2.9. Structure of SWCNT and MWCNT. (a) Model of single-walled carbon nanotube (SWCNT) formed from a rolled up sheet of grapheme, (b) Schematic diagram of a multi-walled carbon nanotube (MWCNT) obtained by rolling sheets of graphene and nested concentrically	25
Figure 2. 10. Schematic of root and tip growth mechanism	26
Figure 2. 11. Schematic diagram of thermal CVD apparatus	27
Figure 2. 12. Schematic diagram of PECVD apparatus	29
Figure 2. 13. Nanoforest of vertically aligned CNT trees acting as molecular wires	32
Figure 2. 14. Schematic picture of two electrodes connecting a semiconducting SWCNT with GOx enzymes immobilized on its surface	33

List of Figures

Figure 4.5. Equipment setup for measuring the resonant frequency. (a) A probe station with microscope, (b) the enlarged view of the sensor chips with connection to the two probes, (c) an Agilent 4294A impedance analyzer.	72
Figure 4.6. Frequency change of sensor 1 after goat IgG & blocker and anti-goat IgGs were immobilized or captured.	73
Figure 4.7. Relationship between frequency depression, concentration of goat IgG and mass change, (a) Relationship between the frequency depression and the concentration of goat IgG, (b) Relationship between the mass change and frequency depression after the anti-goat IgGs were captured.	78
Figure 4.8. Schematic fabrication process for the circular piezoelectric sensor.	81
Figure 4.9. Optical images of a sensor array. (a) Front view. (b) Backside view.	82
Figure 4.10. Fluorescent image of the reverse side of the sensor array after capturing the specific antibodies. Sensors 1 & 2, 3 & 4 successfully captured anti-HBsAg and anti-AFP.	85
Figure 4.11. Frequency spectrum of the sensor 2. The frequency continues shifting from depositing gold layer to adding anti-HBsAg.	86
Figure 4.12. Detailed frequencies of the sensors in the immunochip after each immobilization process.	87
Figure 4.13. Calibration curve for detecting of HBsAg and AFP with similar immunochips.	89
Figure 5.1. Sketch of synthesis of CNT through TCVD, (a) wafer preparation, (b) SiO ₂ film deposition, (c) deposition of Fe catalysis by E-beam evaporation, (d) CNT growth by TCVD.	95
Figure 5.2. Sketch of CNT growing process.	95

List of Figures

Figure 5.3. Morphology of the catalyst layer after annealing for 15 min with different thickness and temperatures. (a)-(c) shows the pictures of the catalyst film with thickness of 2, 5 and 10 nm at temperature of 700 °C.98

Figure 5.4. SEM images and 3D AFM images (the inserted images) of the catalyst surface (a) before annealing pretreatment and after annealing pretreatment at 700 °C for (b) 5min, (c) 10 min, (d) 15min, (e) 20 min, (f) 25 min, (g) 30min and (h) 45min.100

Figure 5.5. Mean diameter of particle on substrate surface as a function of annealing pretreatment time t_1101

Figure 5.6. High magnification SEM images shows the CNT density grew with different catalyst pretreatment time (a) 10 min, (b) 20 min and (c) 30 min.102

Figure 5.7. Cross section SEM images of CNT at different growth temperatures, (a)-(h) are 650, 700, 725,750,800,850 and 900 °C, respectively. The last two image (h-i) are the enlarged view of CNT growth at temperature of 700 and 900 °C..... 104

Figure 5.8. Raman Spectrum of CNT for different growth temperatures.107

Figure 5.9. Peak intensity Raman ratio I_G/I_D as a function of growth temperatures.107

Figure 5.10. CNT length as a function of growth time at 725 °C. (10min).....109

Figure 5.11. Peak Raman intensity ratio I_G/I_D as a function of growth time t_2 at 725 °C. The growth time varies from 5 to 80 min.110

Figure 5.12. CNT length as a function of C_2H_2 flow rate at 725 °C.112

Figure 5.13. Raman intensity ratio as a function of different C_2H_2 flow rate at 725 °C.....113

Figure 5.14. CNT length as a function of growth pressure.....114

List of Figures

Figure 5.15. Raman intensity ratio I_G/I_D as a function of growth pressure.	116
Figure 5.16. SEM and TEM images of aligned long CNT growing based on optimized parameters. (a) SEM image of long CNTs up to 381 μm , (b) close up view of the dense CNT, (c) TEM images of one single multi-walled CNT, the inset image shows the detailed structure, (b) two single CNTs with catalyst located at the tips.	118
Figure 5.17. Raman spectrum of the grown CNTs based on the optimized parameters.	118
Figure 6.1. Sketch of the sensing platform for attaching molecules. (a) Plain surface, (b) CNT modified surface.	122
Figure 6.2. Schematic diagrams of fabricating the piezoelectric diaphragm and growing CNTs.	124
Figure 6.3. SEM images of the fabricated device, (a) top view of the device, (b) backside view of the reaction chamber, (c) detailed cross sectional view of the PZT diaphragm structure.	126
Figure 6.4. Characterization of the PZT film on the device, (a) P-E hysteresis loop of the PZT diaphragm, (b) the Q factor is as high as 219 at relatively low operating frequency.	127
Figure 6.5. A set up diagram for growing CNTs on the backside of PZT diaphragm inside quartz tube.	128
Figure 6.6. SEM images of the PZT diaphragm with CNTs, (a) backside view of PZT diaphragm, (b) a close-up view of bottom surface of the deep hole, (c) cross section of the PZT diaphragm with CNTs, (d) PZT film together with top electrode was peeled off.	130

List of Figures

Figure 6.7 Pictures of the fabricated sensor array with different top electrode shape.
 (a) Solid top electrode, (b) Small solid electrode, (c) Ring shaped electrode. 133

Figure 6.8 Relationship between the sensor resonant frequency and the diaphragm diameter. 134

Figure 6.9. Sketched process flow for immobilization of GPTS [154]. (a) plain silicon substrate with SiO₂ film, (b) H₂O₂/H₂SO₄ treatment brings Si-OH groups onto silica surface, (c) GPTS covalently bond to the oxide surface and cross-link the silane groups after thermal curing, (d) goat IgG bond to the GPTS coated surface through the open epoxy ring, (e) blocker blocks the open space on the substrate, (f) anti-goat IgG couples with goat IgG. 138

Figure 6. 10. Fluorescence images for the three sensors with different buffer layers.
 Left: GPTS, Middle: PEI and Right: Plain surface. 140

Figure 6.11 Pictures of CNTs solution. a) Un-dispersed CNTs in HNO₃ solution for 1 h, b) GPTS functionalized CNTs after 10 min of sonication, c) uniformly dispersed CNT solution after the complete sonication and stirring process. 141

Figure 6. 12. Sketched immobilization processes for the CNT enhanced PZT biosensor. 143

Figure 6. 13. SEM images of one reaction chamber, (a) before CNT deposition, (b) after CNTs deposition, (c) enlarged image of the deposited CNTs. 144

List of Figures

Figure 6.14. FSEM and TEM images of the functionalized CNTs. (a) & (c) are the images of acid pre-treated CNTs, (b) & (d) are the images of CNTs immobilized with goat IgGs. 144

Figure 6.15. AFM image CNTs across immobilization stages. Stages 0-IV are representing CNT, CNT+GPTS, CNT+GPTS+goat IgG, CNT+GPTS+goat IgG+blocker and CNT+GPTS+goat IgG+blocker+anti-goat IgG, respectively. The last picture shows the CNT diameter measurement. 145

Figure 6.16. Average CNT diameter at different immobilization stages. 146

Figure 6.17. Raman spectrum of the CNTs across biomaterial immobilization stages. 147

Figure 6.18. Peak intensity Raman ratio across biomaterial immobilization stages..... 150

Figure 6.19. ATR-FTIR spectrum across different biomaterial immobilization stages, (a) acid treated CNT, (b) CNTs coated with GPTS, (c) goat IgG bond onto the GPTS draft CNT, (d) blocker added into CNT-GPTS-IgG composite, (e) anti-goat IgG captured by CNT composite..... 153

Figure 6.20. Detailed frequency shift of the two sensor array (a) without CNTs, (b) with CNTs after each immobilization processes. 155

Figure 6.21. Relationship between the frequency depression (Hz) and concentration of the added anti-goat IgG (ng/ml). C1 to C8 represents the concentrations of 0, 0.1, 1, 10, 100, 1000, 10000 and 100000 ng/ml, respectively. 156

List of Tables

Table 3.1 Values of λ^2 for an edge clamped circular diaphragm	41
Table 3.2 Values of α^2 for an edge clamped circular diaphragm	42
Table 3.3 Frequency parameters $(\gamma_{1mn}a)^2$ for a fully clamped circular or square plate	47
Table 3.4 Materials properties and theoretical mass sensitivity	53
Table 3.5 The first four vibration mode of the circular diaphragm.....	55
Table 3.6 Mass sensitivity of the sensors obtained by theoretical calculation and FEA simulation	56
Table 5 1: Synthesis parameters for the series of experiments.	96
Table 5 1: Synthesis parameters for the series of experiments.	96
Table 5 2: Optimum Parameter from each set of experiment.	117
Table 6. 1 Summary table of D-Band and G-Band across biomaterial immobilization stages.	148

List of Abbreviations

AFM	Atomic Force Microscope
AFP	α -fetoprotein
CNT	Carbon Nanotube
CVD	Chemical Vapor Deposition
DRIE	Deep Reactive Ion Etching
ESR	Electron Spin Resonance
GPTS	3-Glycidoxypropyl-trimethoxysilane
HBV	Hepatitis B Virus
HMDS	Hexamethyldisilazane
IPA	Isopropyl – alcohol
IgG	Immunoglobulin G
MEMS	Micro-Electro-Mechanical Systems
MWCNT	Multi-wall Carbon Nanotube
PECVD	Plasma Enhanced Chemical Vapor Deposition
PEI	Polyethyleneimine
QCMS	Quartz Crystal Microbalance System
RIE	Reactive Ion Etching
SCCM	Standard Cubic Centimeters per Minute
SEM	Scanning Electron Microscope
SWCNT	Single-Walled Carbon Nanotube
SOI	Silicon-on-insulator
TBS	Tri-buffered-saline
TEM	Tunneling Electron Microscope

Chapter 1

Introduction

In this opening chapter, the background of biosensors, including configuration, classification and research trend, is briefly introduced. Special attention is focused on the microfabrication technology and micro-piezoelectric biosensors. Extraordinary properties of carbon nanotubes used to enhance the sensitivity of the biosensor are also discussed shortly. The motivation and the objectives of this research study are briefly explained. At the end of the chapter, the organization of this thesis is presented.

1.1 Background

It is believed that global warming and pollution have resulted in many new diseases every year. In year 2003, severe acute respiratory syndrome (SARS) was overspreaded in Asia and caused a serious impact on the region's economics and societies. Afterwards, other new diseases, like bird flu, dengue fever and hand, foot & mouse disease spread widely in Southeast Asia. Most recently, influenza A (H₁N₁) is tyrannizing worldwide. Millions of peoples were infected and thousands of them were dead. These highly infection diseases are seriously threatening the population's safety if they are not detected immediately for effective control. With

this regard, biosensors with high sensitivity, compact size, rapid response, and easy operation are urgently required.

A biosensor generally consists of a transducer and an affinity-based sensing interface. After the interested biological analytes are interacted with the receptors, which are bounded onto the interface, some biological, chemical and physical properties of the receptors or analytes change due to the biological interactions. The transducer then converts the changes into readable signals (i.e. current, voltage, resistance, pH value and optical image, et al) and transfers them into a computer or other analysis system [1].

Based on the working principles of the involved transducers, biosensors can be categorized into electrochemical, optical, piezoelectric and thermal types. Electrochemical biosensors are the widely used sensing devices up to date; however, their reliability and accuracy can be easily affected by the liquid properties, such as pH values, flow rates and concentrations [2]. The optical biosensor is also another important device. The main drawbacks of this powerful technique lie in its complexity of the testing, high cost and large size of equipment [3,4]. The extensively applications of thermal biosensors are limited by the long measurement process [5]. The piezoelectric biosensors are usually mass-sensitive and the fabrication of piezoelectric transducers is compatible with Microelectromechanical System (MEMS) process, hence their sizes can be miniaturized and suit demands of rapid response, high sensitivity, small size, and easy operation [6]. Therefore, in this project, the possibility of utilizing piezoelectric mass micro-sensors as biosensors will be investigated.

MEMS is a revolutionary manufacturing technology, which is a new way of making complex electromechanical systems using batch fabrication techniques. It is similar to the way that integrated circuits (ICs) are fabricated and fabricating these electromechanical elements along with electronics. A linguistic examination of the MEMS acronym reveals the key words of “micro”, which demonstrates the advantages gained by size downscaling. The smaller size of the devices and the fewer components of a system can lead to lesser power consumption and higher reliability. Additionally, the integrated functions make MEMS devices more powerful [7]. By using MEMS technology, piezoelectric micro-biosensor will be fabricated in the first stage of this project; CNTs will be incorporated with the piezoelectric sensor to further enhance its sensitivity at the end of this project.

Intensive research interests have been paid to CNTs due to their excellent mechanical, electrical, thermal and bio-chemical properties [8-10]. These remarkable properties have led to a wide range of potential applications including nanoelectronics, quantum wire interconnects, chemical and biological sensors, ceramic or metal composites [11,12]. One of the extraordinary features of CNTs would be their extremely high specific surface areas, which are ranked the highest among all nanomaterials [11-13]. If CNTs are incorporated onto the solid plain surface to form a 3 dimensional (3-D) sensing interface, comparing with the plain sensing surface, a much larger amount of probe molecules are immobilized on the CNT surfaces and interact with the target analytes at the same concentration. Therefore, CNTs served as an amplifier to enhance the output signals; as a result, the sensitivity and the limit of detection will be dramatically increased [14].

1.2 Motivations

Among the micro-machined piezoelectric biosensors, quartz crystal microbalance (QCM), micro-cantilever biosensor and micro-diaphragm based biosensor attract much of the research attention. QCM is widely used because of its robust nature and affordable electronics. With the increasing interest to single cell sensing or testing over the last decades, micro-cantilever and micro-diaphragm biosensor have received much research interest because they are superior to QCM both in mass sensitivity and sensor size [1,15,16]. Micro-cantilever biosensor offers many advantages over other sensors, such as compact size, small active area and easy integration with electronic circuit. More importantly, micro-cantilever biosensor is able to detect extremely light mass (e.g. a single bacterium or spore) due to its designed structure. However, it suffers from low quality factor (Q factor) in liquid media. Additionally, extensive use of such sensors in real operating condition could be limited by their fragility and packaging difficulty. In contrast, piezoelectric micro-diaphragm based biosensor is more durable and has relatively higher Q factor than micro-cantilever biosensor. It also has a very simple diaphragm structure which consists of a thin piezoelectric film and two metal electrodes. This diaphragm together with another thin layer forms a bimorph structure during the vibration. The micro-diaphragm biosensor utilizes a bulk acoustic standing wave formed between the two electrodes which is similar to the QCM. In other word, it uses the thickness vibration mode of the diaphragm. The micromachined diaphragm is usually a composite structure with a support layer; a flexural resonant mode is easy to be excited and utilized. As such, in this project, we investigated the

feasibility of using the flexural vibration mode of the micromachined diaphragm as a mass sensitive biosensor.

1.3 Objectives

The main objectives of this project can be summarized in the following points:

- Theoretically analyze the vibration behavior of the micro-diaphragm and establish the governing equation for its resonant frequency in a mixed mode of tension and flexural rigidity.
- Define the mass sensitivity of the micro-diaphragm based biosensors. To investigate the relationship between the sensitivity, sensor working mode and the sensor geometry parameters.
- To develop two novel piezoelectric diaphragm-based mass sensor arrays using MEMS technology. The first square sensor array needs to be fabricated and characterized to confirm the possibility of applying these piezoelectric sensors for biosensing. Based on the optimized process parameters from the first sensor, the second circular-type sensor array will be developed to further enhance the performance, such as sensitivity, limit of detection and the sensor fabrication yield.
- To synthesis CNTs by thermal chemical vapor deposition (TCVD) and conduct a systematic and comprehensive study on the influences of various synthesis parameters, such as pressure, process gas flow rate, growth temperature, growth time, catalyst pretreatment time and catalyst thickness, on the vertical length and quality of CNTs. All the parameters will be optimized through the

experiments to grow long CNTs with good purity.

- To develop CNT enhanced piezoelectric biosensors by two novel approaches. In the first approach, CNTs will be directly synthesized from the reverse side of the sensor diaphragm by TCVD with the optimized parameters. In the second approach, CNTs will be pre-synthesized and functionalized. Afterwards, the prepared CNTs will be applied into the reaction chambers in the sensors for the bio-immobilization. Both methods will be implemented and optimized to achieve a best performance of the micro-piezoelectric biosensors.

1.4 Organization of the thesis

This thesis comprises six chapters and the organization of the report is presented as follows:

Chapter 1 is the introductory chapter with a brief introduction of the research background and motivations of the project followed by the objectives and the organization of the thesis.

Chapter 2 presents literature review on the fundamental knowledge of biosensors, including the working principles and classifications. As the focus of this research, the reviews on piezoelectric type biosensors are emphasized. The micro-piezoelectric biosensors, including QCM, micro-cantilever, and micro-diaphragm biosensors are introduced and compared. In this chapter, reviews on CNT properties and synthesis methods are also included. The sensor designs are proposed at the end of this chapter.

Chapter 3 gives the theoretical analysis for the piezoelectric diaphragm based biosensor. The resonant frequency governing equations for sensor working in the mixed mode of stress and flexural rigidity are established. Gravimetric and mass sensitivity of the sensor are defined. Diaphragm size and thickness are found to be the two dominant factors to affect the gravimetric sensitivity and their relationships are also investigated in this chapter.

Chapter 4 describes the developments of new micro-piezoelectric diaphragm based biosensor arrays. The detailed fabrication processes for the square and circular type biosensors are presented and the different bio-immobilization processes are also illustrated. Characterization results demonstrate that the developed mass sensors can be potentially applied as immunosensors.

In Chapter 5, influences of CNT synthesis process parameters including pressure, process gas flow rate, growth temperature, growth time, catalyst pretreatment time and catalyst thickness on the CNT length and quality are systematically investigated and optimized through TCVD. The optimized parameters are used for synthesizing long CNTs with good quality for biological applications.

Chapter 6 presents two novel methods to develop CNT incorporated micro-piezoelectric diaphragm based biosensors. In the first demonstration, CNTs are directly grown on the reverse side of the piezoelectric diaphragm; unfortunately, the diaphragm is damaged due to the high CNT growing temperature. As an alternative, pre-grown CNTs are deposited onto the diaphragm surface and bio-immobilization are implemented. Results show that the sensitivity of a CNT-incorporated biosensor is nearly 4 times higher than that without CNTs enhancement.

Chapter 7 concludes the thesis with summary of the research work and achievements have been accomplished. Recommendations for future research in this project are also included.

Chapter 2

Literature Review

A detailed review of biosensors and CNTs is presented in this chapter. The working principle of biosensor, bio-recognition element and immobilization techniques are introduced. Since piezoelectric biosensors are the research focus in this project, the advantages and disadvantages of quartz crystal balance biosensor, piezoelectric cantilever and diaphragm biosensor are discussed. As CNTs will be incorporated with piezoelectric diaphragm based biosensors to enhance their sensitivity and detection limit, the structures, synthesis methods and properties of CNTs are also summarized. In the last section of this chapter, the design of a CNT enhanced piezoelectric biosensor is proposed.

2.1 Biosensors

A biosensor is an analytical instrument that works by incorporating specific biological materials and a transducer [17,18]. As illustrated in Figure 2. 1, recognition molecules and transducers are the two main components in a biosensor. Molecular recognition of specific analytes brings about physical or chemical parameters changes (e.g. changes of ions, electrons, mass, heat or light). Transducers then detect the changes and convert them into readable signals, such as current, voltage, pH values, etc. After amplification and filtering, the signals are transferred to computer or any other system for the analysis [19-21].

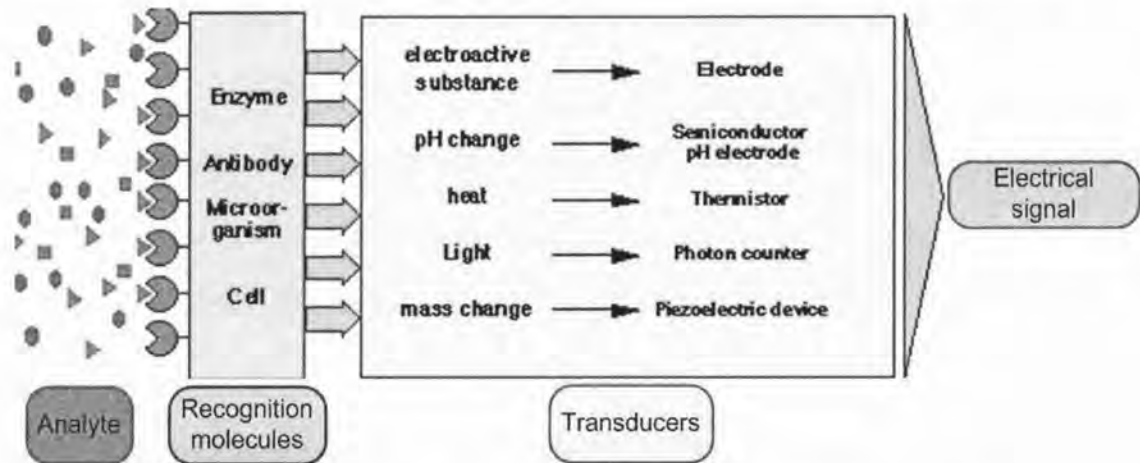


Figure 2. 1. Schematic of the basic components inside a biosensor [21].

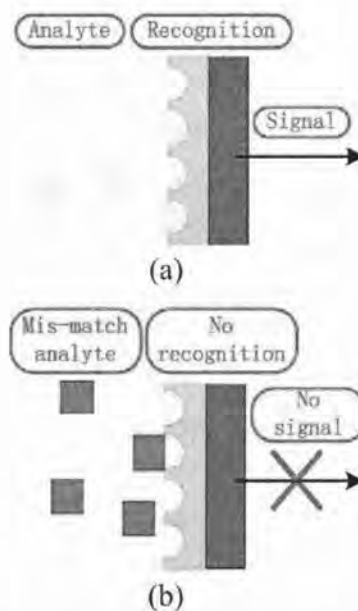


Figure 2. 2. Sketch of a biosensor that utilizes enzymes as the specific receptor [22].

One sketch of biosensor using enzyme as the receptor is depicted in Figure 2. 2 and it can be seen that only when the specific analytes reach the recognition receptors, the coupling effect takes place and causes the physical or chemical changes, which are eventually converted into readable signals by the transducer (Figure 2. 2 a). Otherwise, if there is no match between the non-specific analytes

and the receptor, the coupling effect will not occur and no signal will be generated (Figure 2. 2 b).

Biosensors can be classified into many types according to the used bio-recognition components, immobilization techniques and transducers. Each of them will be discussed in detail in the following sections.

2.1.1 Bio-recognition molecules

Bio-recognition molecules can be classified into catalytic and affinity type. Catalytic biorecognition molecules act as catalysts in the chemical reactions but remain unchanged at the end of the reaction. Enzymes and microorganisms are the commonly used biorecognition protein molecules and the analytes used are usually small organic molecules like glucose.

Affinity bio-recognition molecules utilize antibodies, DNA, peptides and lectins as biorecognition molecules and the analytes are bonded to these molecules without further reaction. As compared to catalytic biosensors, affinity biosensors have a wider range of compatibility as it is able to virtually detect all biological agents [23,24]. Hence, affinity biosensors will be developed in this research and antibody will be used as the biorecognition molecules. Antibody (Ab) is high-molecular weight soluble protein produced by an organism to fight against antigen (Ag). Antibody molecules consist of two light (L) and two heavy (H) polypeptide chains by disulfide bonds, and each has variable (V) and constant (C) portions [25]. As shown in Figure 2.3, the antibody molecule has a “Y” shape where two antigen binding sites are located on the upper parts of the antibody. The Ag-Ab reaction is

one of a key fits into a lock effect, which is formally known as specificity. It refers to the ability of an individual antibody combining site to react with only one antigenic determinant. There is generally a high degree of specificity in antigen-antibody reactions. Antibodies can only distinguish differences in the primary structure of an antigen, isomeric forms of an antigen, and secondary and tertiary structure of an antigen. The key-lock bond is non-covalent in nature, in which multiple bonding, such as hydrogen bonds, electrostatic bonds, Van der Waals forces and hydrophobic bonds, between the antigen and the antibody ensure that the antigen will be bound tightly to the antibody [26, 27].

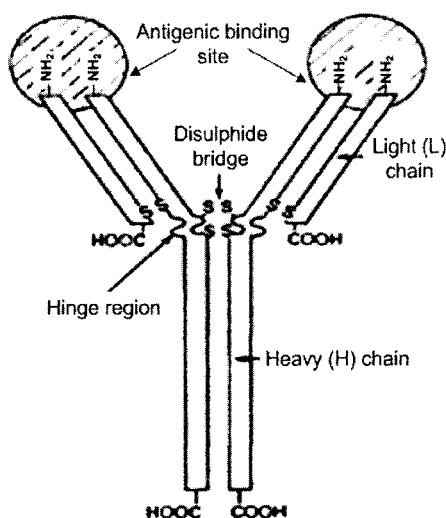


Figure 2. 3. Typical schematic diagram of antibody composed of two heavy chains and two light chains [27].

2.1.2 Immobilization techniques

The choice of appropriate mode of immobilization is important for a biosensor as it will affect the reliability and accuracy of the measurement results. Generally, the bio-immobilization technique can be widely categorized into non-covalent and

covalent type. By using non-covalent techniques, the molecules are absorbed onto the solid sensing interface via weak physical or chemical interactions, such as ionic, hydrogen bonding, static force. Although the natural conformation and the activity of the molecules are preserved, the absorbed molecules are easily desorbed due to the changes in external conditions [28,29]. For example, during the washing process, the molecules absorbed via Van Der Waals forces may drop off the sensing surface because of the weak interaction. However, due to its simplicity, this method will be implemented in the first stage of this project.

The covalent immobilization technique offers higher stability and longer active lifetime of the absorbed molecules as compared to the non-covalent method. In the covalent immobilization method, the proteins are attached onto the solid substrate through certain functional groups in the carriers or the modified surface. The covalent binding is strong and the reaction conditions are usually relatively complicated.

There are two approaches to attach the proteins onto the sensing surface in a transducer through covalent bindings. The first one is to directly attach the proteins onto special solid sensing surfaces (e.g. graphite, glass and gold), which need to be oxidized to obtain highly reactive sites, such as carboxy, phenol, and quinone structures. The normally used oxidation techniques include heat, oxygen radio frequency plasma etching, and electrochemical oxidation. The oxidized surface is then ready for the attaching of proteins. In some cases, a spacing molecule is needed on top of the oxidized surface to avoid protein fouling [29,30].

In another approach, the proteins are bound to the solid surface via a carrier which can be controlled porous glass, colloidal gold particles, agarose, nylon or

polyacrylamide. These activated carriers generally contain amino-, aldehyde-, carboimido-, thiol-, diazonium- or other reactive groups to react with functional groups from proteins. Two steps are usually involved in this binding. Solid surfaces, such as glass, quartz and platinum are firstly activated by silanization. Afterwards, proteins or other molecules are bonded with the modified carriers. Although this technique is relatively complex and time consuming, it is still the most commonly used approach for protein immobilization due to its high stability and reliability. Hence, this immobilization technique will be implemented in the later stage in this project [31, 32].

2.1.3 Transducers

Transducers are the crucial elements in the analytical instrument as they link the biological system and the electrical system of the biosensor. There are a few different physical and chemical transduction modes for the biosensor to examine the biological recognition process. Based on the working principle of the involved transducers, biosensors can be categorized into electrochemical, optical, piezoelectric and thermal type.

(i) Electrochemical biosensors

Many chemical reactions produce or consume ions or electrons, which cause some change in the electrical properties of the solution that can be sensed and used as measuring parameters. The electrochemical biosensors can be further categorized as: (1) Conductimetry: measuring the electrical conductance (resistance) of the

solution. (2) Amperometry: monitoring the current change inside the solution during the reaction process. (3) Potentiometry: measuring oxidation/reduction potential of an electrochemical reaction. (4) Impedance: characterizing of the electrochemical impedance spectroscopy of an electrochemical interface [2]. Although this is widely used biosensors to date, its reliability and accuracy can be easily affected by the liquid properties, such as pH values, flow rates and concentrations.

(ii) Optical biosensors

Optical biosensor is another important device, which allows the detection of analyte on the basis of absorption, fluorescence or light scattering. The biosensors can be made based on optical diffraction or electrochemical illumination [3,4]. The main drawbacks of this technique lie in its complexity (e.g. specialized staff is required for the operation), high cost of equipment and large size of most currently available instruments.

(iii) Thermal biosensors

Thermometric biosensors exploit the fundamental property of biological reactions like absorption or evolution of heat. This is reflected as a change in the temperature within the reaction medium. The change in heat is directly monitored to calculate the extent of reaction or structural dynamics of biomolecules in the

dissolved state. Their extensively applications are limited by the long measurement process [5].

(iv) Piezoelectric biosensors

The piezoelectric biosensors are usually mass sensitive and piezoelectric transducers are excited mechanically or electrically so that they can vibrate at their resonant frequency. The transducer surfaces are immobilized with probe molecules to capture the target analytes, which cause a mass change, thus resulting in a resonant frequency shift of the biosensor [34]. Comparing with other type of biosensors, only piezoelectric biosensors are suitable for miniaturization and the fabrication processes are completely compatible with MEMS process, hence they will be discussed in details in the next few sections since they are the research focus in this project.

Micro-machined piezoelectric biosensors are being widely investigated due to their many advantages over other sensors such as compact size, high sensitivity, easy integration with an analysis circuit, and rapid response [35]. Depending on the sensing platform of the sensor, micro-machined piezoelectric biosensors can be classified into cantilever type, quartz-crystal microbalance (QCM) type and diaphragm type.

● Piezoelectric microcantilever biosensor

As shown in Figure 2. 4, upon binding of the target molecules to the receptors, the cantilever will bend and change the stiffness of the device [6]. The relationship of the frequency shift and the mass change is shown as below [34]:

$$\Delta m = \frac{K}{4\pi^2} \left(\frac{1}{f_1^2} - \frac{1}{f_o^2} \right) \quad (2.1)$$

where K is the cantilever spring constant, Δm is the loaded mass, f_1 and f_0 are the resonance frequency before and after bio recognition, respectively.

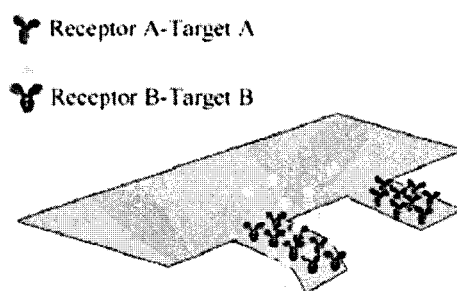


Figure 2. 4. Scheme of cantilever biosensors. The left one was bent due to the mass of the targeted biomolecules captured by the immobilized receptors [35].

Up to date, micro-machined piezoelectric cantilever-based sensors are still the major player in the field of biosensing because of their high sensitivity and label free detection [36-40]. The micro biosensor is self-oscillated at its fundamental vibrant frequency by an oscillating circuit and the vibration frequency is measured by a frequency counter. Most of these sensors use the mass micro-balancing technique to measure the change in resonant frequency after the capture of target molecules on a functionalized micro-cantilever surface [43-45]. Lee et al reported a biosensor, which composed of a micro cantilever and a PZT film (Figure 2. 5). The

length, the width and the thickness of the micro cantilever are 100, 30 and 5 μm , respectively, and the PZT film is 50 μm in length and 2.5 μm in thickness. The micro biosensor is tested by detecting the mussel gluing protein, the insulin-anti insulin binding protein and the poly T-sequence DNA. The estimated sensitivity can be as high as 480 Hz/fg.

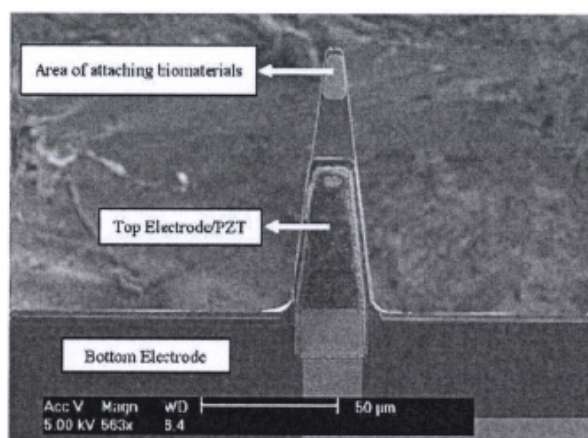


Figure 2. 5. SEM image of a classic piezoelectric cantilever [16].

However, piezoelectric microcantilever biosensor suffers from the low yield after fabrication due to its high fragility. It also suffers from a low Q value in a liquid media. Therefore, extensive applications of this kind of device could be limited by its brittleness under real operating conditions. In addition, it is very challenging to fabricate functional strain multilayered piezoelectric microcantilever biosensor because they always bend up or down due to high residual stress generated in the fabrication process. This could make the characterization/immobilization more difficult.

● Quartz crystal microbalance biosensors

To overcome this issue, the quartz crystal microbalance (QCM) was developed as an alternative. QCM is the best-known, oldest, acoustic wave device due to its simplicity in theory and vast applicability [44-46]. Figure 2.6 shows the sketched structure of a typical QCM sensor. This sensor has a thin plate of AT cut quartz, which is placed at an angle to support a shear deformation and has a zero first order temperature coefficient [47,48]. It has thin metal electrodes deposited on each side of the plate (Figure 2.4 a).

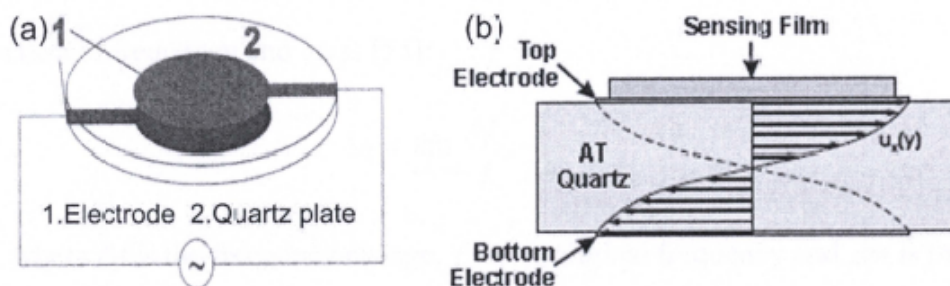


Figure 2.6. Sketches of a typical QCM sensor, a) overall view, b) cross sectional view[6].

An applied voltage across the electrodes creates a large electric field through the bulk of the quartz plate, and a shear mechanical displacement is experienced due to the piezoelectric effect in quartz (Figure 2.4 b). If the applied voltage across the electrodes is of oscillating frequency, a mechanical resonance is created where the bulk acoustic wave is propagated in a direction perpendicular to the surface, resulting in a shear mechanical strain of the material [49]. At peak amplitude, the maximum displacement is noticed to be at the surfaces. Thus, this resonator works

well as a surface sensor whereby any slight perturbation will be reflected in the frequency shift, which makes it more sensitive to mass accumulation [50]. So, it is able to effectively detect any particles that are coupled to its surface.

Recently, the QCM biosensor was reported to be used in many fields of human interest such as detection of genetically modified organism and genetic diagnostics [51,52]. The surface of the QCM sensor is immobilized with bio-receptors. Based on thickness shear mode, analytes bind with the receptors fixed on the sensing surface causing a mass change on the surface of the sensor, thus resulting in a shift in the resonant frequency of the acoustic wave [53,54]. The working principle of a QCM sensor is governed by Equation (2), in which mass sensitivity (S_m) is a function of frequency and mass [55]:

$$S_m = \lim_{\Delta m \rightarrow 0} \frac{\Delta f}{f} \cdot \frac{1}{\Delta m} \quad (2.2)$$

where Δf is the frequency change, f is the original frequency and Δm is the mass change causes by the captured bio-entities. QCM biosensors have many merits, such as high Q factor, feasibility to be used in vivo system and easy measurement through several simple electronics circuits. Moreover, due to the shear mode vibration, the viscosity damping has less impact on the mass sensing in liquid medium. This is a clear advantage for QCM biosensors when used in biological applications where a liquid environment is required during the operation. However, the extensive usability of QCM sensor is hindered by a low operating frequency limited by the thickness of the crystal as well as the lack of integration for use in a biosensor array.

● Piezoelectric diaphragm based biosensors

Piezoelectric diaphragm biosensors have been shown to be a trade-off between all those considerations in piezoelectric cantilever and QCM biosensors [56]. This device simultaneously addresses problems such as the fragility of the silicon-based cantilever in the piezoelectric cantilever biosensor, and the lack of integration potential in the QCM biosensors. The physical structure consists of a multilayered substrate where the diaphragm is subsequently released by microfabrication techniques. The diaphragm usually has a sandwich structure, which consists of a piezoelectric thin film with electrodes on both sides as seen in Figure 2. 7 (a). The bulk vibration behavior of the diaphragm is presented in Figure 2. 7 (b). The biological materials can be immobilized either on the surfaces of top or bottom electrodes.

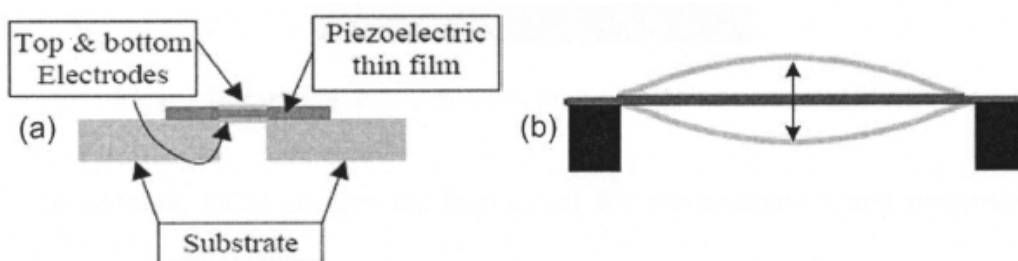


Figure 2. 7. (a) Schematic side-view of a thin film diaphragm (b) and its vibration behavior [1].

The resonance frequency, f_n of a piezoelectric diaphragm can be determined by [1]:

$$f_n = \frac{1}{2\pi} \sqrt{\frac{K_{eff,n}}{M_{eff,n}}} \quad (2.3)$$

where $K_{eff,n}$ and $M_{eff,n}$ respectively stand for effective spring constant and mass of the diaphragm with the subscript n denotes the n^{th} eigenmode. During the operation of both devices in air and liquid environment, a thin diaphragm is shown to exhibit a mass sensitivity of two orders higher than micro cantilever with a significantly higher Q value [56]. Compared to QCM sensors, the advantage of using a multilayered substrate allows the flexibility of deposition of different materials to suit specific requirements with the ease of integration.

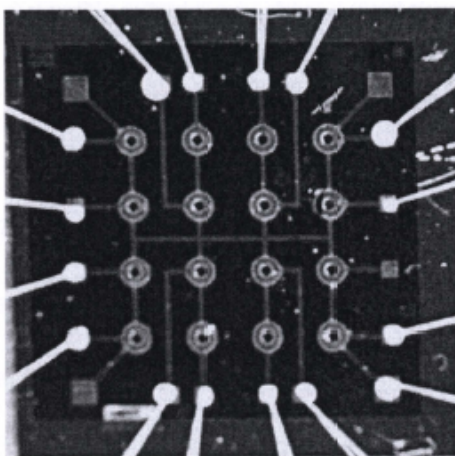


Figure 2. 8. Piezoelectric diaphragm type biosensor array [56].

In addition, QCM sensors are impractical for miniaturization and biosensor array application. Therefore, with all the advantages over the other two types of mass sensitive biosensor, piezoelectric diaphragm type biosensors will be developed in this project. Recently, Niciu et al reported an interesting device based on micro-machined piezoelectric diaphragm arrays [56]. As shown in Figure 2. 8, these 4×4 matrices of piezoelectric diaphragms were fabricated by standard micromachining techniques starting with a silicon-on-insulator (SOI) wafer. Each diaphragm was individually actuated through a PZT thin film. It has been demonstrated as a DNA-

DNA hybridization biosensor with an estimated mass sensitivity of 3.6 Hz/pg which is several hundreds times better than that of the state-of-art values for piezoelectric mass-sensing devices.

However, this device also has some limitations. Firstly, the PZT film was deposited by RF magnetron sputtering, which could lead to difficulties in controlling the stoichiometry of multi-component oxide films. Problems arising from the differences in the sputtering rates of the constituents have a significant effect on the properties of the film. This may be one of the reasons that cause the resonant frequency spectrum as shown in the paper [56]. Moreover, the affinity-based interface of this device is the open top surface of the diaphragm; hence, the reactive liquid that contains biomaterial can flow freely from one sensor to another sensor, resulting in undesired interaction between different biomaterials. Thus, this sensor array is not suitable for multi-biomaterial detection. Therefore, a newly designed piezoelectric biosensor array for multiple biomaterials detection is required in this research. Since CNTs will be used to further increase the sensitivity of the diaphragm based biosensor, the properties and synthesis methods will be reviewed in the next section.

2.2 Carbon nanotubes

CNTs are interesting nanostructures, which are known to possess excellent electrical, mechanical, thermal, optical, and chemical properties. These characteristics have generated great interest in research on CNTs due to their numerous potential applications.

2.2.1 Physical structure of CNTs

The structure of CNT is made up of a stable form of crystalline carbon called graphite. Graphite consists of layers of carbon atoms. Each carbon atom has six electrons, which occupy $1s^2$, $2s^2$, and $2p^2$ atomic orbitals. The $1s^2$ orbital contains two strongly bound core electrons while four more weakly bound electrons occupy the $2s^2 2p^2$ valence orbital for the free carbon atom. In other carbon forms like graphite and diamond, the outer four electrons ($2s^2$ and $2p^2$) forms different hybrid orbitals such as sp , sp^2 and sp^3 . The sigma (σ) bonds formed have maximum electronic overlap with each other. Hence, they form a 3-D interlocking structure, making it rigid. Within the layers of graphite, the atoms are arranged at the corners of hexagons, filling the whole plane. The carbon atoms are strongly bonded by covalent bonds to each other (carbon-carbon distance $\sim 0.14\text{nm}$). Van der Waal's forces of attraction weakly bond the layers to each other (interlayer distance $\sim 0.34\text{nm}$). This weak interlayer coupling gives graphite the property of a seemingly soft material [60-63]. According its physical structure, CNT can be classified into single-walled CNT (SWCNT) and multi-walled CNT (MWCNT).

A SWCNT can be pictured as a seamless hollow cylinder formed by graphene sheet rolled up into a tube (Figure 2. 9 a). The bonding in CNT is essentially composed of sp^2 bonds, similar to those of graphite. However, the circular curvature will cause quantum confinement and σ - π rehybridization, in which three σ bonds are slightly out of plane; for compensation, the π orbital is more delocalized outside the tube. This is the reason why CNT has better mechanical, electrical, thermal properties and are chemically and biologically more active than graphite. A

MWCNT consists of layers of graphite sheets rolled into a group co-axial SWCNT and the sketch of MWCNT is shown in Figure 2. 9 (b).

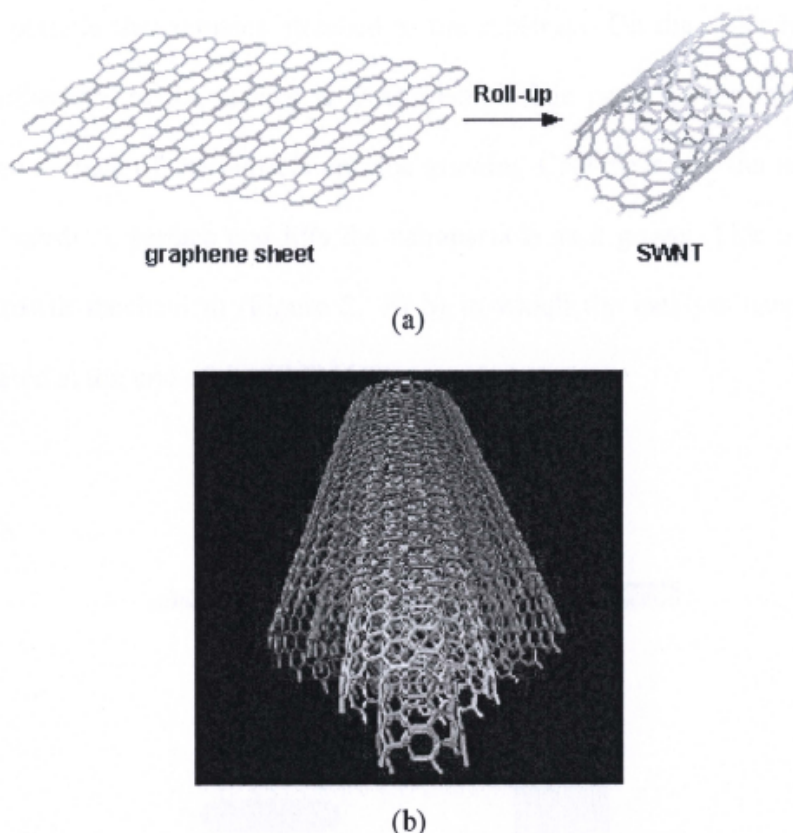


Figure 2. 9. Structure of SWCNT and MWCNT. (a) Model of SWCNT formed from a rolled up sheet of grapheme, (b) Schematic diagram of a MWCNT obtained by rolling sheets of graphene and nested concentrically [64].

2.2.2 Synthesis of CNTs by chemical vapor deposition

The structures and properties of synthesized CNT are closely related to the growth mechanism which ultimately determines the usefulness of the CNTs. So, it is better to understand the CNT growth mechanism before conducting the synthesis processes. Among the numerous literatures, root and tip growth are the two mostly reported mechanism. Root growth mechanism (Figure 2. 10 a) occurs when there is

a strong nanoparticle adherence to the substrate surface. Carbon precipitates from the top surface of the catalytic nanoparticle and the CNT continues to grow upwards from the particle that remains attached to the substrate. On the other hand, if the particle adherence to the surface is weak, then carbon precipitation takes place at the bottom surface of the particle and the growing CNT detaches the nanoparticle from the substrate surface and lifts the nanoparticle as it grows. This is known as the tip growth mechanism (Figure 2. 10 b) in which the catalyst nanoparticle is encapsulated at top end of the CNT [65].

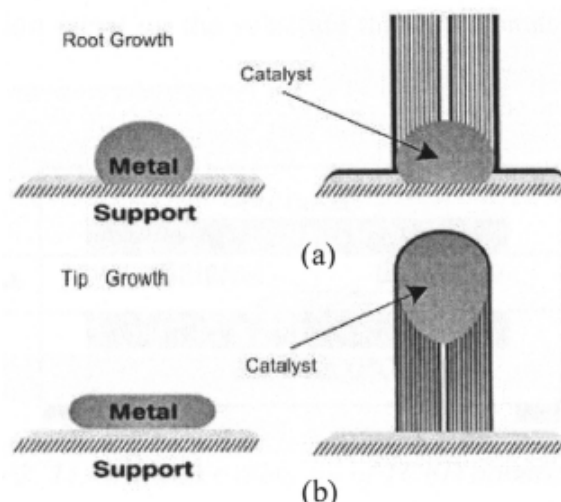


Figure 2. 10. Schematic of (a) root and (b) tip growth mechanism [65].

There are tremendous advances in CNT synthesis since its discovery and many techniques have been developed to date. The earlier successful techniques were arc synthesis and laser ablation while recently chemical vapor deposition (CVD) has gained popularity for its capability in scaled up production and controllability for many commercial applications. Hence, the CVD method is the focus in this research. The CVD technique can be broadly categorized into the thermal CVD (TCVD) and

plasma-enhanced CVD (PECVD). Both methods will be discussed in the following sections.

(i) Thermal chemical vapour deposition

TCVD involves heating a catalyst material to a high temperature in a tube furnace and allowing the flow of hydrocarbon gas (e.g. C_2H_2 or CH_4) through the tube reactor for a specified period. The catalyst layer is prepared by depositing a thin layer of transition metal on the substrate through a sputtering or evaporation process.

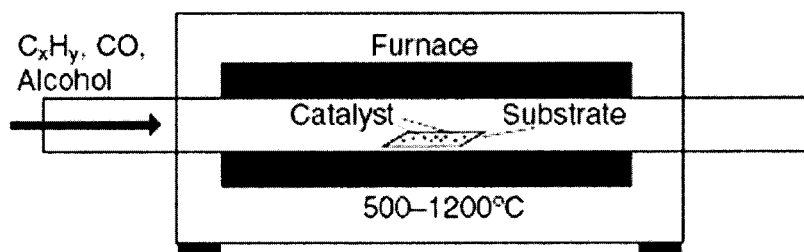


Figure 2. 11. Schematic diagram of TCVD apparatus [9].

Special surface treatment methods, such as chemical etching or thermal annealing, are applied to induce catalyst nucleation. Thermal annealing results in cluster formation on the substrate, which aids in CNT growth. Figure 2. 11 shows the typical schematic of TCVD apparatus. Catalyst layers, normally iron (Fe), nickel (Ni), cobalt (Co), or alloy of the three catalytic metals, are deposited on a substrate (e.g. silicon wafer with SiO_2 film). The specimen is then placed in a CVD reaction furnace and processing gases (e.g. Ar and H_2) are released into the apparatus. When the furnace is heated up to high temperature (500 to 1000 °C) in

vacuum, nano-sized fine catalytic metal particles are formed [9]. Afterwards, reaction gases (e.g. C_2H_2 , CH_4) are added in and react with the catalyst particles to grow CNTs. Gases pass through one end of the apparatus and exit through the other end. CNTs are grown on these fine catalytic metal particles during CVD synthesis. The advantage of this method lies in the simplicity of the apparatus and feasibility of mass production.

(ii) Plasma-enhanced thermal chemical vapor deposition

PECVD has the advantages of low temperature synthesis and its plasma-grown nanotubes are more vertically aligned than TCVD. The schematic diagram of PECVD apparatus is shown in Figure 2. 12. A high frequency current is applied to both electrodes, thus generating a glow discharge in the chamber. Catalytic metals, such as Fe, Ni and Co, on a substrate are firstly etched using H_2 gas. Afterwards, reaction gases, such as C_2H_2 , CH_4 , C_2H_4 , C_2H_6 and CO pass through the top plate to supply the carbon sources. CNTs are grown on the nano-size catalytic particles by glow discharge generated from high frequency power [8]. The strong electrical field induced by the plasma results in cone shaped CNTs with a varying diameter along their length, which makes them less suitable for practical applications [66]. Moreover, the apparatus used in PECVD are much more complex than that of those TCVD. As such, TCVD will be employed as the CNT synthesis method in this project.

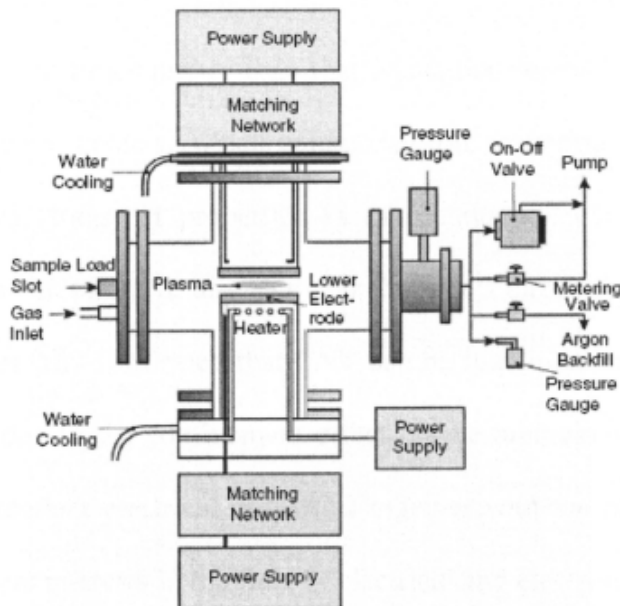


Figure 2. 12. Schematic diagram of PECVD apparatus [8].

2.2.3 CNT properties

The electrical, mechanical and chemical properties will be discussed in the following sections.

(i) Electrical properties

Electrical properties of the CNTs can be metallic, semiconducting or insulating depending on the structure, diameter and chiral angle of the nanotube. Synthesized CNT are usually one third metallic, which have the armchair structure, while the rest are semiconducting. Individual MWCNT has been observed to possess a variety of novel electrical properties, including two-dimensional quantum-interference effects due to weak localization and universal-conductance fluctuations. Theoretical

and experimental results show that CNTs can carry current density of up to 10^9 A/cm², which is 1000 times higher than that of copper wires [67]. Unfortunately, MWCNTs often have defects, which cause electron scattering. CNTs also have exceptional ballistic transport properties as the conduction electrons in metallic SWNTs experience an effective disorder over the tube's circumference [10]. It also has been experimentally confirmed that CNT can be functionalized like a quantum wire intrinsically due to the confinement effect on the tube circumference [8]. All the unique and excellent electrical properties together with the nano size of CNTs have generated great interests in the field of electrical and electronic applications.

(ii) Mechanical properties

Both experimental and theoretical calculations have shown that a carbon nanotube is as stiff as a diamond with very high Young's modulus and tensile strength [8]. These excellent mechanical properties are due to the C-C covalent bonding and the seamless hexagonal network [67]. CNTs have Young's modulus of up to 1800 GPa, which is almost twenty times higher than that of steel. CNTs are very resilient to bending because they contain few defects and the carbon-carbon bonds in CNTs are sp² hybrids, which can rehybridize after bending [60]. For an individual CNT with a Young's modulus of 1000 GPa, the tensile strength can be as high as 150 GPa and the high elastic strain (~15%) of CNT is also a result of sp² rehybridization, in which the high strain is released through the elastic buckling [8].

(iii) Chemical properties

Small radius, large specific surfaces and σ - π rehybridization make CNT very attractive in chemical and biological applications because of their strong sensitivity to chemical or environmental interactions. The tips of the CNT are more reactive than its cylindrical sidewall because of the presence of metallic catalysts sitting on the opened ends and they have greater curvature. Many approaches have been used to open the nanotube tips. These methods include oxidation, plasma etching, and chemical reaction using acids such as HNO_3 [8]. At the same time, these processes also help to convert CNT from hydrophilic to hydrophobic. Other than the tips of the CNT, the side walls and inner walls can also be chemically functionalized with different functional groups such as carboxyl. Functionalization of CNT is necessary for many applications such as chemical and biological separation, purification, sensing/detection, energy storage, and electronics.

Applications of CNTs range in various fields, such as semiconductors, field emission, energy storage, conductive connectors, molecular electronics, thermal materials, and biomedical applications [8]. This report will focus on discussing the application of CNTs in biochemical sensing.

2.2.4 Biological applications of CNTs

CNTs have been widely used as sensing platforms in biological or chemical sensors due to their unique properties. Some typical applications in biosensing are briefly discussed in the following sections:

(i) CNT-based amperometric enzyme electrodes

An attractive avenue for preparing CNT-based amperometric enzyme electrodes involves CNT/insulator/enzyme biocomposites [68-70]. Conventional carbon-paste composites have been widely used for the design of amperometric enzyme electrodes [71]. Britto et al. prepared a composite electrode based on mixing MWCNT and bromoform as a binder [72]. As shown in Figure 2. 13, CNT paste enzyme electrodes were prepared by mixing CNTs with mineral oil. Such composite electrodes combine the ability of carbon nanotubes to promote electron-transfer reactions with the attractive advantages of paste electrode materials. The resulting biocomposite was packed within a needle and used as a microsensor [73].

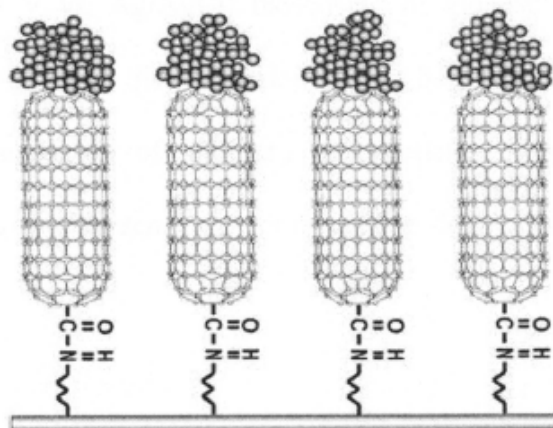


Figure 2. 13. Nanoforest of vertically aligned CNT trees acting as molecular wires [73].

(ii) CNT based glucose biosensor

The diagnosis and management of diabetes mellitus require tight monitoring of blood glucose levels. Glucose electrochemical biosensors play a leading role in this

direction. Lin *et al.* [74] reported glucose biosensors based on CNT nanoelectrode ensembles (Figure 2. 14).

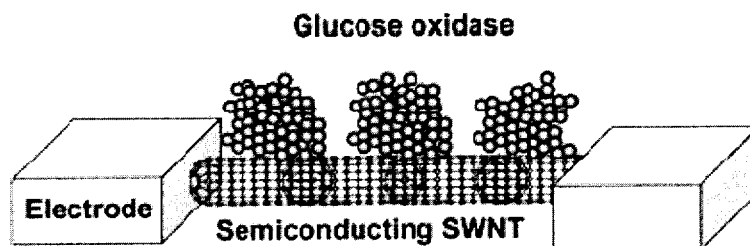


Figure 2. 14. Schematic picture of two electrodes connecting a semiconducting SWCNT with GOx enzymes immobilized on its surface [75].

CNT/Nafion/GOx-coated electrodes, coupling the electrocatalytic detection of hydrogen peroxide with the permselectivity of Nafion, offered highly selective, low-potential (~ 0.05 V vs. Ag/AgCl) biosensing of glucose [76]. The resulting biosensor offered an effective discrimination against both neutral and anionic redox constituents. The deposition of platinum nanoparticles onto Nafion-containing CNT/GOx film led to higher sensitivity compared to devices based on CNT or Pt-particles alone.

(iii) CNT-based electrochemical DNA biosensors

DNA biosensors, based on nucleic acid recognition processes, are rapidly developed towards the goal of rapid, simple and inexpensive testing of genetic and infectious diseases. Electrochemical hybridization biosensors rely on the immobilization of a single-stranded (ss) DNA probe onto the transducer surface that converts the duplex formation into a useful electrical signal [77]. The performance

of such devices can be improved further with the use of CNT. Such improvements are attributed to enhanced detection of the target guanine or the product of an enzyme label, as well as to the use of CNT carrier platforms. Surface-confined MWCNT have been shown in Figure 2. 15.

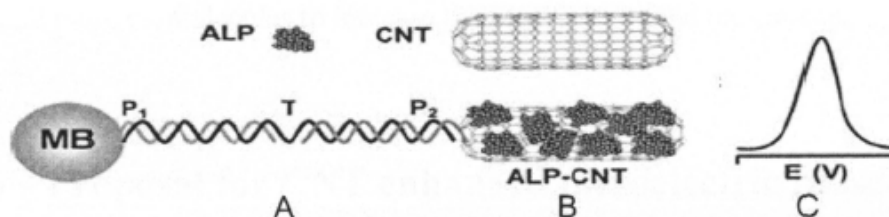


Figure 2. 15. CNT-derived amplification of the recognition and transduction events [78].

In the stage of A, the alkaline phosphatase (ALP) loaded CNT tags are captured to the streptavidin modified magnetic beads by the DNA recognition events; Addition of the substrate and enzymatic reaction occurs in process B; Lastly, electrochemical detection of the product of the enzymatic reaction at CNT-modified glassy carbon electrode (stage C).

The interesting works discussed above demonstrate a bright future for the CNT in biosensing applications. However, there are still some challenges faced by us in order to develop viable and durable CNT based biosensors. Firstly, it is very difficult to align CNTs onto the sensing surface or electrodes due to the nano scale size and strong static forces between the CNTs. The quality and quantity of the misaligned CNTs can't be controlled; hence, the accuracy and repeatability of the CNT based biosensors will be seriously affected. Secondly, signals from the CNT-based biosensors are mainly generated from the CNT property changes (e.g. electrical resistance, optical image change), however, CNT properties are determined by

many parameters including purity, conductivity, single or multi-wall nature. These parameters are again strongly dependent on the synthesis processes, which are difficult to be controlled precisely. To avoid these problems, in this project, CNTs will be integrated with piezoelectric sensors and used just as the sensing platform to capture more biomolecules to increase the sensitivity of the biosensors.

2.3 Proposal for CNT enhanced piezoelectric biosensors

In the first stage of this project, a square piezoelectric diaphragm based sensor array will be developed to verify the possibility of using this diaphragm as a biosensor. Optimization of the fabrication process will also be implemented. The schematic of a single sensor is shown in Figure 2. 16 (a). The piezoelectric diaphragm has a multilayer structure. The thin SiO₂ film at the lowest level acts as the passive layer and together with the bottom electrode and PZT film to form a bimorph structure to excite the vibration. Top and bottom electrodes (Pt/Ti thin films) are deposited on both sides of the PZT films. The deep hole in the opposite side can be created by wet etching processes and will be used as reaction chambers for the bio-immobilization. The PZT film will be deposited by the sol-gel deposition method and the polyimide film surrounding the top electrodes can reduce the parasitic capacitance. To study the effect of different designs on the sensor sensitivity, another circular sensor array with similar structure is also proposed, in which the individual sensors share the common bottom electrode and separated top electrodes (as shown in Figure 2. 16 b) and the bottom reaction chambers are etched

by deep reactive ion etching. The merit of a sensor array is the multiple biomaterials detection, which can significantly save the testing time and cost.

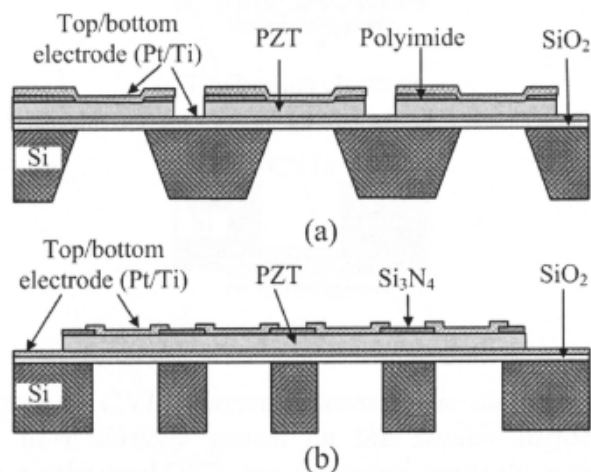


Figure 2. 16. Proposed design of piezoelectric diaphragm based (a) square shape biosensor, (b) circular biosensor.

In order to increase the sensitivity of the diaphragm based biosensor, a CNT enhanced biosensor is also proposed. The key idea of incorporating CNTs is to use the high specific surface area of the CNTs to absorb more bio-molecules to amplify the output signals, which lead to a higher sensitivity. The sensors for CNT integration are those shown in Figure 2.16. Two methods of employing CNTs onto the sensing platform are proposed. In the first method, CNTs will directly grow from the reaction chambers. A catalyst (Fe) film will be deposited onto the bottom surface of the chamber and CNTs will be grown by TCVD. The sketch is shown in Figure 2. 17 (a). By using this method, CNTs may have good uniformity and well controlled density.

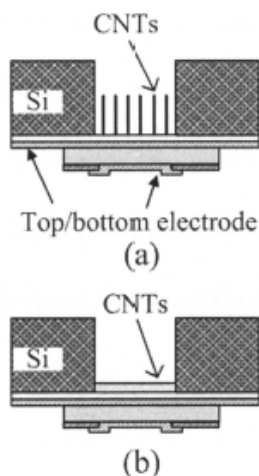


Figure 2. 17. Sketch of CNT enhanced piezoelectric diaphragm based biosensor array. (a) CNTs were directly grown on the bottom surface of the reaction chambers; (b) pre-synthesized CNTs are deposited inside the reaction chamber.

As an alternative, CNTs will be synthesized in a separated substrate and transferred to a solution. After several chemical and physical treatments and ultrasonic vibration, CNTs will be dissolved into the solution uniformly. Afterwards, the CNT mixed solution will be dropped into the reaction chambers in the sensors (Figure 2. 17 b). CNTs will be attached onto the bottom surface of the reaction chamber after the solvent is evaporated. Afterwards, CNTs will be functionalized for the bio-immobilization.

2.4 Summary of this chapter

In this chapter, a systematic review of biosensors and CNTs is presented. The biosensor introduction, bio-recognition element and immobilization techniques are reviewed. The advantages and disadvantages of three main types of piezoelectric

biosensors, such as QCM biosensor, piezoelectric cantilever and diaphragm biosensor, are compared and discussed. Because CNTs will be integrated with the diaphragm based piezoelectric biosensor to enhance the sensitivity, the structures, deposition method and bio-applications of CNTs are summarized. A CNT enhanced piezoelectric biosensor is also proposed at the end of this chapter.

Chapter 3

Biosensor Design and Simulation

In this chapter, a novel analytical model for the resonant frequency of a micro-machined piezoelectric diaphragm working in a mixed mode of tension and flexural rigidity is established based on the classic plate theory. The gravimetric sensitivity is derived and the results show that it is independent of the tension and flexural rigidity. Based on the gravimetric sensitivity, mass sensitivity is also defined and confirmed by the finite element analysis. The study shows that the diaphragm in the sensor should be designed to be thin and small with low density to achieve a high mass sensitivity. By considering the sensitivity and difficulty of biomaterial immobilization, the designed diaphragm diameter varied from 600 μm to 1000 μm with a thickness of about 1 μm .

3.1 Sensor design and working principle

The piezoelectric diaphragm based biosensor will be micro-fabricated on a silicon wafer. As the sketched simplified structure shown in Figure 3.1, it consists of silicon substrate, reaction chamber and a composited diaphragm which will be etched from the backside of the substrate. The composited diaphragm consists of

one thin SiO₂ film, two metal electrodes and one PZT layer. The SiO₂ and the PZT layer form a bimorph structure to excite the vibration as well as a stop layer during the reaction chamber etching process. The thin PZT layer will be deposited by sol-gel deposition method and used as the active layer during the vibration. The top and bottom electrodes of the sensor will be deposited on both sides of the PZT layer by sputtering. The detailed diaphragm thickness and the reaction diameter will be optimized and discussed in the following sections.

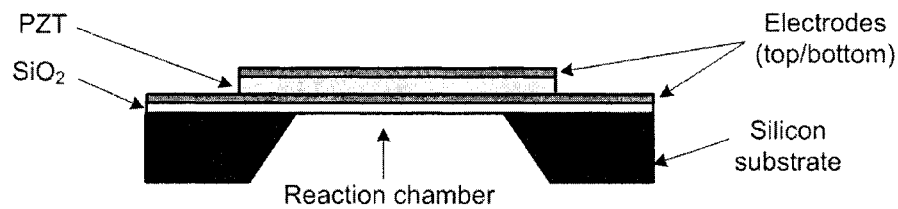


Figure 3. 1. A sketch of the designed biosensor.

The piezoelectric diaphragm based biosensor, which will be studied in this project, actually works as a mass sensor. The working principle of this sensor is that the resonant frequency of the diaphragm decreases in response to an external mass loading onto the sensing surface. For an amount of mass added onto the micro-machined diaphragm surface, the resonant frequency change of the sensor is inversely proportional to the added mass. The relationship is shown in Eq.3.1:

$$\Delta f \propto \frac{1}{\Delta m} \quad (3.1)$$

where Δf and Δm denote the frequency change and the amount of mass added onto the sensor, respectively. If bio-receptors are immobilized onto the sensor surface and significant frequency shift is observed after capturing the target analyte, the developed piezoelectric mass sensor can be potentially used as a biosensor.

3.2 Sensor vibration analysis

The vibration characteristics of a diaphragm structure depend on whether the structure behaves as a tension dominated diaphragm/membrane or a flexural rigidity dominated plate. In case of an edge-clamped circular diaphragm with radius R , the resonant frequency (f_0) can be expressed as [79,80] either:

$$f_0 = \frac{\lambda^2}{2\pi R^2} \sqrt{\frac{D}{\rho d}} = \frac{\lambda^2}{2\pi R^2} \sqrt{\frac{D}{M}} \quad (3.2)$$

or

$$f_0 = \frac{\alpha^2}{2\pi R} \sqrt{\frac{T}{\rho d}} = \frac{\alpha^2}{2\pi R} \sqrt{\frac{T}{M}} \quad (3.3)$$

where λ and α are the frequency parameters, which depend on the vibration modes, $D=Ed^3/12(1-\nu^2)$ is the flexural rigidity, T is the initial tension of the diaphragm, ρ and d are the density and thickness of the diaphragm, respectively; E is the Young's modulus and ν is the Poisson's ratio. $M=\rho d$ is the mass per unit area of the diaphragm (unit: kg/m²). Eq. (3.2) and (3.3) are also applicable to a square shaped diaphragm, but the radius (R) in the equations needs to be replaced by the length of the square (L). In the circular membrane, the values of λ and α can be founded in Table 3.1-3.2, where n and s refer to the number of nodal diameters and the number of nodal circles, respectively.

Table 3. 1. Values of λ^2 for an edge-clamped circular diaphragm [79].

Nodal Circle (s)	Nodal Diameter (n)		
	0	1	2
0	2.404	3.832	5.135
1	5.520	7.016	8.417
2	8.654	10.173	11.62

Table 3. 2. Values of α^2 for an edge-clamped circular diaphragm [81].

Nodal Circle (s)	Nodal Diameter (n)		
	0	1	2
0	10.2158	21.26	34.88
1	39.771	60.82	84.58
2	89.104	120.08	153.81

However, due to the complexity of the micro-fabrication process, the residual stress in the diaphragm is not avoidable after the fabrication. Both tension and stiffness are interacting simultaneously in the micro-sensors and no mixed mode model is available till today. Hence, an alternative equation is needed to govern these mixed mode vibration. Since square and circular diaphragms based sensors will be fabricated in this project, the equations will be established for both circular and square diaphragms by means of the classical theory of plate vibrations. In this study, it should be noted that the classic theory of membrane vibrations is not suitable as the rigidity is not considered inside.

3.2.1 Resonant frequency of a square diaphragm based sensor

By considering a clamped square plate [82] the nonlinear partial differential equation governing a plate with initial tension can be obtained as Eq. 3.4, where $w(x,y,t)$ is the transverse displacement.

$$\rho h \frac{\partial^2 w}{\partial t^2} + D \nabla^4 w - T \nabla^2 w = -\eta \frac{\partial w}{\partial t} + f(x, y, t) \quad (3.4)$$

where ρ : the density of the diaphragm material; h : the diaphragm thickness; $w(x,y,t)$: the transverse displacement, x : length of the diaphragm; y : width of the diaphragm; t :

time; D : the flexural rigidity of the diaphragm; T : the initial tension per unit length; η : the damping coefficient; $f(r, \theta, t)$: the transverse loading per unit area. The Laplace operator (∇^2) and biharmonic operator ($\nabla^4 = \nabla^2 \cdot \nabla^2$) in Cartesian coordinate are

$$\nabla^2 = \frac{\partial^2}{\partial x^2} + \frac{\partial^2}{\partial y^2} \Rightarrow \nabla^4 = \frac{\partial^4}{\partial x^4} + 2 \frac{\partial^4}{\partial x^2 \partial y^2} + \frac{\partial^4}{\partial y^4} \quad (3.5)$$

The flexural rigidity (D) for a diaphragm composed of one layer is defined as follows:

$$D = Eh^3 / (12(1-\nu^2)) \quad (3.6)$$

where E is the Young's modulus, h is the thickness and ν is the Poisson's ratio.

In a typical piezoelectric mass sensor, as it is mentioned earlier, the diaphragm is composed of different layers like SiO₂, Pt/Ti, and PZT layers. A sketched simplified diaphragm structure is shown in Figure 3.2. For these multilayered diaphragms, the flexural rigidity can be calculated by Eq. 3.7.

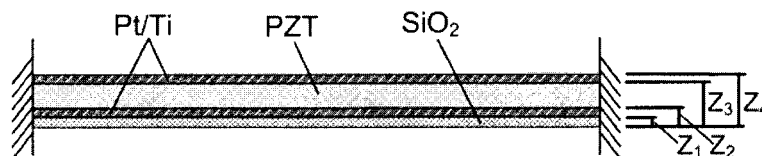


Figure 3. 2. A sketch of the diaphragm structure.

$$\begin{aligned} A &= \sum_i \frac{E_i}{1-\nu_i^2} (z_i - z_{i-1}); & B &= \sum_i \frac{E_i}{1-\nu_i^2} \left(\frac{z_i^2 - z_{i-1}^2}{2} \right) \\ C &= \sum_i \frac{E_i}{1-\nu_i^2} \left(\frac{z_i^3 - z_{i-1}^3}{3} \right); & D &= \frac{AC - B^2}{A} \end{aligned} \quad (3.7)$$

where $i = 1, 2, 3$ and 4 represents the layer number and z illustrates the total height from the bottom surface (as shown in Fig.3.2). A, B, C are the coefficients

and D is the effective flexural rigidity. In the absence of damping and forcing, we will search for a modal solution of the form

$$w(x, y, t) = W(x, y)e^{i\omega t} \quad (3.8)$$

where $W(x, y)$ is an unknown function and ω is the natural frequency.

Substituting Eq.3.9 into Eq. 3.4, we obtain

$$-\rho h\omega^2 W + D\nabla^4 W - T\nabla^2 W = 0 \quad (3.9)$$

The Eq. 3.9 can also be expressed as

$$\left(\nabla^2 + \gamma_1^2\right)\left(\nabla^2 - \gamma_2^2\right)W = 0 \quad (3.10)$$

Where

$$\gamma_1^2 = \frac{-T + \sqrt{T^2 + 4\rho h\omega^2 D}}{2D}; \gamma_2^2 = \frac{+T + \sqrt{T^2 + 4\rho h\omega^2 D}}{2D} \quad (3.11)$$

There are two boundary conditions to be satisfied at any point on the boundary of square diaphragm, which are shown in Eq. 3.6.

$$\begin{aligned} \text{at } x = 0, a \quad w(x, y, t) = 0; \quad \frac{\partial w(x, y, t)}{\partial x} = 0 \\ \text{at } y = 0, a \quad w(x, y, t) = 0; \quad \frac{\partial w(x, y, t)}{\partial y} = 0 \end{aligned} \quad (3.12)$$

where a is the width of the square diaphragm. A possible solution for Eq. 3.12, which satisfied the clamped boundary condition, is proposed by Leissa [81] as Eq.

3.13

$$W_{m,n}(x, y) = A \left(\cos\left(\frac{2m\pi x}{a}\right) - 1 \right) \left(\cos\left(\frac{2n\pi y}{a}\right) - 1 \right) \quad (3.13)$$

where a is the width of the square diaphragm, A is a constant, m and n are the number of nodal points in length and width direction, respectively. By normalizing the natural modes as it is illustrated in Eq. 3.14 the constant A can be obtained as

$$\int_0^a \int_0^a \rho (W_{mn})^2 dx dy = \int_0^a \int_0^a \rho \left(A \left(\cos\left(\frac{2m\pi x}{a}\right) - 1 \right) \left(\cos\left(\frac{2n\pi y}{a}\right) - 1 \right) \right)^2 dx dy = 1 \quad (3.14)$$

$$\text{So } A = \frac{2}{3a\sqrt{\rho}}$$

And the natural frequency can be written as:

$$\omega_{mn} = \sqrt{\frac{1}{\rho h} (\gamma_{1mn}^4 D + \gamma_{1mn}^2 T)} \quad (3.15)$$

Therefore, the resonant frequency of a square diaphragm is obtained in Eq. 3.16

$$f_{mn} = \frac{1}{2\pi} \sqrt{\frac{1}{\rho h} (\gamma_{1mn}^4 D + \gamma_{1mn}^2 T)} \quad (3.16)$$

3.2.2 Resonant frequency for a circular diaphragm based sensor

The natural frequency of a clamped circular diaphragm can be obtained by using a similar approach as discussed for the square diaphragm. The differential equation (Eq. 3.4) needs to be changed into Eq. 3.17,

$$\rho h \frac{\partial^2 w}{\partial t^2} + D \nabla^4 w - T \nabla^2 w = -\eta \frac{\partial w}{\partial t} + f(r, \theta, t) \quad (3.17)$$

where r : radius of the diaphragm; θ : angle. The boundary condition of this diaphragm is shown in Eq. 3.18 and the deflection and slope of the diaphragms are zero at $r=a$.

$$w(r, \theta, t) = 0; \frac{\partial w(r, \theta, t)}{\partial r} = 0 \quad \text{at} \quad r = a \quad (3.18)$$

where a is the radius of the circular diaphragm. Again, in the absence of damping and forcing, we will search for a modal solution of the form

$$w(r, \theta, t) = W(r, \theta) e^{i\omega t} \quad (3.19)$$

where $W(r, \theta)$ is an unknown function and ω is the natural frequency.

Substituting Eq.3.19 into Eq. 3.15, we obtain

$$-\rho h \omega^2 W + D \nabla^4 W - T \nabla^2 W = 0 \quad (3.20)$$

The Laplacian ∇^2 is the divergence of the gradient in polar coordinates, which is given by

$$\nabla^2 = \frac{\partial^2}{\partial r^2} + \frac{1}{r} \frac{\partial}{\partial r} + \frac{1}{r^2} \frac{\partial^2}{\partial \theta^2} \quad (3.21)$$

Eq. 3.21 can be expressed as

$$\left(\nabla^2 + \gamma_1^2 \right) \left(\nabla^2 - \gamma_2^2 \right) W = 0 \quad (3.22)$$

Where

$$\gamma_1^2 = \frac{-T + \sqrt{T^2 + 4\rho h \omega^2 D}}{2D}; \gamma_2^2 = \frac{+T + \sqrt{T^2 + 4\rho h \omega^2 D}}{2D} \quad (3.23)$$

Eq. 3.22 is satisfied by every solution of the form

$$\left. \begin{array}{l} \left(\nabla^2 + \gamma_1^2 \right) W_1 = 0 \\ \left(\nabla^2 - \gamma_2^2 \right) W_2 = 0 \end{array} \right\} \Rightarrow W = W_1 + W_2 \quad (3.24)$$

A possible solution for Eq. 3.24 is the separation variables as the following:

$$W(r, \theta) = R(r) \Theta(\theta) \quad (3.25)$$

Substitution of $W(r, \theta)$ into Eq. 3.24, results into Eq. 3.26.

$$\begin{aligned} r^2 \left(\left(\frac{\partial^2 R}{\partial r^2} + \frac{1}{r} \frac{\partial R}{\partial r} \right) \frac{1}{R} + \gamma_1^2 \right) &= -\frac{1}{\Theta} \frac{\partial^2 \Theta}{\partial \theta^2} \\ r^2 \left(\left(\frac{\partial^2 R}{\partial r^2} + \frac{1}{r} \frac{\partial R}{\partial r} \right) \frac{1}{R} - \gamma_2^2 \right) &= -\frac{1}{\Theta} \frac{\partial^2 \Theta}{\partial \theta^2} \end{aligned} \quad (3.26)$$

Eq. 3.26 can be satisfied if and only if each of the four expressions is equal to the same constant m^2 . Therefore the Eq. 3.26 leads to

$$\begin{aligned} \frac{\partial^2 \Theta}{\partial \theta^2} + m^2 \Theta &= 0 & (a) \\ \left(\frac{\partial^2 R}{\partial r^2} + \frac{1}{r} \frac{\partial R}{\partial r} \right) + \left(\gamma_1^2 - \frac{m^2}{r^2} \right) R &= 0 & (b) \\ \left(\frac{\partial^2 R}{\partial r^2} + \frac{1}{r} \frac{\partial R}{\partial r} \right) - \left(\gamma_2^2 + \frac{m^2}{r^2} \right) R &= 0 & (c) \end{aligned} \quad (3.27)$$

The solution of Eq. 3.27 a is as follow

$$\Theta(\theta) = A_{1m} \sin m\theta + A_{2m} \cos m\theta \quad (m = 0, 1, 2, \dots) \quad (3.28)$$

The solution of Eq.3.28 must be continuous, implying that the solution for $\theta=\theta_0$ should be equal to the solution for $\theta=\theta_0+2\pi$, and therefore m must be an integer. Eq. 3.27 (b) is a Bessel equation, and therefore its solution is composed of $J_m(\gamma_1 r)$ and $Y_m(\gamma_1 r)$ which are the Bessel functions of order m and of the first and second kind, respectively. Eq. 3.27 (c) is a modified or hyperbolic Bessel equation, and therefore its solution is composed of $I_m(\gamma_2 r)$ and $K_m(\gamma_2 r)$ which are the modified Bessel functions of order m and of the first and second kind, respectively. Finally, function $R(r)$ is found as the following:

$$R(r) = B_{1m} J_m(\gamma_{1m} r) + B_{2m} Y_m(\gamma_{1m} r) + B_{3m} I_m(\gamma_{2m} r) + B_{4m} K_m(\gamma_{2m} r) \quad (3.29)$$

where B is the constant coefficient and determined from the boundary condition. Both $Y_m(\gamma_1 r)$ and $K_m(\gamma_2 r)$ are singular at $r=0$. Therefore, for a plate with a displacement at the plate center, the coefficients B_{2m} and B_{4m} are equal to zero. Applying function $R(r)$ into the boundary condition (Eq.3.18), results in the two following equations.

$$\begin{bmatrix} J_m(\gamma_1 a) & I_m(\gamma_2 a) \\ J'_m(\gamma_1 a) & I'_m(\gamma_2 a) \end{bmatrix} \begin{bmatrix} B_{1m} \\ B_{3m} \end{bmatrix} = 0 \quad (3.30)$$

The prime indicates a derivative with respect to r . Two important results are obtained from Eq. 3.30, first a relation between the coefficients which is depicted in Eq. 3.31, and second the fact that for non-trivial solutions of B_{1m} and B_{3m} the characteristic equation should be equal to zero as shown in Eq.3.32.

$$B_{1m} = -\frac{I_m(\gamma_2 a)}{J_m(\gamma_1 a)} B_{3m} \quad (3.31)$$

$$J_m(\gamma_1 a) I'_m(\gamma_2 a) - I_m(\gamma_2 a) J'_m(\gamma_1 a) = 0 \quad (3.32)$$

Determining the roots of Eq. 3.32 and labeling them successively as $n=1,2,\dots$ for each $m=0,1,2,\dots$, gives the eigenvalues of Eq. 3.30. m and n are integers and represents number of diametrical and circular nodes, respectively. Reordering Eq. 3.23 and replacing the obtained eigenvalues into that gives the natural frequencies as shown in Eq. 3.33.

$$\omega_{mn} = \sqrt{\frac{1}{\rho h} (\gamma_{1mn}^4 D + \gamma_{1mn}^2 T)} \quad (3.33)$$

Therefore the resonant frequency is shown in Eq. 3.34

$$f_{mn} = \frac{1}{2\pi} \sqrt{\frac{1}{\rho h} (\gamma_{1mn}^4 D + \gamma_{1mn}^2 T)} \quad (3.34)$$

Finally the mode shape is obtained as the following

$$W_{mn}(r, \theta) = \left[J_m(\gamma_{1mn}r) - \frac{J_m(\gamma_{1mn}a)}{I_m(\gamma_{2mn}a)} I_m(\gamma_{2mn}r) \right] (A_{1m} \sin m\theta + A_{2m} \cos m\theta) \quad (3.35)$$

By solving the characteristic Eq. 3.32 numerically and obtain the eigenvalues of γ_{1mn} and γ_{2mn} , the resonant frequency of a circular plate can be calculated by Eq. 3.34. However, there are two variables in the Eq. 3.32, either D or T must be known in order to find the relationship between γ_{1mn} and γ_{2mn} , so that Eq. 3.32 can only be solved. For the demonstration, in this chapter, we set T=0, then the he values of $(\gamma_{1mn}a)^2$ are easily obtained and shown in Table 3.3.

Table 3. 3: Frequency parameters $(\gamma_{1mn}a)^2$ for a fully clamped circular or square plate.

$n \backslash m$	1	2	3	4	5	6
1	35.99	73.40	131.90	210.526	309.04	428
2	73.40	108.24	165.02	242.66	340.59	458.27
3	131.90	165.02	220.06	296.35	393.36	509.9
4	210.526	242.66	296.35	371.38	467.29	583.83
5	309.04	340.59	393.36	467.29	562.18	676
6	428	458.27	509.9	583.83	676	792.5

It is interesting to find that Eq. 3.16 and 3.34 are identical by considering the joint effect from the rigidity and stress. This result implies that the resonant frequency of the diaphragm possess a shape independent nature. Based on Eq. 3.34, if we set $(\gamma_{1mn}a)^2=k$, where k is a constant, the Eq. 3.34 can be rewritten as

$$f_{mn} = \frac{1}{2\pi a} \sqrt{\frac{1}{\rho h} \left(\frac{k^2 D}{a^2} + kT \right)} \quad (3.36)$$

Based on Eq. 3.36, two extreme conditions can be considered, where one is the flexural rigidity dominated plate ($T=0$, Eq. 3.37) and another one is the tension dominated diaphragm ($D=0$, Eq. 3.38). The following two equations can be derived:

$$f_{mn} = \frac{k}{2\pi a^2} \sqrt{\frac{D}{\rho h}} \quad \text{if } T = 0 \quad (3.37)$$

$$f_{mn} = \frac{\sqrt{k}}{2\pi a} \sqrt{\frac{T}{\rho h}} \quad \text{if } D = 0 \quad (3.38)$$

It is clear that Eq. 3.37 and 3.38 are identical with Eq. 3.2 and 3.3, this consistency proves the validity of the derived resonant frequency equations (Eq. 3.16 and 3.34) for the diaphragm based sensors in this work. Thus, the sensitivity of the sensors will be calculated based on the derived resonant frequency equations in the following sections.

3.3 Sensitivity of the diaphragm based sensors

Sensitivity is one of the most crucial parameters in evaluating the performance of a biosensor. The physical structure of the biosensor has to be carefully designed to achieve the highest sensitivity. Choosing the proper diaphragm thickness and size are the two main challenges in the biosensor design. Hence, it is necessary to define the sensitivity and investigate the relationships between the sensor sensitivity and the diaphragm thickness and size.

3.3.1 Gravimetric sensitivity

The gravimetric sensitivity (S_M) is the rate of resonant frequency change in response to the change of the uniformly distributed loaded mass per unit area on a piezoelectric mass sensor; it can be defined as [83]

$$S_M = \lim_{\Delta M \rightarrow 0} \frac{\Delta f}{f_0} \cdot \frac{1}{\Delta M} \quad (3.39)$$

where ΔM is the mass per unit area loaded onto the sensor surface, and $\Delta f = f - f_0$ is the frequency change in response to the loaded mass. The standard unit of S_M is m^2/kg .

Differentiating Eq. 3.16 or 3.34 with respect to M , we obtain:

$$\frac{df}{dM} = -\frac{1}{2} \cdot \frac{1}{2\pi} \sqrt{\frac{1}{M}(\gamma_1^4 D + \gamma_1^2 T)} \cdot \frac{1}{M} = -\frac{1}{2M} \quad (3.40)$$

where $M = \sum \rho_i d_i$ for the case of multilayer diaphragm, ρ_i and d_i are the density and thickness of the i^{th} layer in the diaphragm, respectively. Regardless of D or T dominates in the diaphragm, using Eq. 3.40 together with the definition in Eq. 3.39, we can obtain one unique expression for gravimetric sensitivity for both cases directly as below.

$$S_M = \frac{1}{f_0} \frac{df}{dM} = -\frac{1}{2f_0} \cdot \frac{1}{2\pi} \sqrt{\frac{1}{M}(\gamma_1^4 D + \gamma_1^2 T)} \cdot \frac{1}{M} = -\frac{1}{2M} = -\frac{1}{2\sum \rho_i d_i} \quad (3.41)$$

It can be seen from Eq.3.41 that the gravimetric sensitivity is independent of the residual stress and flexural rigidity of the diaphragm. In another word, the gravimetric sensitivity is solely determined by the mass per unit area of the diaphragm itself.

Since the gravimetric sensitivity of the diaphragm based sensor defined by Eq. 3.41 has nothing to do with the tension T and the flexural rigidity D , the troublesome issue of checking the specific resonant behavior of the fabricated diaphragm can be avoided. Meanwhile, effects of all the other factors (e.g. T or D) of the sensor are solely exhibited in the resonant frequency f_0 . Once the sensor has been fabricated, the S_M can be easily calculated from Eq. 3.41.

It is clear that the gravimetric sensitivity is inversely proportional to the density and thickness of the multiple layers within the diaphragm. Therefore, in order to develop a piezoelectric biosensor with high sensitivity, the thickness of each layer should be made as thin as possible. Due to this reason, there is a great research attention to use MEMS technology to develop micro-diaphragm based biosensors in this project.

3.3.2 Mass sensitivity

Mass sensitivity is the resonant frequency change corresponding to a unit mass load [84-86]. This is a normalized sensitivity and can be written as:

$$S_m = -\frac{\Delta f}{\Delta m} \quad (3.42)$$

where Δf is the frequency change due to an externally introduced mass load Δm . The standard unit of S_m is Hz/kg. Referring to Eq. 3.39 and Eq. 3.42, the relationship between S_m and S_M can be rewritten as:

$$S_m = -\frac{\Delta f}{\Delta m} = -\frac{f_0}{A} S_M \quad (3.43)$$

where f_0 is the resonant frequency before any mass is added onto the diaphragm, S_M is the gravimetric sensitivity, and A is the area of the diaphragm. Since the dimensions and material properties of the diaphragm are constant, Eq. 3.41 and Eq. 3.43 reveal that the gravimetric and mass sensitivity have been defined once the sensor is fabricated. The mass change is proportional to the detected frequency change and can be easily derived from Eq. 3.43 as:

$$\Delta m = -\frac{A}{S_M f_0} \cdot \Delta f \quad (3.44)$$

where f_0 is the resonance frequency which can be determined by using impedance analyzer. The mass change is independent of the tension status and the resonant behaviors of the diaphragm. Therefore, the mass of the biological entity captured by the bio-receptor is proportional to the resonance frequency change of the diaphragm, and can thus be calculated by the measured the resonant frequency change of the sensor. This result is quite significant in quantitative mass analysis using such a sensor.

To know more about the vibration behavior of the sensors, finite element analysis (FEA) using ANSYS software is conducted and the accuracy of the sensor sensitivity derived from Eq. 3.16 or Eq. 3.34 can also be further confirmed by the simulation. Since the gravimetric mass sensitivity is independent of the diaphragm shape, only circular diaphragm was considered during the simulation. The diaphragm consisted of several different layers, however, the thickness of the electrode was much smaller than that of the PZT and SiO₂ layer, hence, the diaphragm was simplified as a 0.8 μm-thick PZT layer on a 2 μm-thick silicon oxide layer as the sketch shown in Figure 3.3 during the simulation.

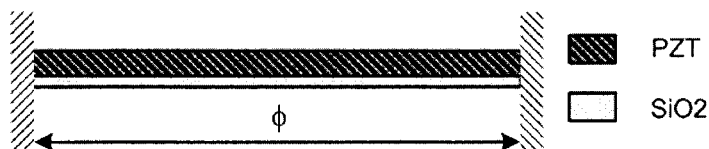


Figure 3. 3. Sketched cross sectional view of fully clamped double layer (SiO₂/PZT) diaphragm.

The mechanical properties of the PZT and SiO₂ layers used for the simulation are listed in Table 3.4. The initial tension usually induced by the residual stresses during the film deposition process, however, it is quite difficult to control or estimate the residual stress accurately during the microfabrication process.

Table 3. 4. Materials properties and theoretical calculated mass sensitivity [87].

Material	Young's modulus E (GPa)	Poisson ratio ν	Density ρ (10 ³ kg/m ³)
SiO ₂	72.4	0.16	2.07
PZT	86.2	0.287	7.62

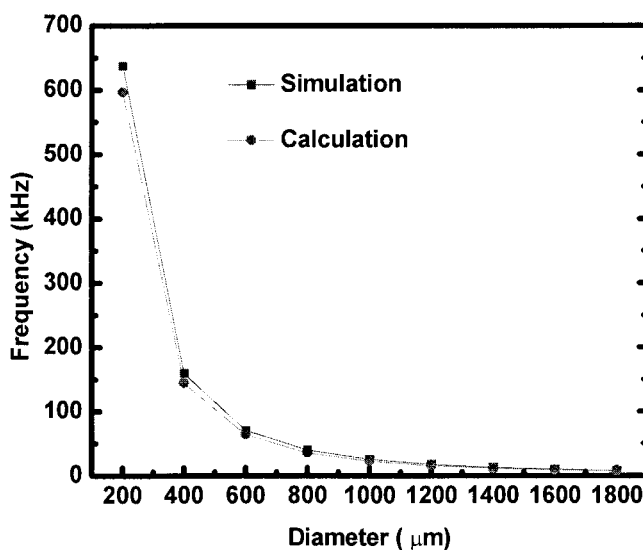


Figure 3. 4. Relationship between the resonant frequency and the diaphragm diameter.

Fortunately, the gravimetric sensitivity is independent of the resonant behaviors as we discussed in the previous part, hence, in this simulation, the tension is not considered and the diaphragm behaves as a plate in which the flexural rigidity (D) is dominant. Figure 3.4 shows the relationship between the resonant frequency (1st mode) and the diaphragm diameter. Both the simulation and calculation results show the resonant frequency decrease according to the diameter increase, thus, the diaphragm diameter needs to be properly designed in order to achieve a low working frequency. The calculated frequencies shown in the above figure are based on Eq. 3.2 and it can be seen that the simulation results are in agreement with those from the calculation. The frequency difference between the simulation and calculation is about 1.2 %. The first 4 vibration modes of the sensor are shown in Table 3.5. The resonant frequency of the sensor increases according to the order of the vibration mode; at the same time, the modal shape becomes more complex at high order vibration modes. Since the resonant frequency in the 1st mode is the fundamental and the simplest for a diaphragm based sensor, it will be the focus in this project. To analyze the frequency change after an external loaded mass, a uniformly distributed additional layer (0.1 μm thick) with the density of water ($\rho=1\times 10^3 \text{ kg/m}^3$) is added on top of the diaphragm as the added internal mass, corresponding to a mass loading (ΔM) of 10^{-5} g/cm^2 and $\Delta m = \Delta M \times A$. The calculated and simulated gravimetric sensitivity (S_M) and mass sensitivity (S_m) are evaluated based on Eq. 3.41, Eq. 3.39, Eq. 3.43 and Eq. 3.42, respectively.

Table 3. 5: The first four vibration mode of the circular diaphragm.

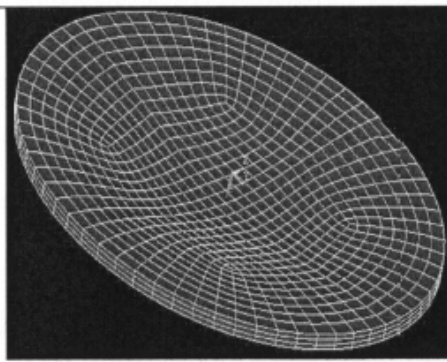
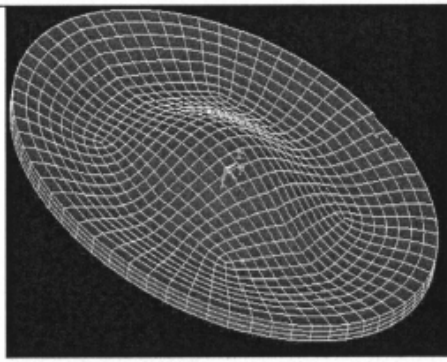
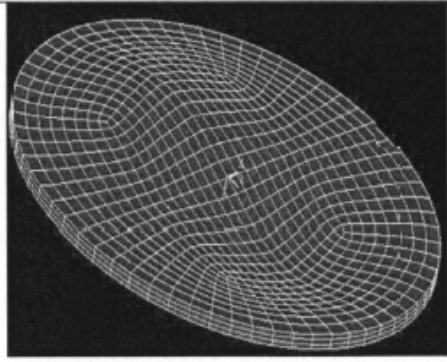
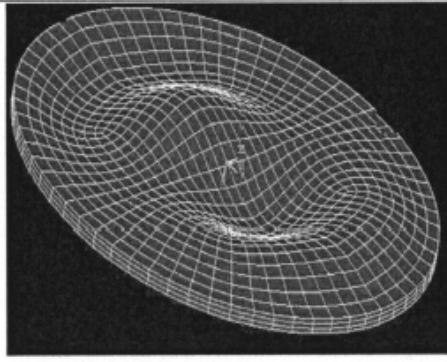
Circular node(s)	Diametrical node (n)	
	0	1
1		
2		

Table 3.6 shows the simulated and calculated sensitivities of the sensors with different diameters. It shows that the size of the diaphragm (ranging from 200~1800 μm) does not affect the gravimetric sensitivity $S_M (\pm 0.05 \text{ m}^2/\text{kg})$ much although the unloaded resonant frequency f_0 decreases with increasing the diaphragm size. It can be concluded that the gravimetric sensitivity (S_M) is independent of the size of the diaphragm. This result is also presented in Figure 3.5 (a).

Table 3. 6: Mass sensitivity of the sensors obtained by theoretical calculation and FEA simulation.

ϕ (μm)	A (mm^2)	f_0 (kHz)	f (kHz)	Δf (kHz)	Δm (ng)	FEA S_M (m^2/kg)	Cal. S_M (m^2/kg)	FEA S_m (Hz/ng)	Cal. S_m (Hz/ng)
200	0.0314	637.56	634.469	3.093	3.14	48.513	48.845	984.4	985.03
400	0.1256	159.88	159.104	0.776	12.57	48.536	48.845	61.75	62.17
600	0.2826	71.164	70.8192	0.345	28.27	48.493	48.845	12.21	12.3
800	0.5024	40.081	39.8865	0.194	50.27	48.477	48.845	3.87	3.89
1000	0.785	25.685	25.5603	0.125	78.54	48.472	48.845	1.59	1.59
1200	1.1304	17.871	17.7839	0.087	113.10	48.515	48.845	0.77	0.77
1400	1.5386	13.181	13.1175	0.064	153.94	48.477	48.845	0.42	0.42
1600	2.0096	10.181	10.1317	0.050	201.06	48.521	48.845	0.25	0.25
1800	2.5434	8.201	8.16122	0.040	254.47	48.482	48.845	0.16	0.16

The average S_M obtained by FEA is around $48.5 \text{ m}^2/\text{kg}$, which agrees well with the theoretically calculated S_M ($48.8 \text{ m}^2/\text{kg}$) obtained by Eq. 3.41. The negligible difference between them is attributed to the following fact: in the FEA, E , ν and ρ are considered, however, only ρ and d (thickness) are used to calculate S_M by Eq. 3.41. Therefore, Eq.3.41 can be used to predict the designed biosensor's gravimetric sensitivity. Moreover, based on Eq.3.41, the sensitivity can only be affected by the thickness and density of different layers within the diaphragm. Theoretically, the thinner diaphragm layer leads to a higher sensitivity. However, if the diaphragm is too thin, the fabrication reliability and the piezoelectric properties will be compromised. As a trade-off for the above concerns, the optimized diaphragm thickness in this project will be about $1 \mu\text{m}$.

Since the diaphragm diameter can't be determined by Eq. 3.41, the normalized mass sensitivity will be used to investigate the relationship between the sensitivity and the diaphragm size. Both the simulated and calculated mass sensitivities (S_m) shown in the above table have very small variation, indicating that the sensitivity defined by Eq. 3.43 are accurate. It can be found from the table that the mass sensitivity (S_m) decreases as the diaphragm diameter increases, however, the mass sensitivity is not affected much by the diameter change when the diameter exceeds 1200 μm . This is because the diaphragm becomes more flexible as the diameter increases; hence, under the same stress condition, the diaphragm is not sensitive to a loaded small mass. As such, the diameter of the diaphragm should be designed to be small to achieve a high mass sensitivity. However, on the other hand, if the size of the reaction chamber is too small, the solutions containing biological materials may not be able to flow into the reaction chamber due to capillary phenomenon, which makes the immobilization process more challenging. Therefore, by considering the sensitivity and the immobilization process, the diameter size will be designed from 600 to 1000 μm in this project.

The mass sensitivity (S_m) of the diaphragm can also be studied through the theoretic analysis. Referring to Eq.3.2, Eq.3.42 can be rewritten as:

$$S_m = f_0 \times S_M \times \frac{1}{A} = \frac{\lambda^2}{2\pi R^2} \sqrt{\frac{D}{\rho t}} \times S_M \times \frac{1}{\pi R^2} \quad (3.45)$$

$$S_m \propto \frac{1}{R^4} \quad (3.46)$$

when other parameters such as λ , D and t remain the constant, Eq. 3.45 can be rewritten as Eq. 3.46 which implies that the mass sensitivity is inversely

proportional to R^4 , where R is the radius of the diaphragm. The result is plotted in Figure 3.5.

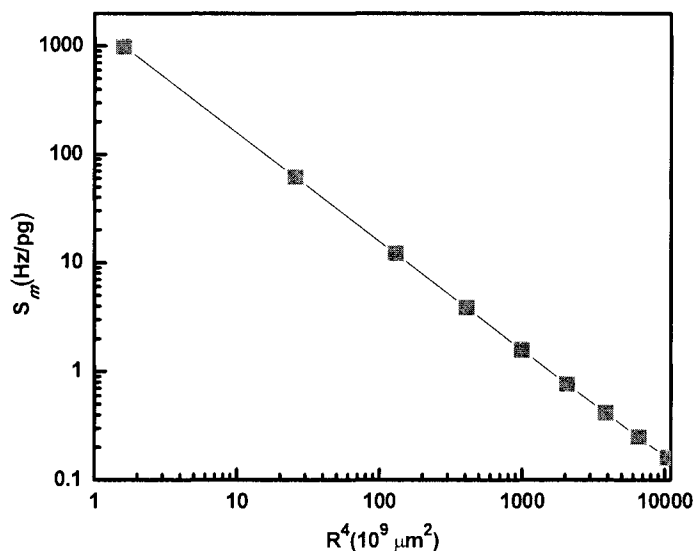


Figure 3.5. The relationship between the mass sensitivity (S_m) and the diaphragm size.

The optimized parameters for a mass biosensor are summarized in Table 3.7.

Table 3.7: Optimized parameters for the diaphragm based biosensor.

Diameter (μm)	PZT Thickness (μm)	Density ρ (10^3 kg/m^3)
600-1000	1	Depends on individual layer

3.4 Summary of this chapter

In conclusion, the sensitivity of the designed biosensor depends on the thickness, density and size of the diaphragm. The above study shows that the diaphragm in the sensor should be designed to be thin and small with low density to

achieve a high sensitivity. By considering the sensitivity and difficulty of biomaterial immobilization, the designed diaphragm diameter varies from 600 μm to 1000 μm with a thickness of about 1 μm .

Chapter 4

Micro-machined piezoelectric diaphragm based immunosensor array

This chapter reports two types of micro-machined piezoelectric diaphragm-based biosensor arrays for immunoassays. The fabrication processes and characterization are discussed in detail. The first square-type sensor array successfully detected anti-goat immunoglobulin G (IgG) with a mass sensitivity of 6.25 Hz/ng. The second circular-type sensor array was developed to increase the sensitivity and the fabrication yield. After optimizing the fabrication and immobilization processes, it is demonstrated that the immunosensor chip is able to simultaneously detect HBsAg and α -protein with a mass sensitivity of 16.05 Hz/ng, which is more than two times higher than that of the square sensor array. The preliminary results discussed in this chapter indicate that the micro-machined piezoelectric diaphragm-based biosensors have very compact size, high sensitivity, high quality factor, rapid response and have a potential application as immunosensors.

4.1 Background of bulk micromachining

As discussed in the literature review in Chapter 2, we will develop square and circular piezoelectric diaphragm-based biosensor arrays. The diaphragm can be

Chapter 4 Micro-machined piezoelectric diaphragm based immunosensor array

released either by wet etching or dry etching. In wet bulk micromachining, features are sculpted in the bulk of materials by using orientation dependent (anisotropic) or orientation-independent (isotropic) wet etchants. Due to the good single crystal characteristic of silicon, the silicon substrate can be anisotropically etched due to the different etch rates along different crystal planes. The classic anisotropic etchant for silicon is KOH solution. Etch rate towards $\langle 111 \rangle$ crystal plane direction is much slower than that towards $\langle 100 \rangle$ crystal plane direction due to the different densities of covalent bonds. As a result, an inverted-pyramid pit will be formed and these structures facilitate the bio-immobilization as the open surface is much larger than that in the bottom. In addition, wet etching process is simple and the fabrication cost is low. It will be firstly used in this project to fabricate the square shape diaphragm based biosensors.

Deep reactive ion etching (DRIE) of silicon is another micromachining technique; it allows perfectly vertical sidewall angles and randomly shaped linear geometries. DRIE is capable of anisotropic etching high aspect ratio trenches and is an alternative process of etching and passivation. SF_6 is used to etch silicon in the etching cycle and a thin fluorocarbon polymer which is deposited using C_4F_8 as a source gas in the passivation cycle. In the followed etching cycle, energetic ions (SF_x^+) remove the protective polymer at the bottom of the trench. The repetitive alternation between etch and passivation steps results in a vertical sidewall for deep etching in the substrate. Hence, in the second stage of this project, the DRIE will be used to develop circular shape diaphragm based biosensor array.

In addition, the circular sensor array was able to detect multiple biological materials simultaneously. After the characterization, it was verified that the sensor

Chapter 4 Micro-machined piezoelectric diaphragm based immunosensor array

array developed in the work can potentially be used as an immunosensor. The detailed fabrication process and characterization results are introduced in the following sections.

4.2 Squared biosensor array

4.2.1 Fabrication processes

The piezoelectric diaphragm-based biosensor array was fabricated using standard bulk micromachining fabrication techniques. As shown in Figure 4.1, there are 10 main steps involved: (1) A thermal silicon oxide (SiO_2) layer (1.8 μm thick) was grown on a 4-inch double sided polished silicon wafer. (2) A silicon nitride (Si_3N_4) layer with a thickness of 200 nm and a lower temperature oxide (LTO) layer with a thickness of 350 nm were then deposited by low pressure chemical vapor deposition (LPCVD) on both sides of the wafer. The Si_3N_4 layer was used to compensate the residual stress from the SiO_2 film and the LTO layer was used as the hard mask during the Si wet etching process. (3) To open a window for backside silicon etching, the LTO and $\text{Si}_3\text{N}_4/\text{SiO}_2$ layers were etched by buffered oxide etching (BOE) and reactive ion etching (RIE). (4) After patterning, KOH wet etching was performed until the remaining thickness of silicon was about 50 μm . This remaining Si film makes the substrate more solid during the subsequent process. (5) Ti/Pt (20/200 nm) layers were sputtered, patterned and used as bottom electrode.

Chapter 4 Micro-machined piezoelectric diaphragm based immunosensor array

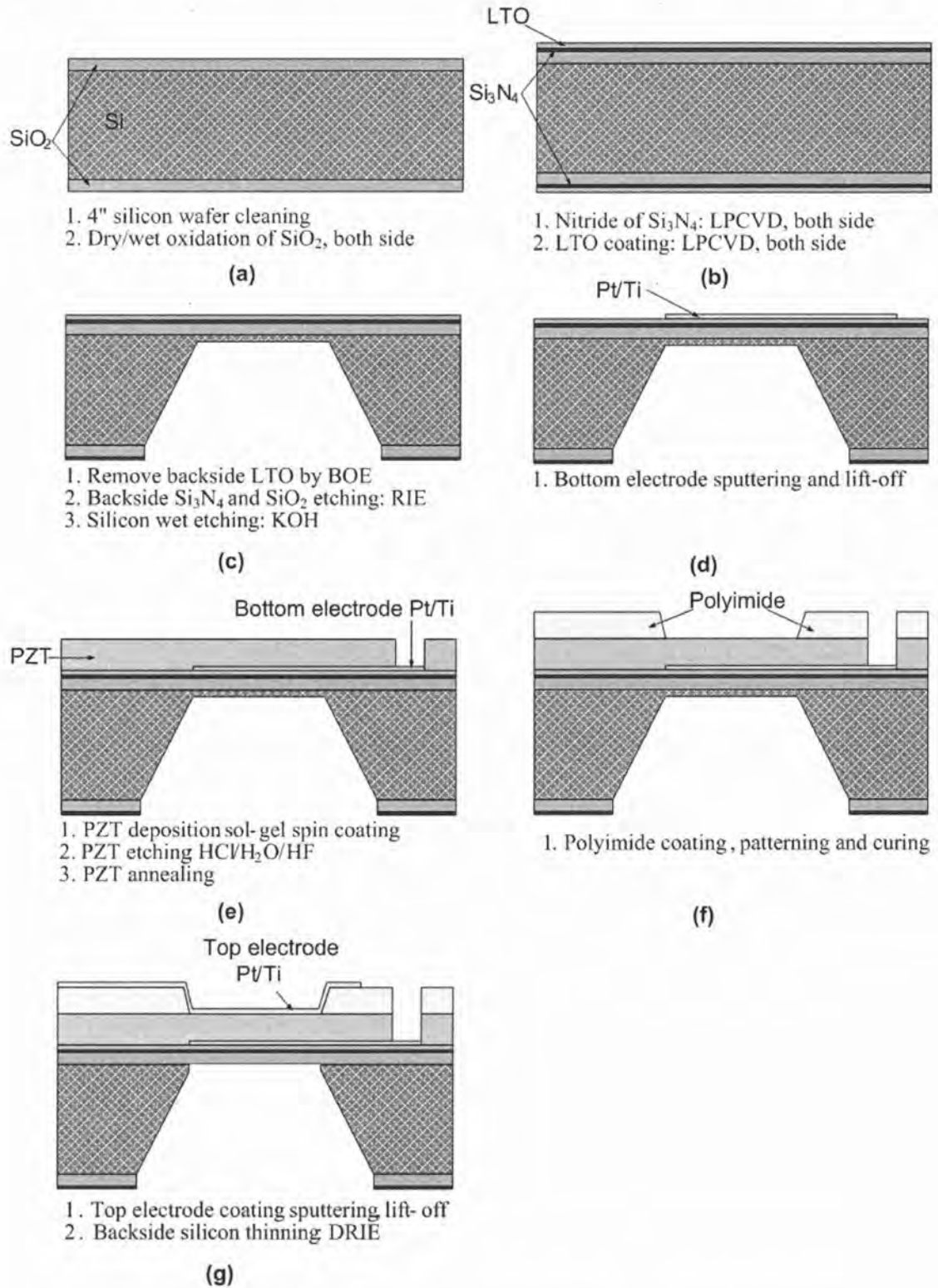


Figure 4.1. Schematic fabrication process for the square piezoelectric sensor.

Chapter 4 Micro-machined piezoelectric diaphragm based immunosensor array

(6) $\text{Pb}(\text{Zr}_{0.52}\text{Ti}_{0.48})\text{O}_3$ (PZT) was used as the piezoelectric material for actuating the sensing diaphragm. A thick PZT layer with a required thickness of around $3.5 \mu\text{m}$ was deposited by the composite thick film deposition technique [88-89]. (7) Wet etching of the PZT in diluted $\text{HCl}:\text{HF}:\text{H}_2\text{O}$ (50:1:50) solution was done to expose the bottom electrode pad. (8) A polyimide layer was spin-coated, patterned and cured as an insulation layer to minimize parasitic capacitance induced by the patterned electrode wiring. (9) Ti/Pt (20/200 nm) layers were sputtered and patterned on the front side by using lift-off to serve as the top electrode. The metal top and bottom electrodes are firstly used to polarize the piezoelectric film and electrical pads during the testing. (10) The remaining thin Si layer on the backside was etched by KOH or DRIE till the SiO_2 layer was exposed.

4.2.2 Fabrication results

By using the micromachining processes described above, the diaphragm-based piezoelectric biosensor array was successfully fabricated. As shown in *Figure 4.2* (a), each array consists of 7 individual sensors which are located in a hexagonal shape. Each square block is actually a single sensor and can be individually actuated through the PZT film. The backside of the array, which shows the reaction chambers, is illustrated in *Figure 4.2* (b). The width of the sensor bottom was about 0.51 mm, which was close to the designed value (0.5 mm). The opening area of the chamber was much larger than that of the bottom diaphragm due to the anisotropic wet etching by KOH. The subsequent biomaterial immobilization processes such as

Chapter 4 Micro-machined piezoelectric diaphragm based immunosensor array

the dipping and washing of the biomaterial, were much more convenient because of this enlarged opening area.

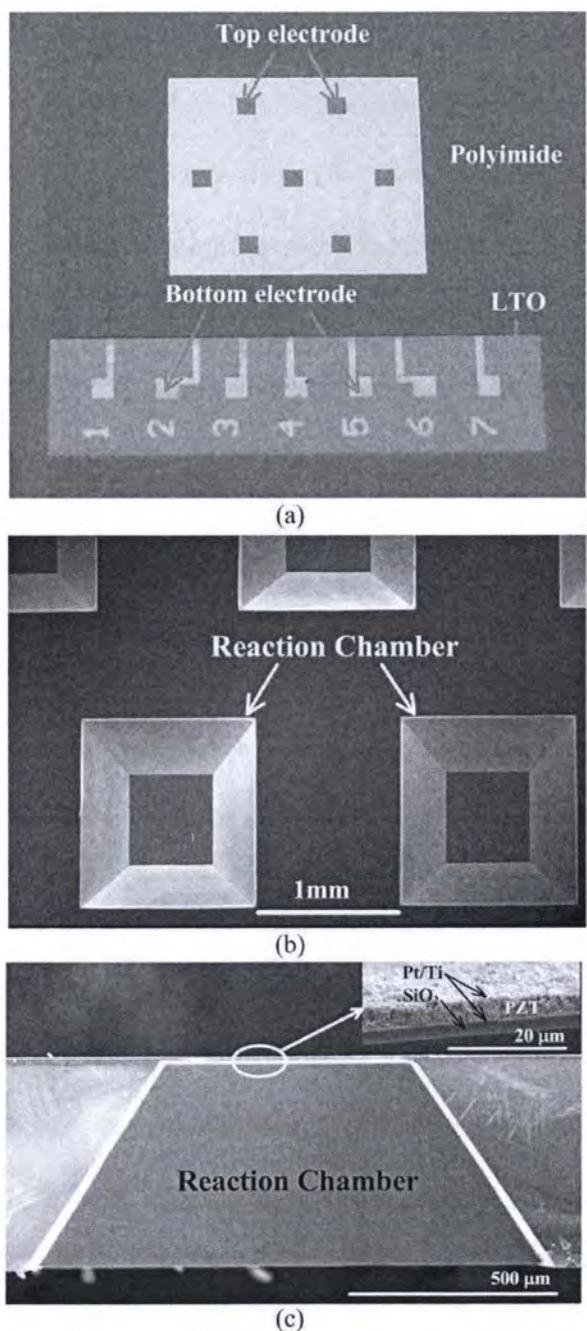


Figure 4.2. Images of the fabricated sensor array, (a) optical image in top view, (b) SEM of the reverse side, (c) cross sectional SEM of one sensor and the insert is the SEM of the detailed PZT membrane structure.

Chapter 4 Micro-machined piezoelectric diaphragm based immunosensor array

Figure 4.2 (c) shows the detailed multilayer structure made on the front side of the silicon wafer. The PZT layer is about 3.5 μm in thickness, the backside silicon was completely etched out, and the $\text{Si}_3\text{N}_4/\text{LTO}$ is invisible because its thickness is too thin to be observed in this magnification. Although some good devices were successfully fabricated, the fabrication yield (< 20%) is very low. This yield is calculated by the percentage of numbers of the functional sensors after fabrication over the numbers designed on the masks. One of the reasons lies in the fact that only very thin SiO_2 layer ($\sim 50 \text{ nm}$) remained after the wet etching in the third step, thus, the stress generated from the fabrication process could deform the thin diaphragm.

This makes the subsequent film deposition non-uniform and some of the films were even peeled off. Another possible reason lies in the fact that many of the thin diaphragms with high stress were broken or deformed during the washing process after the wet etching process in the last step.

4.2.3 Biomaterial immobilization

The coupling effect between antigen-antibody is actually a key-lock reaction, in which an individual antibody combining site can only react with one antigenic determinant. Due to this high degree of specificity, antigen-antibody reaction is one of the more popular techniques for immunosensor applications [26]. In this work, two different biological entities, goat IgG and HBsAg, were used to verify the feasibility of applying this sensor as an immunosensor.

Chapter 4 Micro-machined piezoelectric diaphragm based immunosensor array

Among the numerous reported immobilization methods, immobilizing proteins onto gold surface via physical adsorption, due to their hydrophobic properties, is undoubtedly the simplest and quickest way [90-92]. Since the bonding between the gold film and protein is of a non-covalent nature, it allows the multiple washing and makes the sensing device reusable [92]. The schematic of biological material immobilization is depicted in *Figure 4.3* and implemented by a simple yet reliable dip and dry process [93].

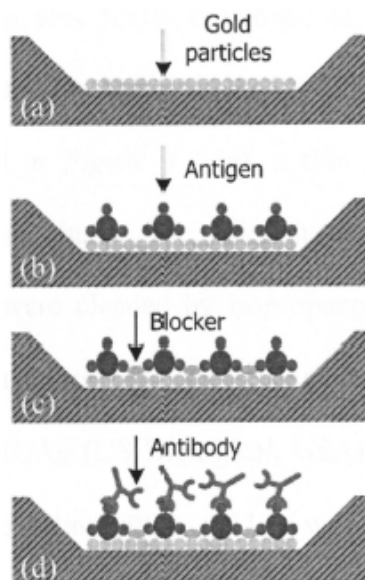


Figure 4.3. Schematic processes of immobilizing. (a) Thin gold film was deposited onto the diaphragm through sputtering process. (b) Different antigens (goat IgG and HBsAg) were immobilized onto the diaphragm. (c) Blocking the open surface by Blocker Casein in TBS. (d) Hybridization of antigens and antibodies (anti-goat IgG and anti-HBsAg).

(i) Effect of process time on the binding activity of the immobilized antigens

Since the sensor chip after immobilizing with biomaterials needs to be dried out before measuring the resonant frequency, it is necessary to study the binding activity of the immobilized antigens after exposure to the air during the measuring process. This is critical to effectively and reliably capture the antibody in the last step. Hence, one sensor chip was firstly employed to investigate the effect of process time on the binding activity before starting the immobilization process for the biosensors. As described in *Figure 4.3 (a)*, a thin gold film (~50 nm) was sputtered onto the diaphragms inside the reaction chambers in the first step. Afterwards, the diaphragms were cleaned by isopropanol (IPA) and dried out by nitrogen (N₂) gas. For the demonstration, only HBsAg was used as the receptors for the seven sensors. 1 μl of HBsAg (US Biological, USA) with concentration of 20 μg/ml in phosphate buffered saline (PBS, pH7.4) was added into each reaction chamber (*Figure 4.3 b*). The chip was placed on a vibrator with horizontal movement to facilitate the proteins attached onto the gold surface. After 30 min of reaction at room temperature, the excess or unattached HBsAg were washed away by carefully-injected tris-buffered-saline (TBS washing buffer, pH8.0) (*Figure 4.3 c*) followed by de-ionised (DI) water cleaning. The HBsAg functionalized surfaces were dried under N₂ flow. 1 μl of Blocker™ Casein in TBS (Pierce, Germany) with a concentration of 1 mg/ml was dropped into each chamber and incubated in the culture chamber (~ 37 °C) for 30 min to block the open surfaces.

Chapter 4 Micro-machined piezoelectric diaphragm based immunosensor array

The blockers and the HBsAg were again washed by DI water and dried with N₂. In order to investigate the time factors on the frequency shift, 1 μl of anti-HBsAg (Sigma, USA) with concentration of (100 μg/ml) in PBS was added into the first sensor after exposing it in air for 15 min. After reacting for 30 min, the anti-HBsAgs were bonded with the immobilized HBsAgs and the un-bonded anti-HBsAgs were washed away using TBS and DI water. Anti-HBsAgs with the same concentration were then added into sensor 2 and 3, 4 and 5, 6, 7 after drying for 30, 45, 60, and 75 min, respectively. Since the drying time of 30 and 45 min are crucial in the bio-immobilization process, 2 sensors with the same concentration were used to ensure the accuracy of the results.

The resonant frequency of each sensor was measured after the last step and the equipment set up will be introduced in section 4.2.4. The frequency of each sensor was measured for 3 times and the frequency shift was plotted in *Figure 4.4*. An average measurement value from two sensors was used for the drying time of 30 and 45 min. The seven sensors in the chip have a similar resonant frequency and they will ideally have a comparable frequency shift after different time delays before the bio-immobilization. The frequency shifts for sensor 1, 2 and 3 are 890 and 880 Hz, respectively. It is clear that within 30 min of drying, the variation (0.11%) of frequency shift due to the time exposed to air is negligible. However, significant frequency shift shrinks are observed after 45 min of drying. The frequency shift of the sensors drying for 45, 60 and 75 min are 780, 250, and 80 Hz which are 87.6, 28.1, and 8.9% of the frequency shift at 15 min. These indicate that the binding activities of the HBsAgs decayed as the time expose to dry air increased [94-96]. Only a very small amount of antibodies were captured due to the antigens

Chapter 4 Micro-machined piezoelectric diaphragm based immunosensor array

losing their original binding activities after the long time (> 45 min) exposure to air in dry condition. Hence, it can be concluded that the antigens immobilized in the second step as described in section 4.2.3 still remained in active conditions when the drying time was less than 30 min.

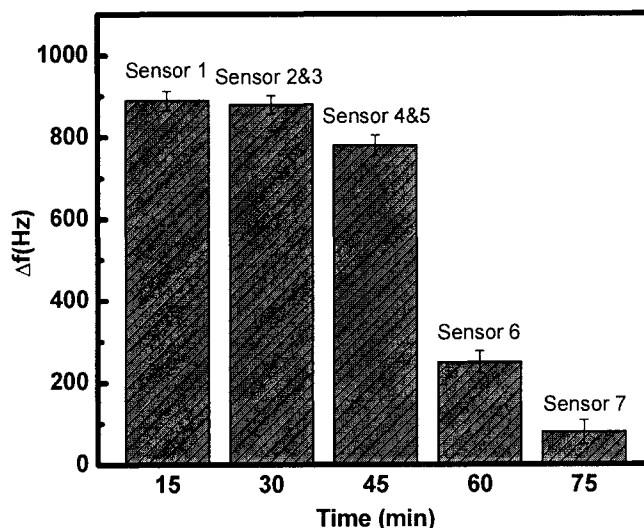


Figure 4.4. Processing time effect on the frequency change.

(ii) Immobilization of goat IgG onto the biosensor array

Goat IgG and HBsAg were immobilized onto the diaphragm surfaces to serve as receptors after verifying the time effect on the protein binding activity. The immobilization processes and parameters, including gold deposition, are exactly the same as the above section. In the first immobilization process, sensors 1 to 4 were immobilized with goat IgG (1 $\mu\ell$) with different concentrations. The concentrations of the added goat IgG for the four sensors were 25 $\mu\text{g}/\text{mL}$, 50 $\mu\text{g}/\text{mL}$, 100 $\mu\text{g}/\text{mL}$, and 200 $\mu\text{g}/\text{mL}$, respectively. To investigate the effect of washing processes on the sensor resonant frequency, sensor 5, 6 and 7 were used as the references, which

Chapter 4 Micro-machined piezoelectric diaphragm based immunosensor array

underwent all the same washing and drying process but no biomaterial was immobilized onto them. All the sensors were washed by TBS and dried by N₂ after 30 min of reaction at room temperature. Afterwards, 1 μl of BlockerTM Casein (1 mg/ml) was dropped into each chamber to block the open surfaces.

In the last step, 1 μl of anti-goat IgG (100 $\mu\text{g}/\text{ml}$) were added into each reaction chamber in sensors 1 to 4 accordingly. The sensor chip was washed and dried after 30 min. The resonant frequency of each sensor was measured and each measurement took an average time of about 2 min. In other words, it took about 14 min to complete the measurement for the whole chip, so even the antigens immobilized in the last sensor were still in an active condition to capture the antibodies. It can be seen that the total experimental time was less than 2 hr, which was much faster than other reported times [42], typically 7 to 12 hr, or even longer to complete the process.

4.2.4 Characterization of the immunosensor array

The piezoelectric diaphragm based biosensors can be characterized using an impedance spectrum, which is also one of the advantages of the piezoelectric biosensors. The Agilent 4294A impedance analyzer was used to test the fabricated biosensors. A probe station was used to connect the analyzer and the wiring pads of the sensors. *Figure 4.5* shows the equipment setup for measuring the resonant frequency of the sensor array, where the sensor array was placed on a probe station, which was attached to a microscope. Due to the mass sensitive nature of the

Chapter 4 Micro-machined piezoelectric diaphragm based immunosensor array

fabricated sensors, the resonant frequencies of the sensors shift to the lower frequency domain. After the external materials, such as gold film, goat IgG, and blockers, were attached onto the sensing surfaces of biosensors.

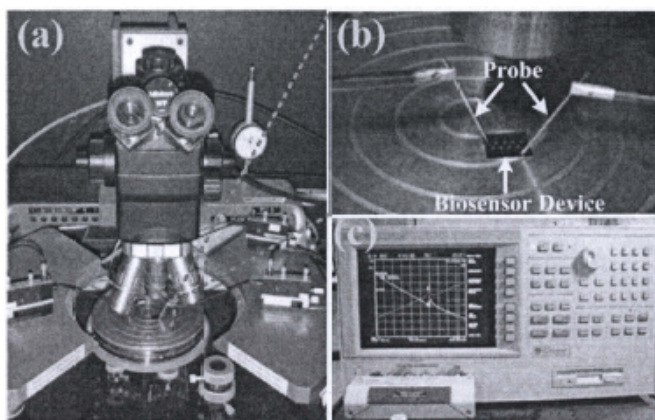


Figure 4.5. Equipment setup for measuring the resonant frequency of the sensor array. (a) A probe station with microscope, (b) the enlarged view of the sensor chips with connection to the two probes, (c) an Agilent 4294A impedance analyzer.

To have a detailed study on this relationship, the resonant frequencies of the sensors were measured immediately after each immobilization or reaction process. Although mass deposition on the sensing surface is the dominant factor affecting the resonant frequency of piezoelectric sensor, it has been reported that the resonant frequency is also influenced by the external environmental factors including medium types, viscosity and humidity of the medium, incubation temperature [97, 98]. Hence, in order to ensure that the immunochip has a good performance and minimize the external effect on the frequency, all the measurements were conducted in gas phase in a class-100 clean room to avoid any tiny particles depositing onto the sensing surface. Inside the clean room, the temperature and relative humidity was kept at 23 °C and 35%, respectively. A vertical laminar flow was maintained within the clean room.

(i) Quality factor

Quality factor (Q value) is one of the key factors to affect the mass sensitivity (S_m). Q value defines the sharpness of the resonance peak [99]. The higher Q value means the resonance peak in the frequency-amplitude diagram is high and narrow, giving a higher precision in determining resonant frequency and a smaller minimum detectable frequency change [100]. The Q value in this work is defined as $f_0/\Delta f$, where f_0 is the resonant frequency of maximum amplitude response, and Δf is the width of the peak at its half height [101]. We fitted the measured impedance peak using Lorentz function to get Δf and f_0 for calculating the Q value [1]. *Figure 4.6* shows the first mode of resonant frequency spectrum of sensor 1 at each immobilization step.

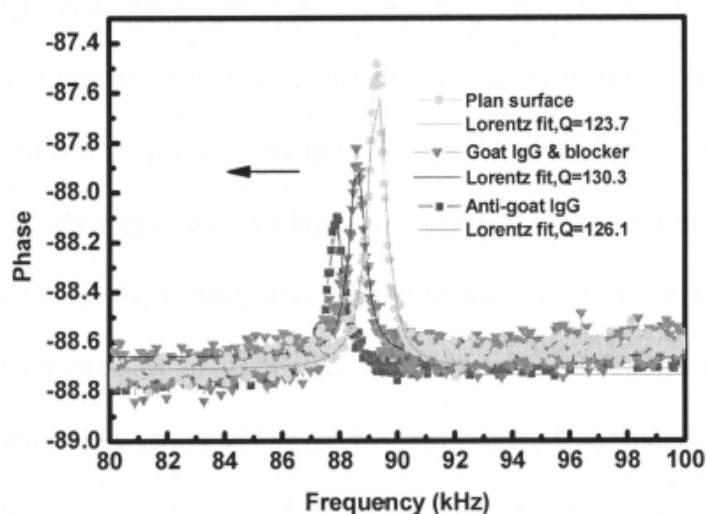


Figure 4.6. Frequency change of sensor 1 after goat IgG & blocker and anti-goat IgGs were immobilized or captured.

Chapter 4 Micro-machined piezoelectric diaphragm based immunosensor array

The Q value obtained from the plane surface, blocker and anti-goat IgGs are 123.7, 130.3 and 126.1, respectively. The Q factor in current stage is sufficient to have a high resolution and further optimization is not likely needed. It can also be seen that the amplitude of the frequency peak in Figure 4.6 decreased as more biomaterials were added onto the sensing surface, this is possibly due to the soft and viscous proteins being well bonded to the diaphragm surface and changed its elasticity. Another reason may be attributed to the damping effect from the thin protein film, which serves as a buffer layer during the vibration [102-104]. This also may be the reason why there is a slight change in Q values at different processes.

(ii) Resonant frequency of the sensor array

The first reference resonant frequency (f_1) was measured after the thin gold layer was deposited, and the second resonant frequency (f_2) was measured after the goat IgGs were immobilized. Hence, the first frequency shift was calculated as $\Delta f_1 = f_1 - f_2$. The resonant frequency after immobilizing blocker (f_3) and anti-goat IgGs (f_4) were subsequently measured. The last two frequency shifts were calculated as $\Delta f_2 = f_2 - f_3$ and $\Delta f_3 = f_3 - f_4$, respectively. All the measurements were conducted in gas phase with a temperature of 30 °C. The results from the 4 sensors show the similar frequency depression trend and Figure 4.6 presents the frequencies of sensor 1 with a plain sensing surface (f_1), goat IgG and blocker (f_3), and anti-goat IgG (f_4). The frequency change varies from 100 to 700 Hz. Figure 4.6 clearly shows that the frequency decreased after each type of biological entity was immobilized or

Chapter 4 Micro-machined piezoelectric diaphragm based immunosensor array

adsorbed. The resonant frequencies of the sensors were measured at a low frequency range (80-150 kHz), thus the cost of measurement equipments are lower than that of high frequency measurement equipments. This is another merit of the sensors developed in this work.

(iii) Calibration

Usually, during investigation of a calibration curve, probe molecule (Goat IgG in this work) with the same concentration is first immobilized on different sensors, while in the last step, the target molecule (Anti-goat IgG) with different concentration is detected. Due to the limited binding sites in the immobilized goat IgG, if the concentration of the anti-goat IgG increases to a certain level, the redundant anti-goat IgG is not able to be captured by the goat IgG, hence a saturation adsorption occurs.

In this work, however, a different immobilizing process was used. Goat IgG was immobilized with different concentrations (25-200 $\mu\text{g}/\text{m}\ell$) in the first step; therefore the numbers of goat IgG binding sites were proportional to the concentration of the solutions. In the last step, anti-goat IgG was applied onto the sensor surface with a relatively high concentration. This sufficiently high concentration of anti-goat IgGs ensures that all the binding sites in the goat IgGs were occupied by anti-goat IgGs. Due to the specific interaction between antigen and antibody, the amount of the anti-goat IgGs captured by the goat IgG binding sites is theoretically proportional to the concentration of immobilized goat IgG.

Chapter 4 Micro-machined piezoelectric diaphragm based immunosensor array

Therefore, a nearly linear relationship between the frequency shift (after anti-goat IgGs were captured) and the concentration of the immobilized goat IgG is expected. This is only valid in the condition that the applied anti-goat IgG concentration did not exceed the value that saturates the binding sites in the goat antigens.

The advantage of our immobilization method is that, the capability of the new biosensors for the detection of added mass and performance uniformity can be proved after the first immobilization process. Based on Eq.3.2 or 3.3, it can be seen that the resonant frequency of the sensor should be changed after the external mass is added and the frequency shift is proportional to the mass change. In this work, the added mass in the first step is actually the mass of the immobilized goat IgG, which is proportional to the concentration of its solution. After the goat IgGs with concentrations of 25 $\mu\text{g/ml}$, 50 $\mu\text{g/ml}$, 100 $\mu\text{g/ml}$ and 200 $\mu\text{g/ml}$ were immobilized on the four different sensors, the frequency shifts were measured to be 150 Hz, 258 Hz, 530 Hz and 1100 Hz, respectively. The frequency shift is nearly proportional to the concentration of immobilized goat IgG, indicating that the sensor array is mass sensitive and the performances of the sensors are reasonably uniform. After the mass sensitive feature of the sensor array was confirmed, we further evaluated the immunoassay performances of the array by applying the anti-goat IgG.

The dose/signal curve was plotted in *Figure 4.7 (a)*, where the frequency shifts were calculated based on the average frequency values after 5 measurements. In the tested goat IgG concentration range of 25-200 $\mu\text{g/ml}$, a nearly linear relationship between the frequency shift (after anti-goat IgGs were captured) and the

Chapter 4 Micro-machined piezoelectric diaphragm based immunosensor array

concentration of goat IgG was found. This reveals that a higher concentration of goat IgG added onto the sensor in the first immobilization process will result in a larger frequency shift after capturing the anti-goat IgG in the last step. This is mainly because more goat IgG binding sites were available in higher concentrations of immobilized goat IgG to capture anti-goat IgGs.

The resonant frequencies of the reference sensors have negligible variations (< 50 Hz) during the washing process. This reveals that washing process has a negligible effect on the sensor's frequency. This also indicates that nonspecific adsorption is not significant in this immobilization processes. The gravimetric sensitivity (S_M) of the fabricated sensors was calculated to be $-16.5 \text{ m}^2/\text{kg}$ by Eq.3.40 based on the parameters listed in Table 4.1. During the calculation, effects from the top and bottom electrode were ignored due to the very thin thickness (< 200 nm) compared to that of PZT and SiO_2 layers.

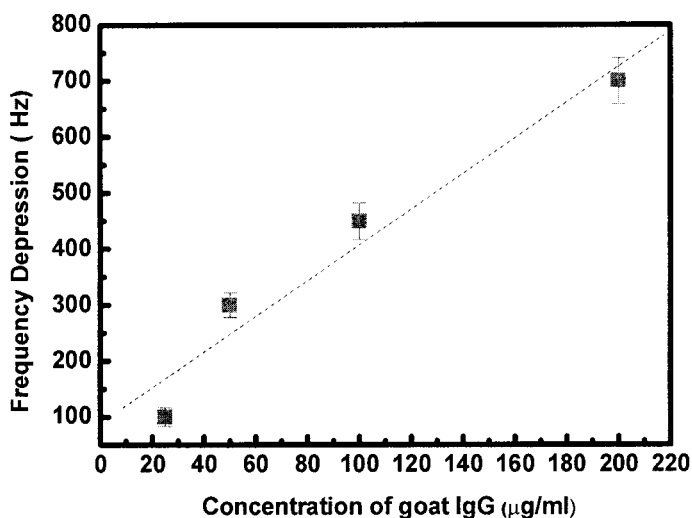
Table 4.1. Material properties of different films in the micro-diaphragm

Layer	ρ (kg/m ³)	d (μm)
SiO ₂	2070	1.8
LTO (SiO ₂)	2070	0.35
PZT	7620	3.5

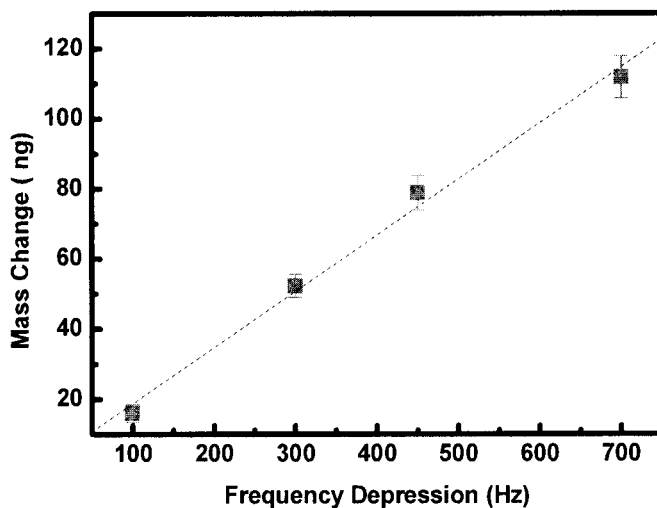
The reference frequency (f_0) in the equation was measured after the blocker immobilization and the frequency change (df) was calculated as $\Delta f_3 = f_3 - f_4$. Based on Eq.3.44 together with the calculated surface area ($A = 500 \mu\text{m} \times 500 \mu\text{m}$), the mass of the captured anti-goat IgG by the four sensors were calculated to be 16.1 ng, 52.3 ng, 78.2 ng and 108 ng, respectively. This result proves that the sensor array

Chapter 4 Micro-machined piezoelectric diaphragm based immunosensor array

developed in this work can detect the mass of the bio-materials in quantity. The linear relationship between the calculated mass and the frequency change is presented in Figure 4.7 (b).



(a)



(b)

Figure 4.7. Relationship between frequency depression, concentration of goat IgG and mass change for the 4 sensors, (a) Relationship between the frequency depression and the concentration of goat IgG, (b) Relationship between the mass change and frequency depression after the anti-goat IgGs were captured.

Chapter 4 Micro-machined piezoelectric diaphragm based immunosensor array

This result is well consistent with the conclusion by Eq. 3.10, and justifies that the performances of the sensors in this array were quite uniform. From the gradient of Figure 4.7 (b), the average mass sensitivity of these 4 sensors was calculated to be 6.25 Hz/ng.

The mass of the immobilized blocker can also be calculated by Eq.3.10 and was much smaller than that calculated by the added concentration and volume. This reveals that the majority of the sensor surfaces were occupied by the goat IgG and there were not many open surfaces for the blockers to attach onto. Hence, it can be concluded that the mass change in the last step was mainly due to the captured anti-goat IgG. This ensures the accuracy of the anti-goat IgG detection. The primary results obtained in these experiments proved to be meaningful in the detection of small quantities of biomaterials.

In this section, a micromachined mass-sensitive square piezoelectric diaphragm-based biosensor array was developed. The preliminary results demonstrated the possibility of using this immunosensor to rapidly detect model targets of anti-goat IgGs. Unfortunately, the square diaphragm by wet etching has very low fabrication yield (< 20%). It also has large die areas due to the inverted-pyramid opening surface, which will increase the fabrication cost and limit its practical applications. More over, the sensitivity is relatively low probably due to the fact: the total thickness of the diaphragm includes the 3.5 μm thick PZT film and other thin films are relatively thick (6.3 μm), according to the definition, the gravimetric sensitivity is inversely proportional to the total thickness of the diaphragm, and the mass sensitivity is depending on the gravimetric sensitivity, hence, the thick diaphragm

Chapter 4 Micro-machined piezoelectric diaphragm based immunosensor array

leads to a mass sensitivity. Beside the low fabrication yield and sensitivity issue, the multiple analytes detection is not demonstrated yet. Hence, it is necessary to make a new sensor design, optimize the fabrication and immobilization processes to achieve a high yield and sensitivity, and simultaneously detect multiple biological entities.

4.3 Circular biosensor array

In this section, a novel thin piezoelectric circular diaphragm-based immunochip was developed to simultaneously detect the model analyte of hepatitis B virus (HBV) and α -fetoprotein (AFP). The detailed fabrication processes and characterization results are presented in the following sections.

4.3.1 Fabrication processes

With the conclusions drawn from Chapter 3, the circular sensor structure and fabrication processes were designed to be much simpler than the square sensor. The total thickness of the multi-layer diaphragm and its size are also designed to be thin and small. The piezoelectric sensor array was fabricated with a similar process as discussed in section 4.2.1 besides some other optimizations. As shown in *Figure 4.8*, firstly, a thin TiO₂/Pt (15/200 nm) film was sputtered on the top side of a 4 inch silicon-on-insulator (SOI) wafer as the bottom electrode. SOI wafer, which has a device layer of 2 μm and SiO₂ layer of 0.5 μm , was used to reduce the residual

Chapter 4 Micro-machined piezoelectric diaphragm based immunosensor array

stress from the silicon oxidation process. Secondly, a thin PZT film ($\sim 0.75 \mu\text{m}$) was deposited by the sol-gel deposition technique. In the third step, the PZT film was wet etched in the specific areas to open the access to the bottom electrode pad.

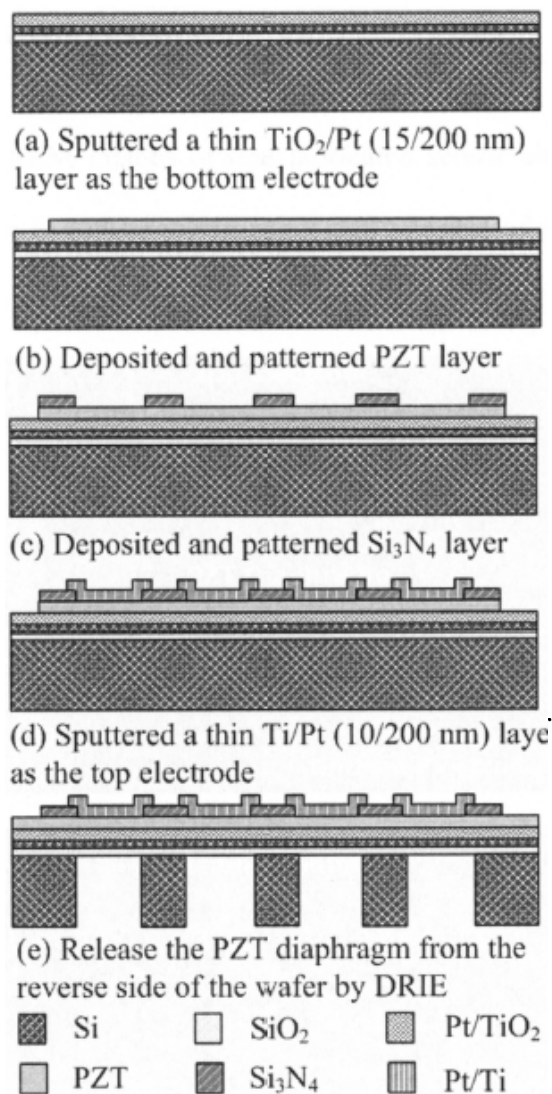


Figure 4.8. Schematic fabrication process for the circular piezoelectric sensor.

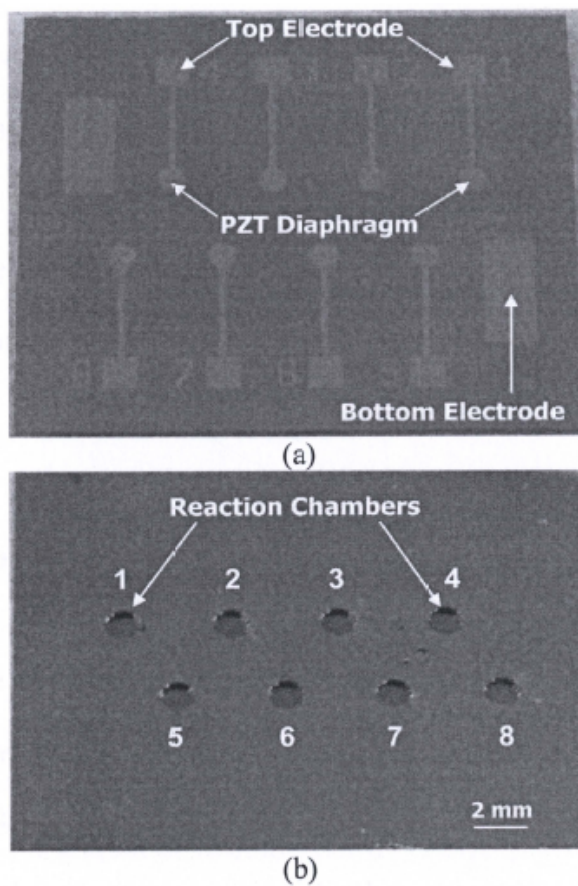
Afterwards, a Si_3N_4 layer (350 nm) was deposited to serve as an insulation layer. The Ti/Pt top electrode (10/200 nm) was patterned and deposited by sputtering.

Chapter 4 Micro-machined piezoelectric diaphragm based immunosensor array

Finally, the backside circular holes were etched by deep reactive ion etching (DRIE).

4.3.2 Fabrication results

The optical and SEM images of one fabricated sensor chip are presented in *Figure 4.9*. As shown in *Figure 4.9* (a), this chip consists of 8 individual sensors which are located in two parallel rows with numberings.



Chapter 4 Micro-machined piezoelectric diaphragm based immunosensor array

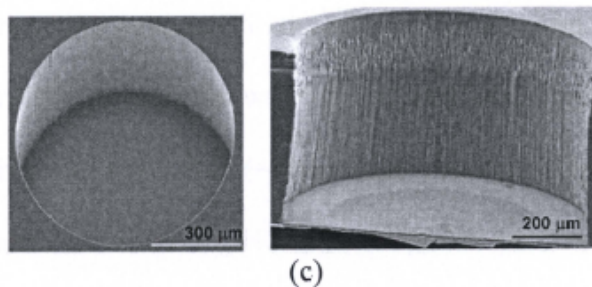


Figure 4.9. Optical images of a fabricated sensor array. (a) Front view. (b) Backside view. (c) Enlarged view (left) and cross sectional view (right) of the reaction chamber.

The individual sensor has a sandwich structure including a circular top electrode, a PZT diaphragm and a bottom electrode. The opposite side of the sensor array is shown in Figure 4.9 (b), where the 8 DRIE etched holes (ϕ 600 μm) serve as the reaction chambers during the bio-immobilization. The pictures in Figure 4.9 (c) left and right are the enlarged SEM image and cross sectional view of one reaction chamber. Because the dry etching technique is implemented to release the hole in the reverse side of the wafer, the yield of the fabricated sensor array is as high as 95.2%.

4.3.3 Immobilization of antigens

To realize the multi-detecting capability of the developed piezoelectric sensor array, three different antigens, HBsAg, HBcAg and α -Fetoprotein (AFP), which are purchased from Sigma (US Biological), were used as the probe molecules. The main immobilization processes, except the last one, are exactly the same as described in Figure 4.3 and the main chemical materials, such as PBS and TBS

Chapter 4 Micro-machined piezoelectric diaphragm based immunosensor array

washing buffer, are of the same condition and supplier with that in section 4.2.3-(i). All the other chemical reagents used were of analytical reagent grade.

After depositing the gold film (~10 nm) in the first step, antigens such as HBsAg, HBcAg and AFP in PBS (pH7.4) were applied into the individual reaction chambers with the same concentration (100 µg/ml) in sensors 1 and 2, 5 and 6, 3 and 4, respectively. One pair of sensors was immobilized with the same biomaterial and concentration, to ensure the accuracy and repeatability of the measurements.

To investigate the effect of the washing processes and the non-specific biomaterial absorption on the resonant frequencies of the sensors; the unused one pair of sensors (7 and 8), without any biomaterial, was used as the reference. After 30 minutes of deposition at room temperature, the reaction chambers were carefully washed by TBS washing buffer and DI water followed by N₂ drying. In the third step, BlockerTM Casein in TBS (1 mg/µl) was added to block the open space around the immobilized proteins. The excess blockers were washed away by TBS and DI water. To evaluate the specificity and selectivity of the immunochip, in the last step, a mixed solution containing anti-AFP (10 µg/ml) and anti-HBsAg (10 µg/ml) (Sigma, US Biological, USA) was added into all the reaction chambers in the sensor array for the hybridization between the antigens and antibodies. This step is similar to the practical clinic or laboratory diagonal process, where the solution to be tested generally contains more than one analyte. This inter-reaction process took about 45 min and the un-bonded or excess antibodies were again washed away by TBS and DI water, and then followed by N₂ air flow drying. The resonant frequencies of the sensors were measurement immediately after each immobilization process.

4.3.4 Characterization

(i) Characterization by fluorescence images

The sensing mechanism for the piezoelectric immunosensor is based on the mass change due to the Ag-Ab hybridization, hence, it is a label-free detection technique and it is also one of the advantages over other types of immunosensors. However, in order to investigate the specificity of the immunochip, Fluorescein Isothiocyanate (FITC) labeled rabbit anti-human HBsAg antibody and Cy-3 labeled anti-AFP (Sigma, USA) were used in the last step. The fluorescent image of the captured antigens could be observed using fluorescence microscopy (Perkin Elmer, Proxpress 2D proteomic imaging system), and the fluorescent effect was only observed in sensors 1 to 4 as shown in *Figure 4.10*, indicating that sensors 1 and 2, 3 and 4 had successfully captured anti-HBsAg and anti-AFP, respectively.

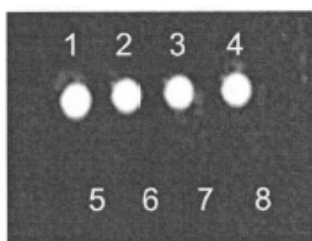


Figure 4.10. Fluorescent image of the reverse side of the sensor array after capturing the specific antibodies. Sensors 1 & 2, 3 & 4 successfully detected anti-HBsAg and anti-AFP.

The other four sensors (sensors 5 & 6 were immobilized with HBcAg and sensors 7 & 8 were used as references) in the second row remained in black color,

Chapter 4 Micro-machined piezoelectric diaphragm based immunosensor array

implying that no antibodies were captured by these four sensors. These results confirm the specific detection of anti-HBsAg and anti-AFP by this immunochip.

(ii) Resonant frequency of the sensor array

The resonant frequencies of the sensors were again measured by an impedance analyzer (Agilent 4294) after each immobilization process. *Figure 4.11* shows the resonant frequency spectrum of sensor 2 at each process. The figure shows that the frequency was continuously shifted to the lower domain, which implies an accumulated mass increasing after each immobilization or hybridization process. As the same phenomena observed in *Figure 4.6*, the amplitude of the frequency peak also decreased as more biomaterials were added. Sensors 3 and 4 for detecting anti-AFP also have a similar frequency spectrum after completing all the processes.

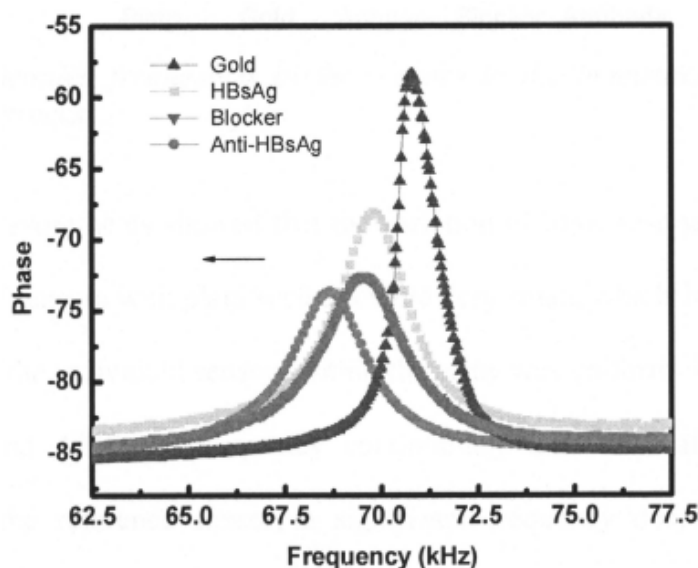


Figure 4.11. Frequency spectrum of sensor 2. The frequency continues shift to low frequency domain.

Chapter 4 Micro-machined piezoelectric diaphragm based immunosensor array

For the convenience of record, the original frequency of a sensor was noted as f_1 , and frequencies after depositing gold film, adding antigens, blockers and antibodies were recorded as f_2 , f_3 , f_4 , f_5 , respectively. Detailed frequency changes after each immobilization process for the sensor array is presented in Figure 4.12. The data shown in the figure were calculated based on the average frequency values of one pair of sensors after 3 measurements.

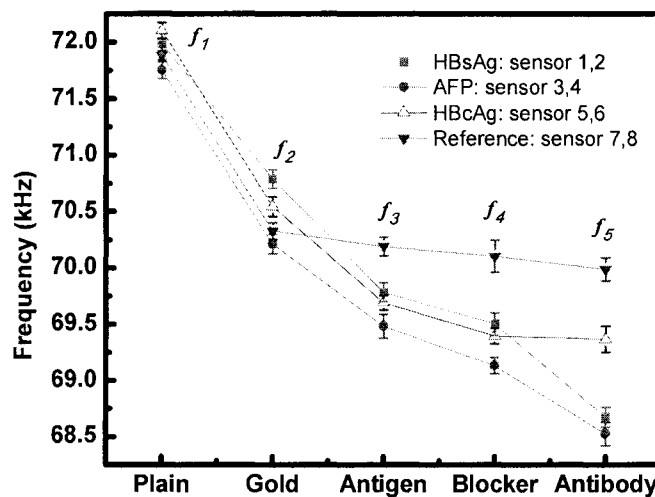


Figure 4.12. Detailed frequencies of the sensors in the immunochip after each immobilization process.

The first measurements showed that the variation of basic resonant frequencies of the 4 pairs of sensors with plain surfaces were very small, which indicate that the performance of the individual sensors within the array was uniform. For the sensors with HBsAg and AFP, the frequency continuously decreased after each step. However, for the reference sensor, a significant frequency decrease was only observed after the gold deposition. As there were no biomaterials fixed on the sensing surfaces in the subsequent process, the slight frequency decrease might be caused by the external contaminants during the washing processes. Comparing the

Chapter 4 Micro-machined piezoelectric diaphragm based immunosensor array

frequency depression values for the sensors with HBsAg and AFP, $\Delta f_{12}=f_1-f_2$ is the largest, which means that the deposited gold mass is the highest due to the high density of gold, and $\Delta f_{34}=f_3-f_4$ is the smallest, which implies that most of the spaces were occupied by the antigens in the second step and only a small amount of blockers were captured. This is also the reason why the slope of the curve at this step shown in Figure 4.12 is the smallest as well.

Although the concentration and volume of the immobilized probe proteins, such as HBsAg, AFP and HBcAg, were the same in the second step, the depressions of the frequency (Δf_{23}) in the second measurement have some variations. This implied that the amount of proteins successfully fixed onto the individual sensor surface was different due to the different physical properties of the proteins, such as density and mobility.

In the last process, because the applied mixed solution only contains anti-HBsAg and anti-AFP, the results presented in Figure 4.12 showed significant resonant frequency depression in the sensors with HBsAg and AFP. The frequency change in the sensors with HBcAg was negligible as no anti-HBcAg was contained in the added analyte solution. These results indicated that the frequency depression of the biosensors with HBsAg and AFP in the last step were mainly due to the mass of the captured antibodies by the antigens. It also demonstrated that the immunochip has a very good specificity. The very small frequency variations of the reference sensors during the whole immobilization processes showed that the washing processes and the non-specific biomaterials absorption had negligible affect on the sensor resonant frequency.

Chapter 4 Micro-machined piezoelectric diaphragm based immunosensor array

A typical single HBV diagnosis through polymer chain reaction (PCR) normally takes 9 to 12 hr or even longer time [105]. However, as discussed above, the total experiment time for detecting of HBsAg and AFP via this immunochip was less than 2 hr, which is much shorter than the reported time. The current immunochip consists of 8 individual sensors. Even if one pair of sensors is used to detect the same analyte, it is still 4 times faster than the single immunosensor.

(iii) Biosensor calibration

In order to investigate the detecting range and the detection limit of the developed immunochip, another two sensor chips with similar original resonant frequency were used to detect anti-HBsAg and anti-AFP, respectively.

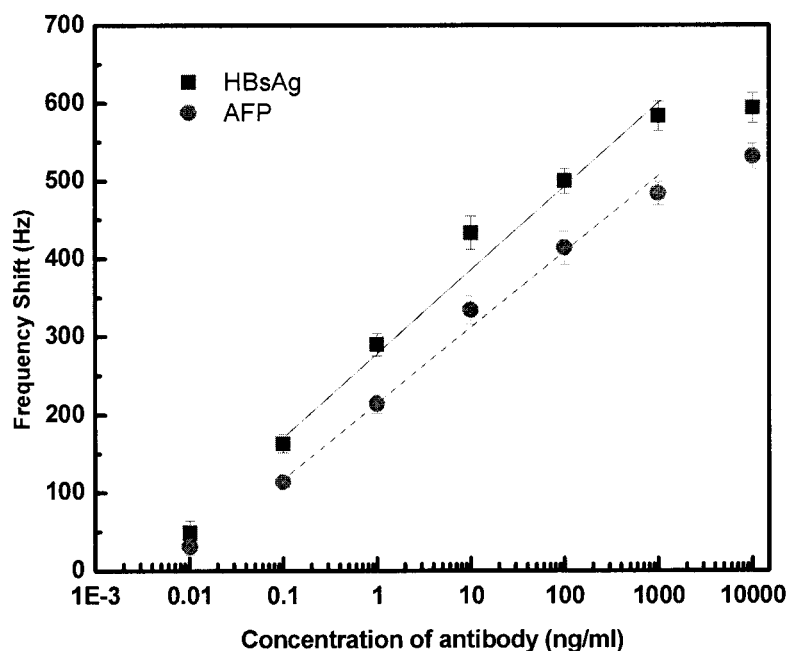


Figure 4.13. Calibration curve for detecting of HBsAg and AFP with two similar immunochips.

Chapter 4 Micro-machined piezoelectric diaphragm based immunosensor array

The immobilization processes were the same as described in section 4.3.3 except that in the second step, HBsAg and AFP were added into the 8 sensors in each chip with the same concentration, and in the last step anti-HBsAg and anti-AFP were applied into the individual reactions chambers in each sensor with the concentration of 0, 0.01, 0.1, 1, 10, 100, 1000, 10000 ng/ml, respectively.

The calibration curves for the frequency shifts versus concentration of HBsAg and AFP were shown in Figure 4.13. The frequency shifts plotted in the figure were obtained from the average values of 3 measurements at each concentration point and the error bars are the standard deviation of 3 replicates. There were very small frequency variation at a concentration fall in the range from 0 to 0.001 ng/ml; however, the curves were nearly linear from 0.1 to 1000 ng/ml for both of HBsAg and AFP with a determination limit of 0.1 ng/ml, which is 200 times lower than that of QCM [108]. It can be observed from the curves that when the concentrations of HBsAg and AFP were higher than 10 μ g/ml, the frequencies shift tended to be saturated due to the binding sites in the antigens being fully occupied by the antibodies. This reveals that the developed immuochips can have real determination for HBsAg and AFP in the range of 0.1 - 10000 ng/ml. The HBsAg shows a higher frequency shift than the AFP due to the different physical properties of the proteins and the immobilization procedures.

Based on all the material properties listed in Table 4.1 and the actual thickness, the gravimetric sensitivity (S_M) for the sensor array was calculated to be -45.33 m^2/kg by using Eq. 3.40. By knowing the S_M , A and f_0 , it is easy to find the S_m for detection of HBsAg and AFP to be 11.15 Hz/ng and 11.08 Hz/ng by Eq. 3.42. The slight variation between the two sensitivities may be attributed to the different

Chapter 4 Micro-machined piezoelectric diaphragm based immunosensor array

chemical and physical properties of HBsAg and AFT. Both S_M and S_m are more than 2 times and 1.5 times higher than that obtained from the square sensor array (S_M : - 16.5 m²/kg, S_m : 6.25 Hz/ng) in the previous section. These improved results are expected and can be explained by the following. Firstly, the total thickness (3.7 μm) and average density of the multi-layered sensing diaphragm in the circular sensor are much thinner and lower than that in the square sensor (6.3 μm thick). According to the Eq. 3.41 in Chapter 3, a thin diaphragm with low density (circular) will have a higher S_M . Secondly; the sensing area (ϕ 600 μm) is smaller than that in the square sensor. Lastly, the working frequency of circular sensors is higher than that of the square one. This may possibly due to the residual stress that was accumulated from the fabrication process. The stress has a minor impact on the resonance in the square sensor as the actuating PZT is thick. However, the stress may increase the resonant frequency for a thin PZT diaphragm based circular sensor, which can be revealed by Eq.3.3. In conclusion, the circular sensors have higher S_M , smaller sensing area and higher working frequency, hence, the S_m is found to be higher than that of the square sensors.

4.4 Summary of this chapter

In this work, two types of micro-fabricated piezoelectric immunochip were developed. The first square piezoelectric diaphragm biosensor array was demonstrated to rapidly detect model targets of anti-goat IgGs with sensitivity of 6.25 Hz/ng. As an improved device, the second circular piezoelectric sensor array was shown to be able to simultaneously detect HBsAg, AFP and HBcAg, A clear

Chapter 4 Micro-machined piezoelectric diaphragm based immunosensor array

frequency depression was observed and the frequency depression among the sensor array varied from 600 to 800 Hz. The immunochip can provide a real determination of HBsAg and AFP with the limit of detection of 0.1 ng/ml in the concentration range of 0.1 to 10000 ng/ml. The sensitivity for detection of HBsAg and AFP was found to be 11.15 Hz/ng and 11.08 Hz/ng, respectively. The sensitivity of mass per unit area is $-45.33 \text{ m}^2/\text{kg}$. For the demonstration in this work, the diameters of the reaction chambers and the overall size of the chip were designed to be relatively large. With the micro-machining technology and further process optimization, their sizes can be further miniaturized and hundreds of chips can be produced in one 4" wafer with very low cost. Moreover, due to the non-covalent bonding between the antigens and the gold film, it is easy to remove the antigen-antibody complex from the gold surface by certain acid treatment and ultrasonic cleaning [106-108]. Therefore, the chip can be reused and the cost can be further decreased. The preliminary results demonstrate that with further calibration and optimization, the developed piezoelectric immunochip has the potential of being used as a disposable biochip for rapid and low cost medical diagnosis.

Chapter 5

Synthesis of carbon nanotubes by thermal chemical vapor deposition

This chapter presents a systematic study on the influences of various synthesis parameters such as pretreatment time, growth temperature, growth time, gas flow rate, and gas pressure on the density, length and purity of carbon nanotube (CNT) growth by thermal chemical vapor deposition (TCVD). Vertically-aligned CNTs grown on Fe catalyst deposited silicon oxide substrates were characterized by scanning electron microscopy (SEM), Raman spectroscopy and transmission electron microscopy (TEM). It was found that both the length and quality of the CNT were affected by the synthesis parameters studied. After studying and optimizing CNT growth with respect to the various TCVD synthesis parameters, long CNT arrays up to 380 μm in length were successfully synthesized. The influence of individual parameter will be discussed in the following sections.

5.1 Introduction

In the past two decades, intensive research interests have been paid to the CNT due to its excellent mechanical, electrical, thermal and bio-chemical properties [8-10]. These remarkable properties have led to a wide range of potential applications including nanoelectronics, quantum wire interconnects, chemical and biological sensors, ceramic or metal composites, and field emission devices [11, 12].

Chapter 5 Synthesis of carbon nanotubes by thermal chemical vapor deposition

In this project, CNTs will be integrated with piezoelectric mass sensor for biosensing application, the density, length and purity of the CNT can directly affect the sensor sensitivity, dynamic range and reproducibility. Therefore, it is vitally important to optimize the synthesis parameters to achieve the best results. CNTs will be synthesized through TCVD because of its simple equipment set-up and capability in scale-up productions [8, 9].

Although it has been widely reported that control of the length, density, and quality of the CNT can be achieved by varying the synthesis parameters such as catalyst thickness, catalyst pretreatment time, growth time, reaction gas flow rate, growth temperature and pressure [13, 14, 109-112], most of the researchers just partially reported the parameter influence on the CNTs and no comprehensive studies are available till date. In addition the dependence of CNT morphology on the synthesis parameters is not very clear and precise control on the growth is not achieved yet. Therefore, a systematic study of the influences of various CVD synthesis parameters on both the length and quality of CNT arrays grown by TCVD is implemented in this project.

5.2 Experimental details

In this experiment, four main steps were involved to synthesis CNTs on Si substrate. As illustrated in Figure 5.1, in the first step, a 4" wafer was cleaned in a mixed solution of H_2SO_4 and H_2O_2 at temperature of 120 °C, secondly, a 2 μ m thick layer of SiO_2 was deposited on the substrate via thermal oxidation. This thin

Chapter 5 Synthesis of carbon nanotubes by thermal chemical vapor deposition

oxidation layer serves as the buffer layer to prevent the catalyst diffusing into the Si substrate. A thin layer of Fe catalyst (2-10 nm) was then deposited on the SiO₂ layer by E-beam evaporation. Finally, the wafer with the catalyst film was cut into small samples (5 cm × 5 cm) and loaded with a face-up direction onto a titanium boat in the center of 4-inch barrel quartz tube.

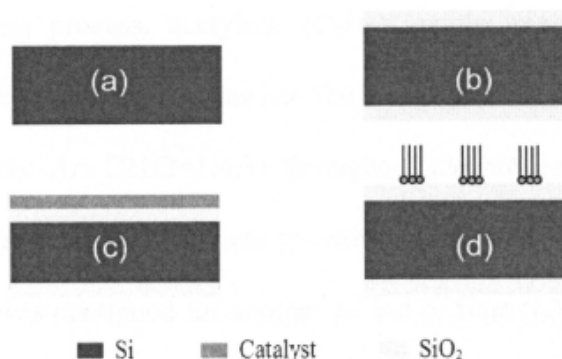


Figure 5.1. Sketch of synthesis of CNT through TCVD, (a) wafer preparation, (b) SiO₂ film deposition, (c) deposition of Fe catalysis by E-beam evaporation, (d) CNT growth by TCVD.

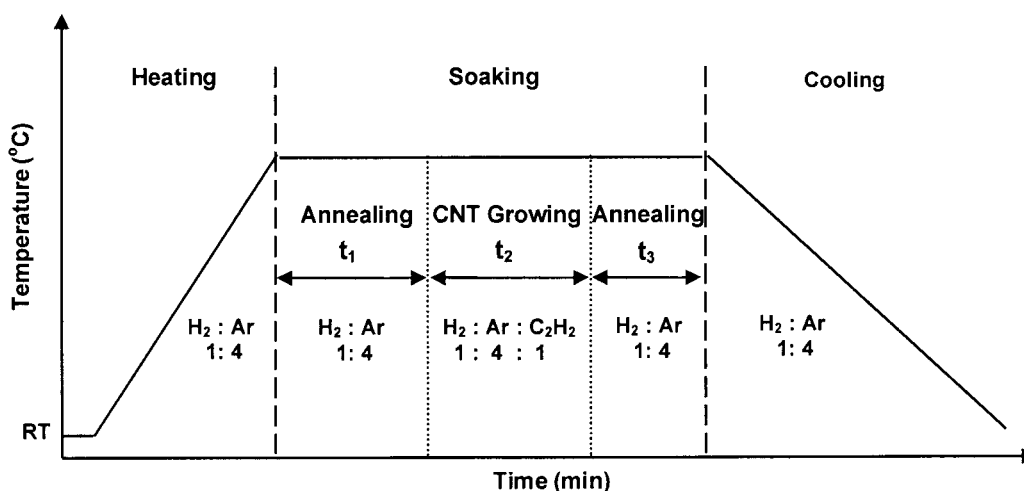


Figure 5.2. Sketch of CNT growing process.

Figure 5.2 summarized the details of the CNT synthesis process by TCVD system. Three main stages, heating, soaking and cooling, were involved in the

Chapter 5 Synthesis of carbon nanotubes by thermal chemical vapor deposition

completed CNT growing process. In the first stage, hydrogen (H_2) and argon (Ar) are released into the quartz tube as process gases, and then the heater was turned on. When the desired growth temperature was reached, the substrate was kept at that temperature for a catalyst pretreatment time (t_1) where the continuous thin Fe catalyst film would be cracked into nano-particles that enable the CNT growth. After this annealing process, acetylene (C_2H_2), as the reaction gas, was then introduced into the quartz tube to initiate the CNT growth. The flow rate of the gases was fixed (H_2 : Ar: $C_2H_2=1:4:1$) throughout the process. The overall CNT growing time was set to be t_2 . After the growth process, C_2H_2 supply was switched off and annealing was continued for another period of time (t_3) before the substrate was cooled down to below 200 °C under the flow of Ar and H_2 gas.

Table 5 1. Synthesis parameters for the experiment series.

Experiment	Pretreatment time t_1 (min)	Temperature (°C)	Growth time t_2 (min)	Flow rate (sccm)	Pressure (Torr)
1	5 - 45	700	45	25	12
2		650 - 900	30	25	12
3			5 - 80	25	12
4				25 - 100	12
5					4 - 20

The effect of process parameter such as the type of catalytic layer, thickness of catalytic layer, pre-treatment time, growth temperature, growth time, gas flow rate and pressure will be discussed in the following sections. Five main experiments

Chapter 5 Synthesis of carbon nanotubes by thermal chemical vapor deposition

were implemented and the variables are highlighted in bold in each experiment listed in Table 5.1. In each experiment, only one parameter was varied, the best value for the variable parameter was confirmed after the characterization, and it was used in the next experiment. All the unknown parameters as shown in blank in the above table were confirmed after 5 rounds of experiments.

5.2.1 The influence of catalyst thickness and annealing time on CNT growth

In the application of direct growth CNT on the piezoelectric diaphragm that will be discussed in Chapter 6, only the tips of the CNTs will be treated and used for bio-sensing; therefore CNTs need to be synthesized with high density. As such, factors affecting CNT densities will be investigated in this section. It is reported that the CNT density is mainly affected by catalyst type, catalyst thickness, catalyst annealing time and CNT growing temperature. The most commonly used catalysts are iron (Fe), cobalt (Co) and nickel (Ni). Fe is selected in this project because CNT grown based on Fe catalyst has the highest density and best quality at any temperature and is the most efficient catalyst among the others [112, 113].

Although a strong correlation between the CNT diameter/density and the nanoparticle size is widely reported for plasma-enhanced CVD [111, 114, 115], it is not true for thermal CVD. In order to investigate the effect of catalyst on CNT growth, the prepared substrate with deposited Fe catalyst layer undergoes annealing in vacuum (mixture of Ar and H₂) with varying thickness, annealing time (t_1), and

Chapter 5 Synthesis of carbon nanotubes by thermal chemical vapor deposition

temperature without subsequent introduction of C_2H_2 gas to simulate the condition of the catalyst layer prior to CNT growth.

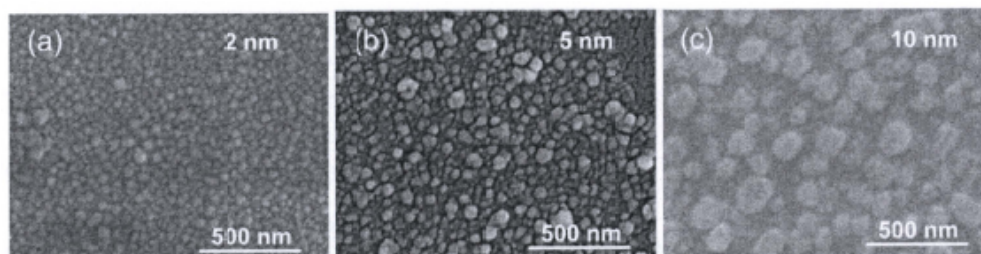


Figure 5.3. Morphology of the catalyst layer after annealing for 15 min with different thickness and temperatures. (a)-(c) shows the pictures of the catalyst film with thickness of 2, 5 and 10 nm at temperature of 700 °C.

In the first experiment, three samples with catalyst layer of 2, 5 and 10 nm were heated at 700 °C for 15 min in vacuum and the morphology of the catalyst layer is shown in Figure 5.3 (a)-(c). It is clearly shown that the diameters of the catalyst particles increase according to the catalyst thickness increase. In addition, the density of the catalyst particles also increases as the thickness increase. Due to the high surface tension, the thin film was easily broken into nano particles during the annealing process. In contrast, under the same conditions, it is difficult for the thick film to break into the small particles due to the low tension, and they eventually break into large particles. As reported by others, the more noticeable trend is to increase in CNT density with increasing catalyst particle density [114, 115]. In conclusion, it is necessary to deposit the catalyst with the thickness of 2 nm to produce high density CNTs in this project.

After optimizing the thickness of the catalyst layer, the second experiment was conducted to study the annealing time (t_2) effect. The aim of the experiment is to determine how this pretreatment time t_1 , with the temperature kept constant at

Chapter 5 Synthesis of carbon nanotubes by thermal chemical vapor deposition

700 °C, will affect the size and distribution of the catalyst particles and the density of CNT growth.

Figure 5.4 shows the top view SEM and 3D AFM images of the catalyst layer on the substrate surface after undergoing annealing pretreatment under H₂ gas flow at 700 °C for various period of time. The AFM images are comparable to the SEM images and the size of the Fe particles increased with pretreatment time t_1 . Before annealing, the substrate surface (*Figure 5.4 a*) appeared to be very smooth and the grain boundaries were not obvious. After treatment for 5 min at 700 °C, the grain boundaries were more noticeable (*Figure 5.4 b*). As the treatment time was increased to 10 min, both the SEM and AFM images showed more uneven surfaces and signs of agglomeration (in *Figure 5.4 c*). The agglomeration became more observable after treatment for 15 min (*Figure 5.4 d*) and the grainy features appeared to be larger after 20 min of treatment (*Figure 5.4 e*).

Chapter 5 Synthesis of carbon nanotubes by thermal chemical vapor deposition

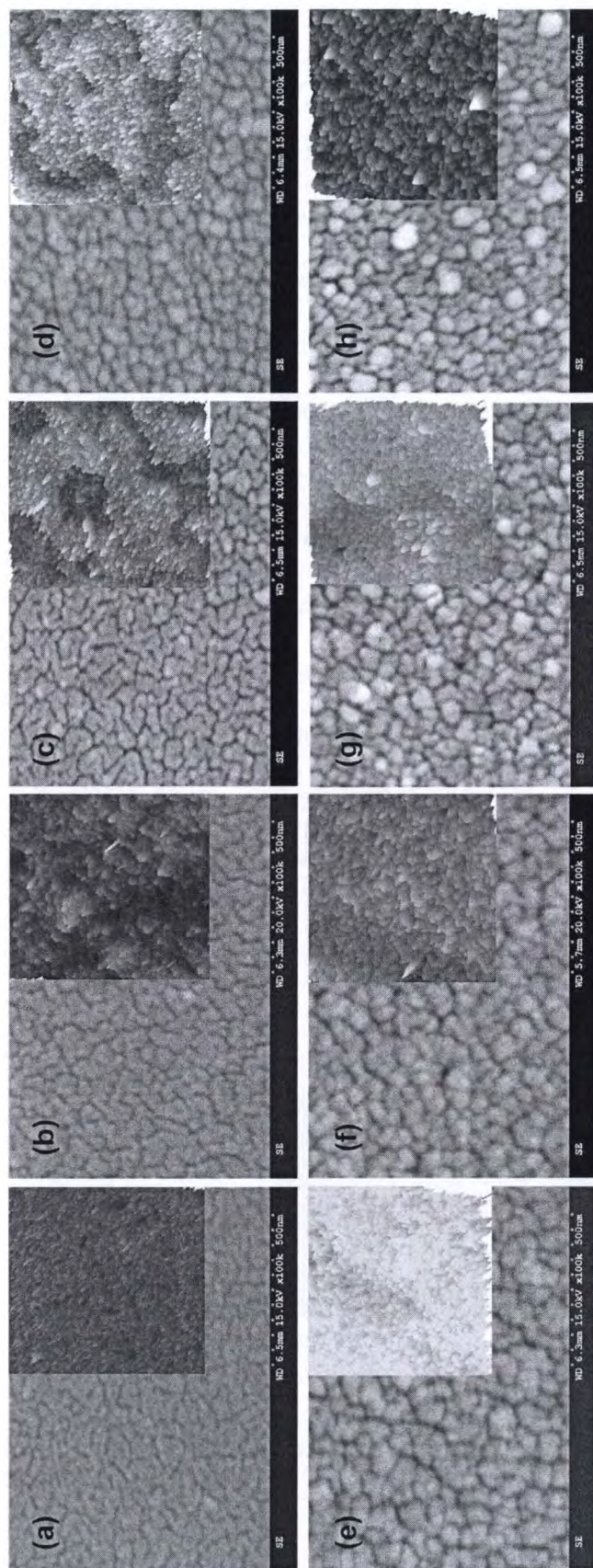


Figure 5.4. SEM images and 3D AFM images (the inserted images) of the catalyst surface after annealing at 700 °C for (a) 0 min, (b) 5 min, (c) 10 min, (d) 15 min, (e) 20 min, (f) 25 min, (g) 30 min and (h) 45 min.

Chapter 5 Synthesis of carbon nanotubes by thermal chemical vapor deposition

As the treatment time increased, catalyst islands started to appear on the substrate surface. The substrate surface after 10 min and 15min of annealing seemed to have smaller particles with a denser distribution, compared to the substrate surface, after more than 20 min of annealing treatment. The difference in appearance for the catalyst surface treated for 20, 25 and 30 min became less distinguishable but several distinct bright particles (Figure 5.1 g-h) started to appear and large particles became more observable when the treatment time was increased to 45 min. This effect is probably due to the increasing coalescence of neighboring Fe catalyst particles as the substrate is treated under longer periods of high temperature at 700 °C and nanoparticles tend to agglomerate to reduce surface energy [110,116,117]. The gradual increase in treatment time did not show very significant changes in the surface morphology.

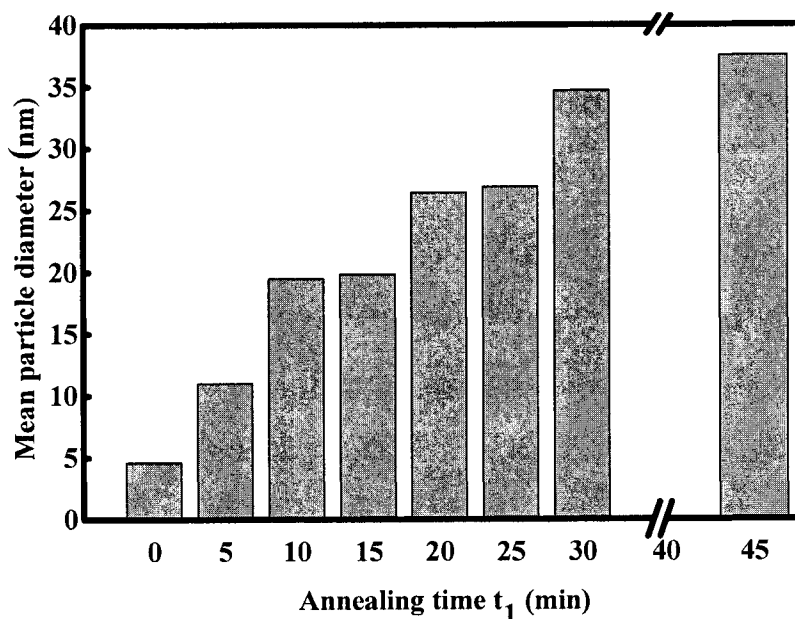


Figure 5.5. Mean diameter of catalyst particle on substrate surface as a function of annealing pretreatment time t_1 .

Chapter 5 Synthesis of carbon nanotubes by thermal chemical vapor deposition

The corresponding mean particle diameter measured by the AFM is shown in Figure 5.5. It is observed that the size of the Fe particles increased with pretreatment time t_1 . Before the annealing process, the size of the mean particle size was less than 5 nm, which was probably attributed to the diameter of the deposited Fe atom. After 5 min of annealing, the substrate surface still appeared to be smooth and the particle size increased to around 11 nm. The particle size increased to around 20 nm after treating for 10 min and there was a slight difference between the 10 and 15 min treatment. Similarly, there was no significant particle size increase between the 20 and 25 min treatment. This result implied that the catalyst particles were unable to accumulate sufficient energy to increase its size during such a small treatment time variation. One interesting phenomena was observed after the catalyst was treated for 30 min. Unlike those found before, there was a significant size change even though the treatment time was increased by 5 min. It can be explained by the fact that the nano particles accumulate enough energy after treatment for 25 min and there was an energy jump or increase in coalescence of neighboring Fe catalyst particles [118]. As further treatment time increased to 45 min, no notable change occurred because the fissure was so wide that catalyst particles were unable to agglomerate further.

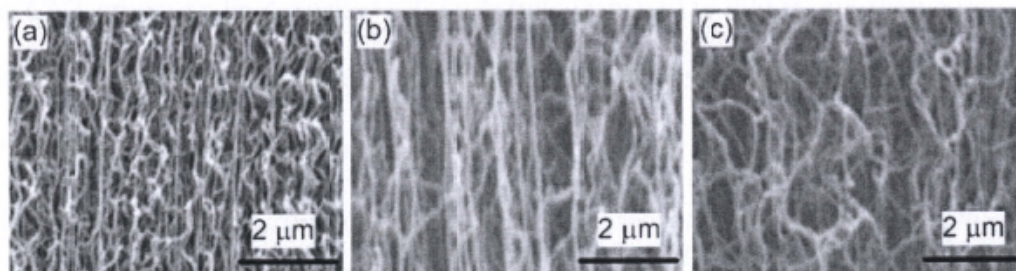


Figure 5.6. High magnification SEM images shows the CNT density grew with different catalyst pretreatment time (a) 10 min, (b) 20 min and (c) 30 min.

Chapter 5 Synthesis of carbon nanotubes by thermal chemical vapor deposition

Due to the variation of catalyst particle size and distribution on the substrate, the densities of CNT growth after TCVD are also different. Figure 5.6 shows the CNT grown with the same parameters list in Table 5.1, except the annealing time. The density decreases with the increase in treating time, which is attributed to the catalyst size at different annealing time. It is obvious that the CNTs have the highest density at the annealing time of 10 min due to the finest catalyst particle size formation. In fact the grown CNTs with treatment time of 30 and 45 min were in disorder and not vertically-aligned. This was mainly because the catalyst particle size was either too small or too large. As a conclusion, in order to obtain the high density vertically-aligned CNTs, the best treating time to be selected is 10 min.

5.2.2 The influence of temperature on CNT growth

In the second experiment, CNT growth was investigated as a function of the TCVD temperature in the range of 650 °C to 900 °C. The pre-treatment time (t_1) was set to be 10 min, which was the optimized value from the first experiment and the parameters were the same as listed in Table 5.1. Cross-sectional SEM images for the CNT grown on Fe-deposited SiO₂ substrate from 650 to 900 °C are shown in Figure 5.7. Uniform CNTs were grown and the length increased from 95 μm at 650 °C (Figure 5.7 a) to 168 μm at 700 °C (Figure 5.7 b). When the temperature was increased to 725 °C, the length of CNT increased dramatically to 288 μm (Figure 5.7 c) but started to decrease to 157 μm at 750 °C (Figure 5.7 d). The length of CNT continues to drop drastically to 35 μm at 800 °C

Chapter 5 Synthesis of carbon nanotubes by thermal chemical vapor deposition

(Figure 5.7 e) and remained relatively constant at 34 μm (Figure 5.7 f) and 35 μm (Figure 5.7 g) for the temperature of 850 $^{\circ}\text{C}$ and 900 $^{\circ}\text{C}$ respectively. It can be observed that CNT length is very temperature dependent, as a slight change in temperature (e.g. from 700 to 725 $^{\circ}\text{C}$ or from 725 to 750 $^{\circ}\text{C}$) can increase or decrease the CNT length by about 100 μm .

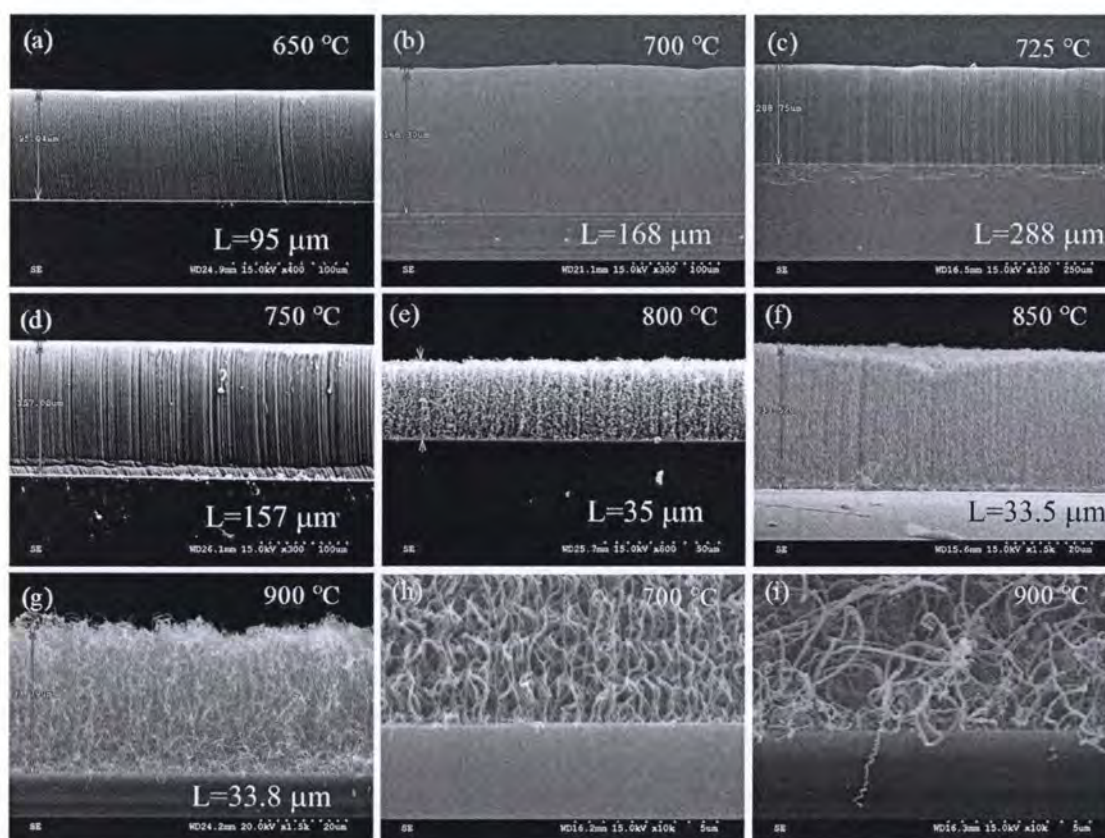


Figure 5.7. Cross section SEM images of CNT at different growth temperatures, (a)-(h) are 650, 700, 725, 750, 800, 850 and 900 $^{\circ}\text{C}$, respectively. The last two image (h-i) are the enlarged view of CNT growth at temperature of 700 and 900 $^{\circ}\text{C}$.

Another noticeable trend is the drop in CNT length at 800 $^{\circ}\text{C}$ corresponding to the decrease in the density of CNT. Vertically well-aligned CNT (as shown in Figure 5.7 (h)) were homogeneously grown at 650 $^{\circ}\text{C}$, 700 $^{\circ}\text{C}$, 725 $^{\circ}\text{C}$ and 750 $^{\circ}\text{C}$, compared to shorter and less well-aligned CNT grown at 800 $^{\circ}\text{C}$, 850 $^{\circ}\text{C}$ and

Chapter 5 Synthesis of carbon nanotubes by thermal chemical vapor deposition

900 °C. The CNT appeared to be less dense and curlier at the three higher temperatures. CNTs grown at 900 °C have the lowest density such that individual strands of randomly oriented CNT can be seen clearly (Figure 5.7 i). This can be explained with the crowding effect that determines the overall vertical CNT length [119]. The influence of temperature growth on morphology of the Fe catalyst particle density was investigated with conditions described in the previous section and the results have the similar trend with that shown in Figure 5.3. It was confirmed that higher temperatures encourage the formation of bigger Fe catalyst particles which are less uniformly distributed with much lower density [110, 120].

Although high temperature increased in the dissolution, diffusion and precipitation of carbon and resulted in higher CNT growth rate; this effect is seriously weighed down by the decrease in catalyst particle density. The low catalyst density allows more space for the CNT to grow laterally and in random directions as they suffer from a lack of crowding effect or mechanical leaning between neighboring CNT. As a result the overall vertical length is much shorter for higher temperatures. Conversely, the CNT synthesized at 700 °C formed from dense Fe catalyst particles are denser and more aligned. This is similar to what has been reported in several papers which investigated the effect of temperature on CNT growth [119, 121]. Based on the obtained results, it can be concluded that the best temperature for growing long CNTs with high density is 725 °C.

The Raman spectroscopy relies on the Raman scattering concept, whereby light scatters inelastically and it is a spectroscopic technique that is used to study vibration, rotational and other low frequency excitations of chemical bonds. In this

Chapter 5 Synthesis of carbon nanotubes by thermal chemical vapor deposition

project, a Renishaw Raman Microscope RM 1000 which utilizes a 633 nm HeNe laser source was used to characterize the functional groups immobilized on the surface of CNTs. Raman spectroscopy was performed on the CNT to evaluate the quality or purity of the grown CNT at different temperature. In general, G-band and D-band indicate the presence of crystalline graphitic carbon and defect carbon within CNTs. Hence, the peak intensity ratio of the G-band over the D-band is often regarded as a measure of the degree of graphitic ordering in the CNTs. Raman spectroscopy of the grown CNTs at temperatures from 650 °C to 900 °C is displayed in Figure 5.8. All the spectra have similar shape and two constant Raman bands at 1325 cm⁻¹ (D-band) and 1575 cm⁻¹ (G-band) were observed. In the spectrum of CNT grown at 650 °C, the D-band is stronger than the G-band, suggesting that there are more defective nano-carbon materials than graphitic carbon of CNT. As the growth temperatures increases, the G-bands become stronger and the relationship between intensity ratio (I_G/I_D) and temperature is shown in Figure 5.9. It is clear that the intensity ratio increases as the temperature increase, reaching a maximum value of 850 °C. This result suggests that CNTs with highly-ordered graphitic tubular structures were grown at high temperature. Raman characterization has demonstrated that the crystallinity of graphitic CNT improves with increasing the CNT growing temperature, which is also reported in some other papers [111, 119, 121, 122]. Another phenomenon observed is that at the temperature of 900 °C, the intensity ratio decreases. At such high temperature, the reaction rate is so fast that the dissolution, diffusion and precipitation of carbon can not be completed smoothly, which results in certain amount of carbon defects.

Chapter 5 Synthesis of carbon nanotubes by thermal chemical vapor deposition

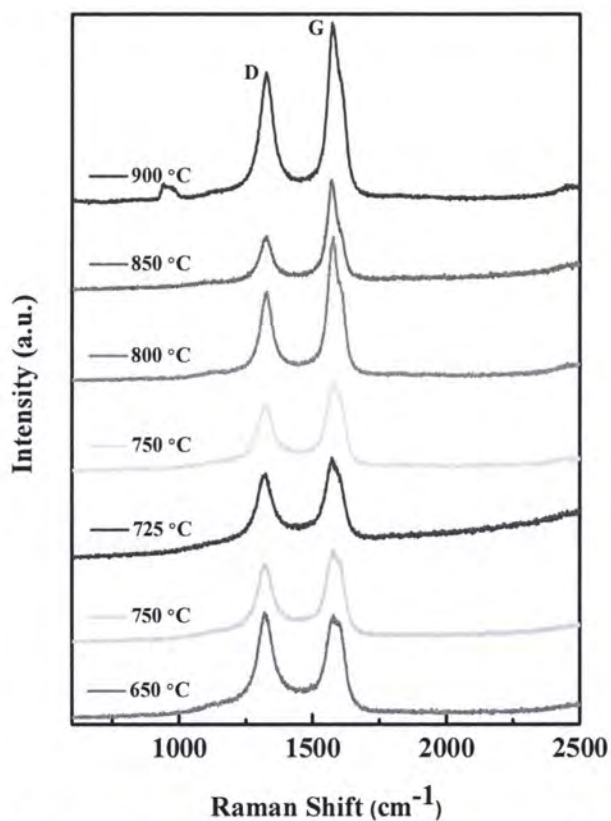


Figure 5.8. Raman Spectrum of CNT for different growth temperatures.

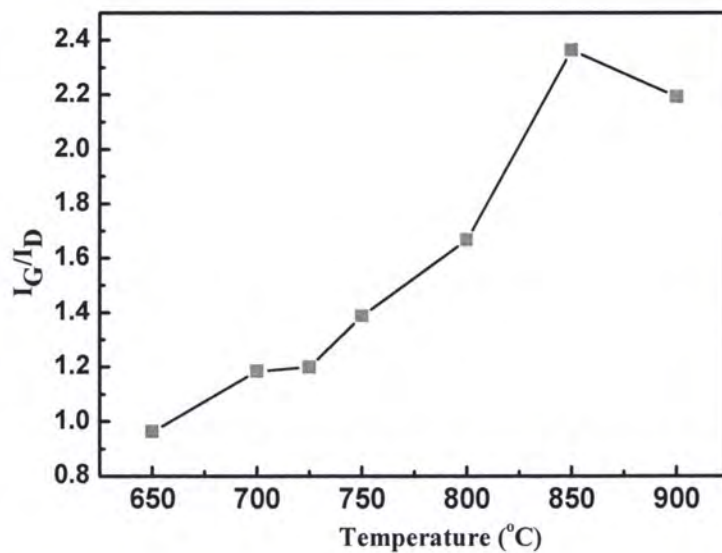


Figure 5.9. Peak intensity ratio I_G/I_D as a function of growth temperatures.

Chapter 5 Synthesis of carbon nanotubes by thermal chemical vapor deposition

The results achieved from this experiment show that both the density and length of CNT growth by the TCVD system can be controlled by adjusting the growing temperature, more over, the structure and purity of CNT is also greatly affected by temperature. Although the high quality CNTs were achieved at 850 °C, the density and length are not suitable for the biosensing application. As such, the best temperature for synthesis vertically-aligned long CNT is around 725 °C.

5.2.3 The influence of growth time on CNT growth

In this experiment, the influence of growth time t_2 will be studied at a temperature of 725 °C. The length of CNT as a function of growth time t_2 ranging from 5 to 80 min is shown in Figure 5.10. The growth increased tremendously from 30 to 190 μm in the first 40 min, but eventually leveled off at about 200 μm for long growing durations. This phenomenon has also been observed in many thermal CVD processes [119, 123, 124].

Initially, the catalyst particles were fresh and active for the nucleation of CNT. As the growth time proceeded; this activity decreased gradually and the precipitation of CNT slowed down. The Fe catalyst particles could also have been turned into iron carbide or other non-catalytic form after prolonged growth duration [125]. So carbon atoms adsorbed onto the substrate surface formed amorphous carbon which gradually inhibited the diffusion of carbon and prevent further formation of CNT [126]. When the growth time was longer than 40min, most of the catalytic Fe nanoparticles were likely to be deactivated by amorphous carbon

Chapter 5 Synthesis of carbon nanotubes by thermal chemical vapor deposition

structures that covered on them. Therefore, further increase of the growth time t_2 was unable to sustain any additional CNT growth.

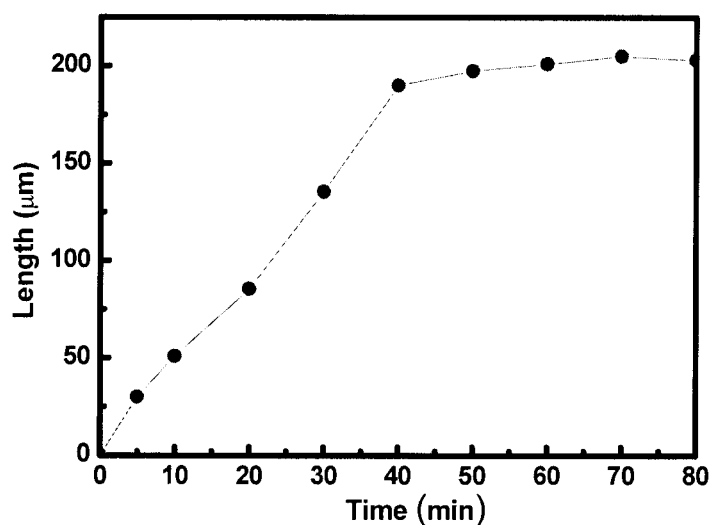


Figure 5.10. CNT length as a function of growth time at 725 °C.

The effect of growth time t_2 at 725 °C was also investigated with Raman spectroscopy. Figure 5.11 shows the relationship of the peak intensity ratio as a function of growth time t_2 . As the growth time increased from 5 min to 10min, the Raman I_G/I_D ratio increased and a maximum value of around 1.5 was reached. However, when growth time was further increased to 20 min, the Raman I_G/I_D ratio decreased and subsequently dropped to below 1 at the time of 80 min. The reason is the following: initially, increased the growth time increases the number of H_2 gas molecules to interact with the catalytic nanoparticles. Hence, the initial increase of Raman I_G/I_D ratio is attributed to the degree of graphitic ordering increasing in the grown CNT. However, when growth time extended beyond a certain point caused the defective carbon structures to form more rapidly than the ordered graphitic

Chapter 5 Synthesis of carbon nanotubes by thermal chemical vapor deposition

structures, resulting in the decrease in I_G/I_D ratio [127]. By increasing the growth time, the purity (I_G/I_D) of the CNT dropped. However, it can increase the CNT length. Therefore, there should be an optimum growth duration for each set of experimental parameters in which the CNTs grown are good quality with reasonable length and yield. This is especially important for the applications where vertically aligned CNT is necessary in this project. Hence, as a compromise, CNT will be synthesized with a growth time of 45 min in the subsequent experiments.

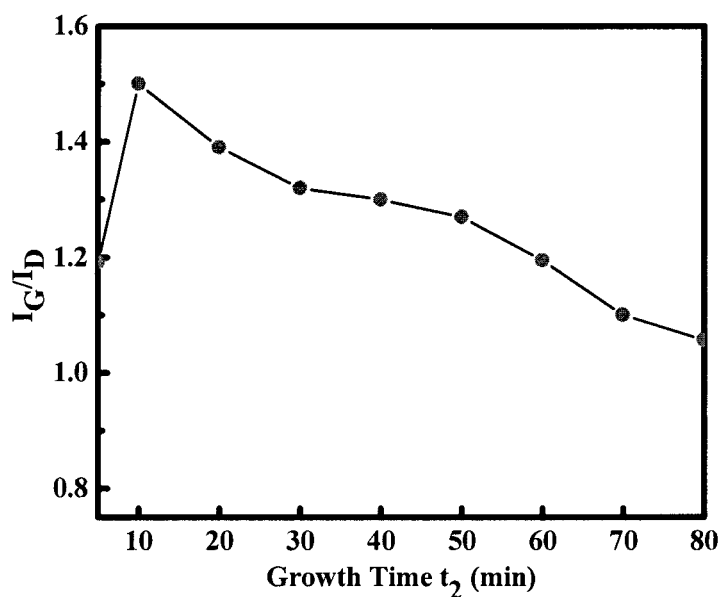


Figure 5.11. Peak Raman intensity ratio I_G/I_D as a function of growth time t_2 at 725 °C. The growth time varies from 5 to 80 min.

5.2.4 The influence of gas flow rate on CNT growth

The next set of experiment was implemented to investigate the influence of gas flow rate on the CNT growth at 725 °C for 45 min. In all the experiments, the ratio of H_2 to Ar to C_2H_2 gases was always fixed at 1:4:1. As C_2H_2 was the reaction

Chapter 5 Synthesis of carbon nanotubes by thermal chemical vapor deposition

gas, the flow rate of C_2H_2 was varied from 5 to 100 sccm. The length of CNT synthesized as a function of C_2H_2 flow rate at 725 °C is plotted in Figure 5.12. The CNT length increased with increasing C_2H_2 gas flow rate at lower flow rates of 5 to 25 sccm. The maximum CNT length of 260 μm synthesized was at 725 °C at C_2H_2 flow rate of 50 sccm. There was a slight decrease after the flow rate increased to 75 sccm. However, the CNT length decreases significantly at flow rate of 100 sccm.

The increase in C_2H_2 gas flow rate increased the supply of carbon to the catalytic Fe nanoparticles, which resulted in an increase in diffusion and precipitation of carbon into graphitic CNT structures. However, there was a competition between CNT growth and catalyst deactivation due to the formation of defective carbon structure. In the early stage of the process, the C_2H_2 flow rate was lower than the C_2H_2 consumption rate. Therefore, CNT length increased as the flow rate increased. At around 50 sccm, the C_2H_2 supply rate is almost in equilibrium with the C_2H_2 consumption rate led to dense CNTs with a maximum length of 260 μm . However, further increase in the C_2H_2 flow rate caused C_2H_2 supply rate to be faster than the C_2H_2 consumption rate. Carbon atoms were absorbed faster than they can be formed into CNT. As a result, the increased production of amorphous carbon that decomposes from excess supply of C_2H_2 deactivated the catalytic Fe nanoparticles faster and prevent CNTs from growing up to a longer length.

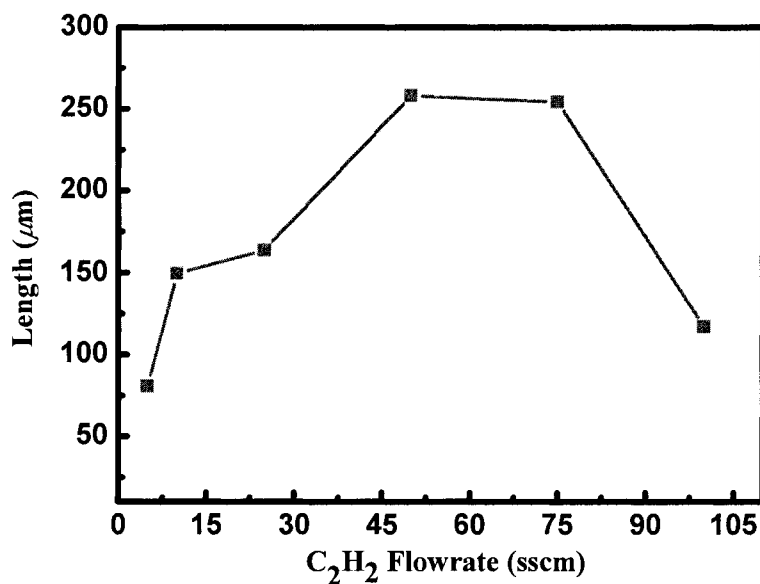
Chapter 5 Synthesis of carbon nanotubes by thermal chemical vapor deposition

Figure 5.12. CNT length as a function of C₂H₂ flow rate at 725 °C.

Therefore, increasing the C₂H₂ gas flow rate did not always increase the CNT length, but instead the CNT length decreased at higher flow rates of 100 sccm. Figure 5.13 shows the Raman intensity ratio I_G/I_D as a function of different C₂H₂ flow rate at 725 °C. There is a slight change when the C₂H₂ flow rate increases by less than 50 sccm, the I_G/I_D ratio reaches a maximum value of 1.25 around 5 sccm. However, as C₂H₂ flow rate increased beyond 50 sccm, there is a prominent intensity ratio drop. As explained in the previous part, the amount of defective structures such as amorphous carbon increased after the flow rate exceeds 50 sccm, which resulted in a stronger D-band. Therefore, Raman I_G/I_D ratio decreased or the quality of CNT decreased as flow rate increases.

Chapter 5 Synthesis of carbon nanotubes by thermal chemical vapor deposition

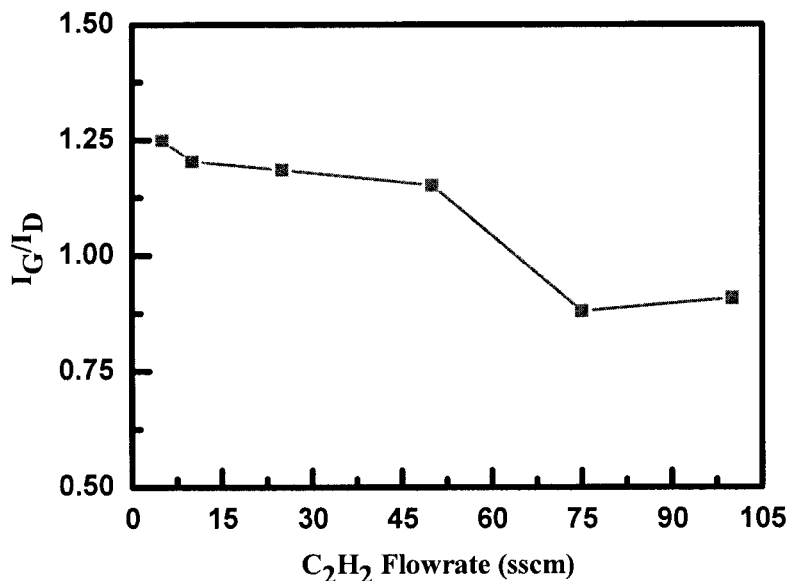


Figure 5.13. Raman intensity ratio (I_G/I_D) as a function of different C_2H_2 flow rate at 725 °C.

In this series of experiments, the CNT with the longest length of around 260 μm was synthesized at the temperature of 725 °C with a flow rate between 50 sccm to 75 sccm. However, the Raman I_G/I_D ratio started to drop when the flow rate was above 25 sccm. By considering both length and quality, it appears that growing CNT with C_2H_2 flow of 25 sccm at 725 °C is the optimum parameters. Hence, for the next series of experiments on investigating the influence of pressure, the flow rate of C_2H_2 will be fixed at 25 sccm.

5.2.5 The influence of pressure on CNT growth

The last series of experiments were conducted to investigate the influence of gas pressure. The pressure under study was the total gas pressure exerted by the

Chapter 5 Synthesis of carbon nanotubes by thermal chemical vapor deposition

C₂H₂ together with Ar and H₂ during growth time t_2 . Based on the results of previous experiments, considerable growth can be achieved at 725 °C with a C₂H₂ flow rate of 25sccm for 45 min (t_2) and 10 min of the catalyst pretreatment time t_1 . Therefore, this set of synthesis parameters was chosen and only growth pressure was varied from 4 to 20 Torr by controlling the vacuum pump valve.

Under these conditions, CNTs were homogenously synthesized and vertically well-aligned and the length of CNT as a function of pressure (Figure 5.14) showed that the CNT length reached a peak at around 10 to 14 and then decreased steadily with minor fluctuations.

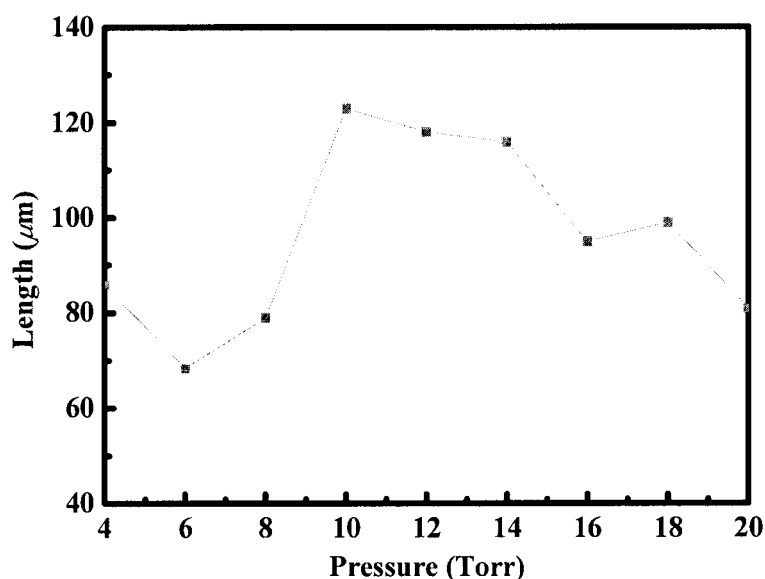


Figure 5.14. CNT length as a function of growth pressure.

The concentration of C₂H₂ molecules increased as pressure increased, hence the probability of the C₂H₂ gas molecules reacting with Fe catalyst nanoparticles increased. As a result, the increase in the formation of CNT led to a denser CNT array and increases CNT length with pressure initially. However, as the pressure

Chapter 5 Synthesis of carbon nanotubes by thermal chemical vapor deposition

was further increased from 10 Torr to 20 Torr, there was a gradual decrease in length. It could be possible that the concentration of C_2H_2 at this pressure was already near the equilibrium point. A further increase in pressure could not increase the growth of CNT but result in the formation of more defective carbon structures that deactivates the catalytic Fe nanoparticles. Hence, CNT length decreases gradually as the pressure was increased gradually to 20 Torr.

Figure 5.15 shows the relationship of the Raman intensity ratio of the grown CNTs under different pressures. The I_G/I_D ratio increases and reaches the highest peak at around 12 Torr but decreases drastically after 12 Torr. A probable explanation is similar to the explanation used for the trend in CNT length previously. At the lower pressure from 4 to 8 Torr, the concentration of C_2H_2 gas molecules was lower and hence there is less interaction between the C_2H_2 gas molecules to form ordered graphitic structures. As the pressure increased to 10 Torr, the rate of carbon consumption and supply approached the equilibrium point where the strongest G-band represents well-ordered graphite structures with lesser defects. However, beyond 12 Torr, the faster decomposition of C_2H_2 led to the generation of more disordered carbon structures such as amorphous carbon. This resulted in a more defective structure on the substrate which corresponded to a stronger D-band or lower I_G/I_D ratio.

In general, the amount of amorphous nanoparticles nucleated on CNT increase with higher pressure [22, 23]. It appears that the CNT grown at the pressure 12 Torr is the least defective, which is confirmed by a very high I_G/I_D ratio of 1.33 and

Chapter 5 Synthesis of carbon nanotubes by thermal chemical vapor deposition

substantial length of up to 118 μm is grown. Therefore, the optimal pressure to grow long and dense CNTs with high purity is 12 Torr.

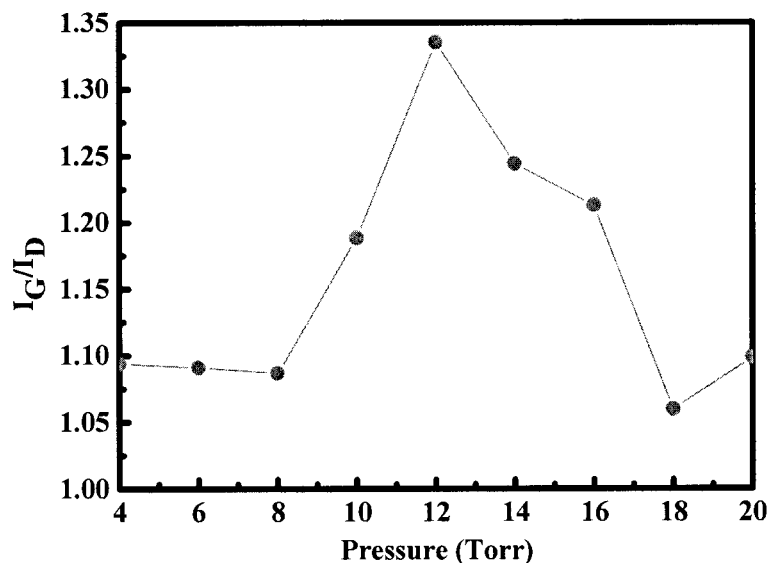


Figure 5.15. Raman intensity ratio I_G/I_D as a function of growth pressure.

5.3 Optimized results

After 5 series of experimental investigations on the influence of individual CNT synthesis parameters, the optimum parameters that can produce long and dense CNTs with good purity are summarized in Table 5.2. A sample wafer was loaded into the furnace to grow CNTs based on the above optimized parameters. An overall view of the vertically aligned CNT with the length up to 381 μm is shown in Figure 5.16 (a), and the close-up view of the dense CNTs is shown in Figure 5.16 (b). The diameter of the single CNT varies from 15 to 110 nm and the density of the grown CNT was estimated to be 90 per μm^2 . TEM was used to further investigate the detailed structure of the CNTs. The TEM image in Figure 5.16 (c) confirms the

Chapter 5 Synthesis of carbon nanotubes by thermal chemical vapor deposition

tube structure of the grown CNT, and no obvious defects are found throughout the tube.

Table 5 2. *Optimum Parameter from each set of experiment.*

Experiments	Investigated Range	Optimum Parameters
Catalyst thickness (nm)	2 – 10	2
Pretreatment time t_1 (min)	5 – 45	10
Temperature ($^{\circ}\text{C}$)	650 – 900	725
Growth time t_2 (min)	5 – 80	45
Flow rate of C_2H_2 (sccm)	5 – 100	25
Pressure (Torr)	4 – 20	12

As shown in the insert picture, the CNT diameter is around 14 nm and consists of 15 layers of well graphitized layer with an internal hollow core of approximately 4 nm in diameter. This observation is similar to that made by Li et al. for CNT grown at low pressure [128]. To understand the growth mechanism of the as-grown CNTs, we transferred the CNTs from the wafer by the Scotch tape. The black catalyst particles shown in Figure 5.16 (d) are in the direction towards the tape. In another words, they are located in the top position of the CNTs. This suggests the tip growth mechanism of the as-grown CNTs [129].

Chapter 5 Synthesis of carbon nanotubes by thermal chemical vapor deposition

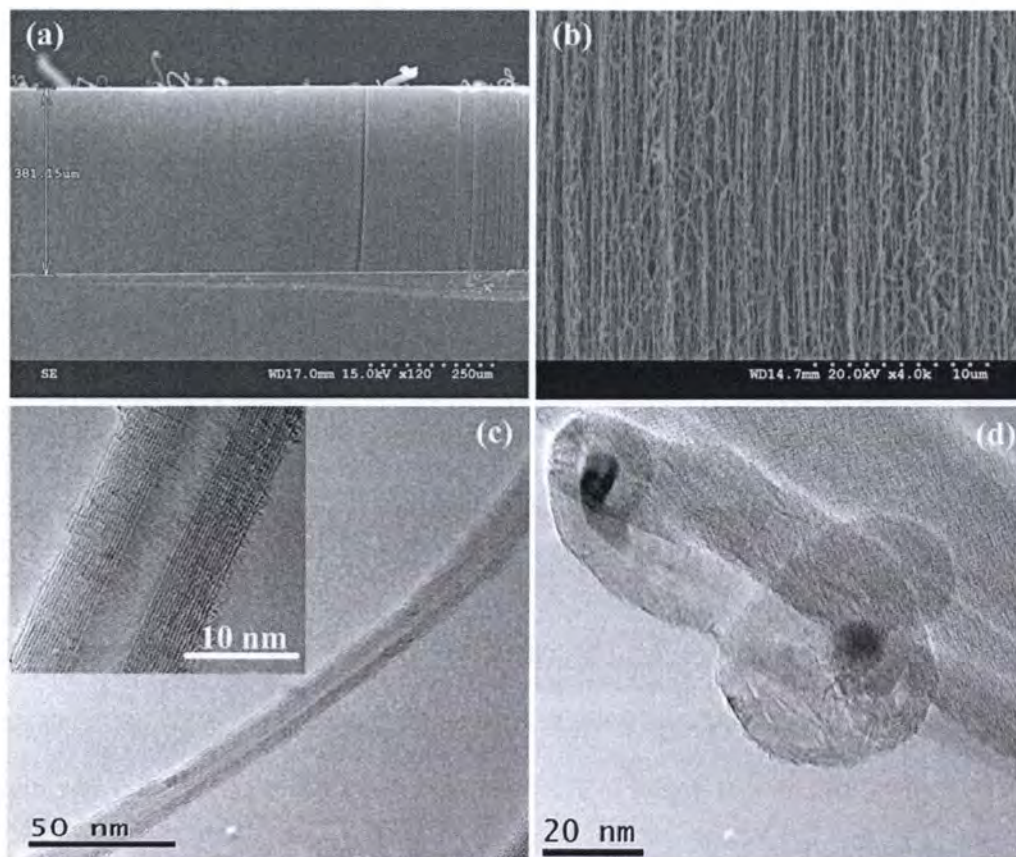


Figure 5.16. SEM and TEM images of aligned long CNT growing based on optimized parameters. (a) SEM image of long CNTs up to 381 μm, (b) close up view of the dense CNT, (c) TEM images of one single multi-walled CNT, the inset image shows the detailed structure, (d) two single CNTs with catalyst located at the tips.

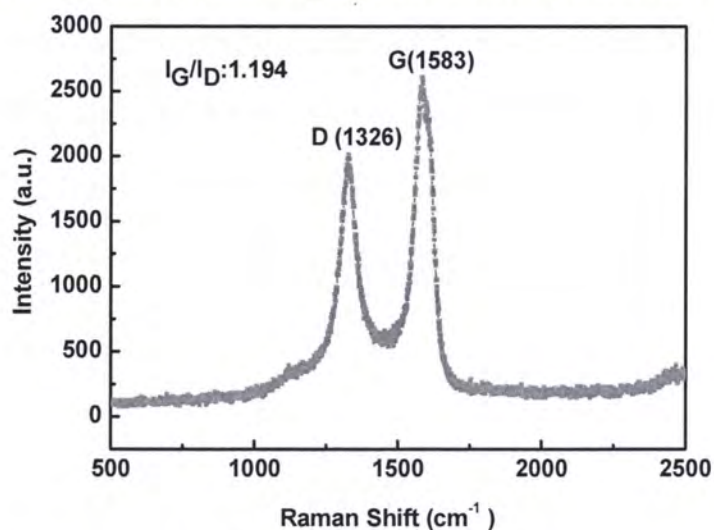


Figure 5.17. Raman spectrum of the grown CNTs based on the optimized parameters.

Chapter 5 Synthesis of carbon nanotubes by thermal chemical vapor deposition

The Raman spectrum shown in Figure 5.17 displays a strong G-band at 1583 cm^{-1} , a weak D-band at 1326 cm^{-1} and an intensity ratio of 1.194, suggesting that the CNTs grown in this process have highly-ordered graphitic tubular structures.

5.4 Summary of this chapter

The study was designed to study the influences of various synthesis parameters on the growth of CNT by TCVD. In particular, the effects of catalyst pretreatment time, growth temperature, growth time, gas flow rate, pressure on the overall vertical length of CNT, density and the quality of CNT were investigated in detail. It appears that all of the synthesis parameters studied here had an effect on both the length and quality of the CNT. The overall vertical length and quality of the CNT can be reliably controlled by varying either the growth temperature or C_2H_2 gas flow rate. In addition, catalyst pretreatment time and temperature also played an important role in controlling the size and density of catalyst particles, which affected the length and density of the grown CNT. A high quality long CNT with length up to $380\text{ }\mu\text{m}$ was successfully synthesized based on the optimized parameters. The optimized parameters for TCVD system will be used for synthesizing CNTs on the PZT diaphragm in the biosensors in the next chapter.

Chapter 6

Development of CNT enhanced piezoelectric biosensor array

In this chapter, two approaches were implemented to fabricate CNT enhanced biosensors. CNTs were directly grown from the sensor diaphragm in the first approach. Aligned dense CNTs were successfully synthesized; however, most of the top and bottom electrodes in the sensors were peeled off from the substrate due to the high temperature during the CNT growth process, which makes this method not practical for the development of CNT based biosensors. Hence, in the second approach, CNTs were pre-synthesized by thermal chemical vapor deposition. Afterwards, functionalized CNTs were applied into the reaction chambers in the sensors. Immobilization methods were optimized and the CNT enhanced biosensors were characterized by FSEM, AFM, Raman spectrum, AT-FIR and impedance analyzer. Results show that that the sensitivity, dynamic range of the CNT enhanced diaphragm based biosensors were 4 times higher than that of the normal piezoelectric biosensor.

6.1 Introduction

Sensitivity and limit of detection are the two crucial measures to judge the performance of a biosensor. With the same concentration of target analyte, a sensor

Chapter 6 Development of CNT enhanced piezoelectric biosensor array

with higher sensitivity can generate a stronger output signal. This is very important in clinic applications because it can provide clearer and more accurate information of the patients. On the other hand, the limit of detection refers to the minimum concentration of the analyte solution that can be detected by a biosensor, which is important for doctors to provide effective treatments or monitor patients in patients' early stage of illness. As mentioned in chapter 4, the circular diaphragm based piezoelectric biosensor has a better fabrication yield than that of the square one. However, the sensitivities of the developed biosensors are still relatively low.

Since the sensor design and fabrication processes can't be further modified, the best approach to improve the sensitivity of the above mentioned biosensor is to modify the sensing surface. Among various reported methods and materials, gold nanoparticles are the most common used material to enhance the sensitivity of the biosensors because of their unique physical properties to provide a three-dimensional platform [130-132]. However, this method is not suitable for micro-machined piezoelectric diaphragm-based biosensor. Because of the high density of the gold, the deposited gold particles may cause micro-mechanical deformation of the thin piezoelectric diaphragm. In addition, the gold particle modified platform also exhibits reliability problems during the immobilization process due to the point-of-contact between the individual particle and the plain surface. As such, CNTs will be used as an alternative material to gold particles in this study. One of the extraordinary features of a CNT would be its extremely high specific surface area, which is ranked the highest among all the nanomaterials. Theoretical calculations have predicted that the specific area for single/multi walled CNT can be as high as 900/400 m²/g [8,9,133].

Chapter 6 Development of CNT enhanced piezoelectric biosensor array

As shown in Figure 6.1 (a), if molecules can only attach onto the plain surface, the total number of the absorbed molecules is determined by the total area of the solid surface. However, CNTs possess high specific areas, when CNTs are integrated with the plain surface and form a 3-dimensional sensing surface (as shown in Figure 6.1 b), under the same concentration and solid sensing surface area, a much larger number of molecules can be absorbed by the CNT modified sensing surface, resulting in much more interaction between the probe molecules and the target analytes. Therefore, CNTs serve as an amplifier to enhance the output signals, as a result, the sensitivity and the limit of detection will be dramatically increased [134]. Recently, some researchers demonstrated CNT's ability to enhance the electrochemical reactivity of some important biomolecules [135-137] and its usefulness for label-free electrochemical detection of DNA hybridization [138]. However, in the reported methods, most of them were depositing CNTs on the electrodes and applying voltage across the CNTs, which may cause certain damage to the proteins and make the testing process unstable and inaccurate.

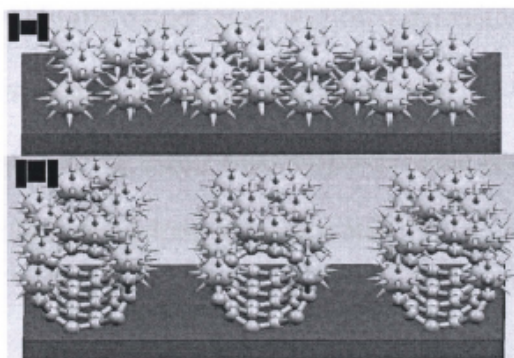


Figure 6.1. Sketch of the sensing platform for attaching molecules. (a) Plain surface, (b) CNTs modified surface.

Chapter 6 Development of CNT enhanced piezoelectric biosensor array

As such, in this chapter, we aim to incorporate CNT on the piezoelectric diaphragm to make a CNT-enhanced mass-sensitive biosensor. The design, fabrication and characterization of the devices will be reported in detail in the following sections.

6.2 Development of piezoelectric diaphragm-based biosensor with direct growth CNTs

6.2.1 Fabrication processes

The piezoelectric diaphragm was fabricated by micro-fabrication technique and it involved 6 main steps. The schematic process flow of the fabrication is illustrated in Figure 6.2. In the first step, a 1.8 μm -thick thermal silicon oxide (SiO_2) layer was grown on a 4-inch double-sided polished silicon wafer as a supporting structure layer. A silicon nitride (Si_3N_4) layer of 200 nm, which was used to compensate the compressive stress within the oxide layer, was then deposited on both sides of the wafer by Low Pressure Chemical Vapour Deposition (LPCVD). The Si_3N_4 and SiO_2 layers at the bottom side of the wafer were removed using Reaction Ion Etch (RIE) for the convenience of silicon etching in the last step.

Chapter 6 Development of CNT enhanced piezoelectric biosensor array

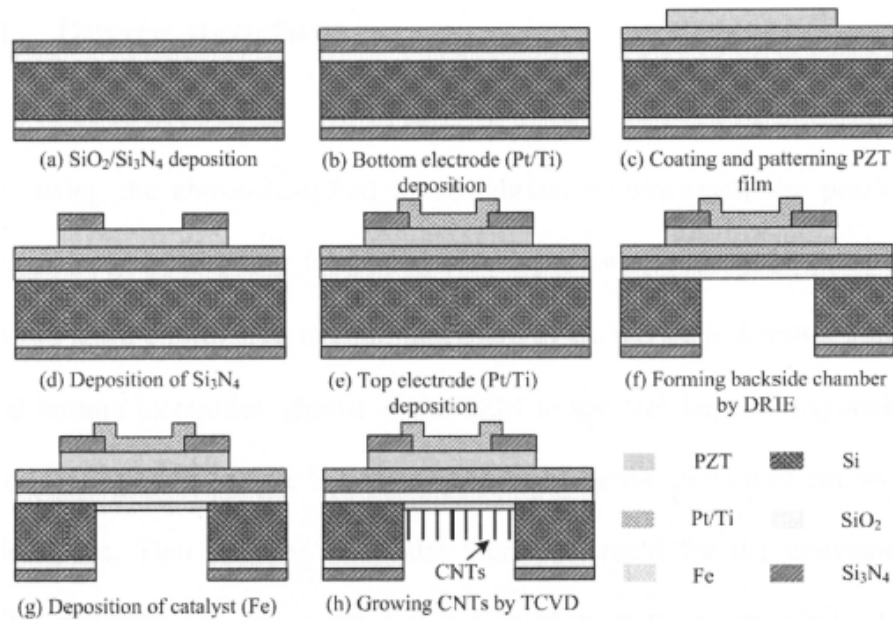


Figure 6.2. Schematic diagrams of fabricating the piezoelectric diaphragm and growing CNTs.

In the second step, the bottom electrode (Ti/Pt: 20/200 nm) was deposited by sputtering and patterned by the lift-off process. PZT layer with composition at morphological boundary was deposited using sol-gel technique [88]. As shown in Figure 6.2 (c), PZT was wet etched in the specific area by diluted HCl:HF (50:1) solution to open a window for access to the bottom electrode pad. After that, a Si_3N_4 layer was deposited by PECVD and patterned by RIE as an insulation layer to reduce the parasitic capacitance induced by the leading wires. The top electrode (Ti/Pt: 20/200 nm) was sputtered and patterned on the front side by the lift-off process. At the end of the fabrication, the backside silicon was etched by DRIE until the exposure of the thermal oxide layer. The last two steps shown in Figure 6.2 present the CNT growing process and will be discussed in details in Chapter 6.2.4.

6.2.2 Device structure

By using the above-described micro-fabrication processes, the piezoelectric diaphragm was successfully fabricated. The top view of the fabricated device is shown in Figure 6.3 (a). The overall dimension of the device is 5 mm × 5 mm. The top and bottom electrodes, shown in the SEM image, are located diagonally. The two quarter segments are the bottom electrodes while the two outer circles are the top electrodes. Two pairs of electrodes were fabricated for the convenience of electrical measurement. The piezoelectric diaphragm is the centre circle shown in the image. Figure 6.3 (b) presents the back view of the device. CNTs will be grown on the bottom of the deep circular hole and it will be used as a reaction chamber during the biomaterials immobilization process. The diameters of the designed holes range from 400 to 1200 μm and the depth is about 350 μm . It can be seen that the bottom surface of the deep circular hole, which is actually the thermal oxidation layer, is quite smooth and this facilitates the catalyst deposition during the CNT growing processes. A detailed view of the multilayer structure of the piezoelectric diaphragm is also shown in Figure 6.3 (c). The PZT film was deposited layer by layer, and after each layer was deposited, it was annealed at 600 °C for 15 min. Therefore, a few interfaces within the PZT layer were observed in the SEM image. The average thickness of the PZT film was about 0.8 μm . The thickness of the top electrode (Ti/Pt) was too thin to be seen under this magnification.

Chapter 6 *Development of CNT enhanced piezoelectric biosensor array*

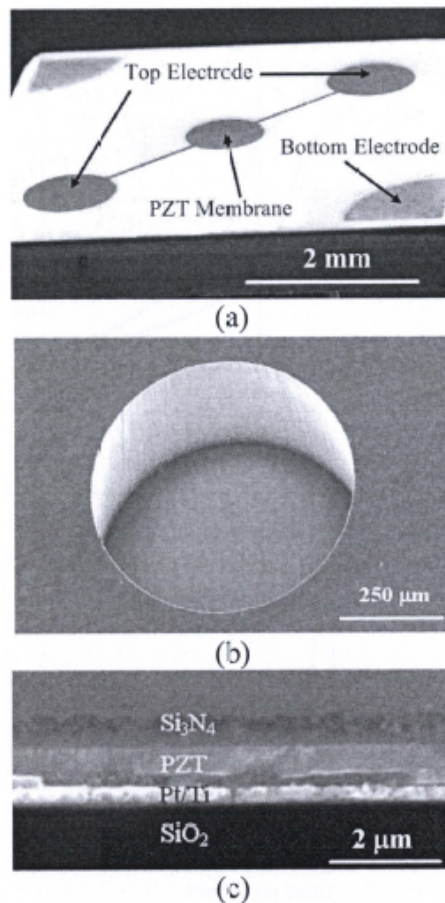


Figure 6.3. SEM images of the fabricated device, (a) top view of the device, (b) backside view of the reaction chamber, (c) detailed cross sectional view of the PZT diaphragm structure.

6.2.3 Characterization of PZT diaphragm

After the piezoelectric diaphragm was successfully fabricated, its ferroelectric property was characterized and its P-E hysteresis loop was measured, which is presented in Figure 6.4 (a).

Chapter 6 Development of CNT enhanced piezoelectric biosensor array

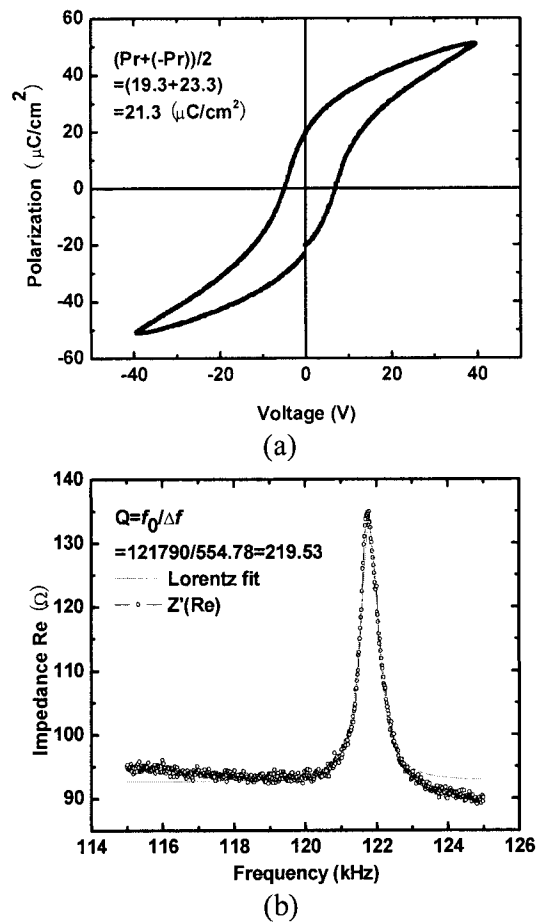


Figure 6.4. Characterization of the PZT film on the device, (a) P-E hysteresis loop of the PZT diaphragm, (b) the Q factor is as high as 219 at relatively low operating frequency.

The shown polarization of $21.3 \mu\text{C}/\text{cm}^2$ indicates that the PZT diaphragm exhibits very good ferroelectric properties. The performance of the PZT diaphragm was characterized using an impedance spectrum. An Agilent 4294A impedance analyzer was used to test the fabricated PZT diaphragm with diameter of 0.8 mm. A probe station was also used to connect the analyzer and the top/bottom electrodes of the diaphragm. Figure 6.4 (b) shows the impedance spectrum of the PZT diaphragm in air at one of the flexural resonant modes. The obtained high Q value (219) at a

Chapter 6 Development of CNT enhanced piezoelectric biosensor array

low operating frequency (~122 kHz) proved that the PZT diaphragm fabricated in this work was well functioning.

6.2.4 Synthesis of CNT on PZT diaphragm

(i) CNT synthesis processes

After the fabrication and characterization of the PZT diaphragm, we further grew CNT on the backside of the diaphragm to prepare the CNT-enhanced biosensor. The sketched fabrication process was presented in Figure 6.2 (g) - (h). In the first step, an iron (Fe) catalyst layer with a thickness of 5 nm was deposited onto the silicon oxide surface, which was at the bottom of the PZT diaphragm, by electron beam evaporator. The patterned photoresist in the last step of the PZT diaphragm fabrication was not removed, and it acted as the mask to ensure the catalyst can only be deposited onto the backside of the diaphragm.

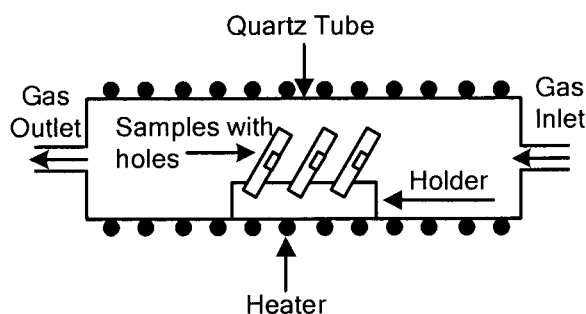


Figure 6.5. A set up diagram for growing CNTs on the backside of PZT diaphragm inside quartz tube.

After the catalyst layer was deposited, the wafer was cut into small samples according to the overall size of the device. The samples were placed in a 4-inch

Chapter 6 Development of CNT enhanced piezoelectric biosensor array

barrel quartz tube to grow CNTs by TCVD at a temperature of 725 °C. Figure 6.5 shows the schematic diagram of a TCVD quartz tube for CNT growth. Process gases flow into the quartz tube from the inlet and exhaust through the outlet. During the CNT growing process, the wafer should be placed inclining about 20° to ensure that sufficient process gases to reach the catalyst film. Otherwise, there would be no or very thin short CNT growth on the diaphragm [139]. The distance between two samples was about 5 cm and the growing parameters are the same as the optimized values reported in chapter 5.

(ii) CNT incorporated piezoelectric diaphragm

Figure 6.6 shows the SEM images of the PZT diaphragm after the CNTs growth. The backside view of the device is shown in Figure 6.6 (a), in which the bottom surface of the deep hole seems to be quite rough comparing with that before CNT growing shown in Figure 6.3 (b) due to the CNTs grown on the surface. It can be seen from the image that the central dark part is actually the bottom electrode located on the other side. A close-up view of the CNTs is shown in Figure 6.6 (b). It can be clearly seen that CNTs grew on the backside of PZT diaphragm. The inserted images show the CNTs grown on different locations on the surface. An annular shape formed by the grown CNTs on the surface implies that the length of the grown CNTs varies throughout the diaphragm surface. The CNTs grown near to the edge of the hole are longer than those in the centre location. This is a very interesting phenomenon and it can be explained by the following. During the catalyst deposition process, ideally, the Fe atoms were uniformly deposited on a flat

Chapter 6 Development of CNT enhanced piezoelectric biosensor array

surface. However, due to the deep hole, some of Fe atoms bombarded to the wall and fell onto the centre positions leading to a thicker deposited catalyst layer. Hence, the CNTs were grown with non-uniform length.

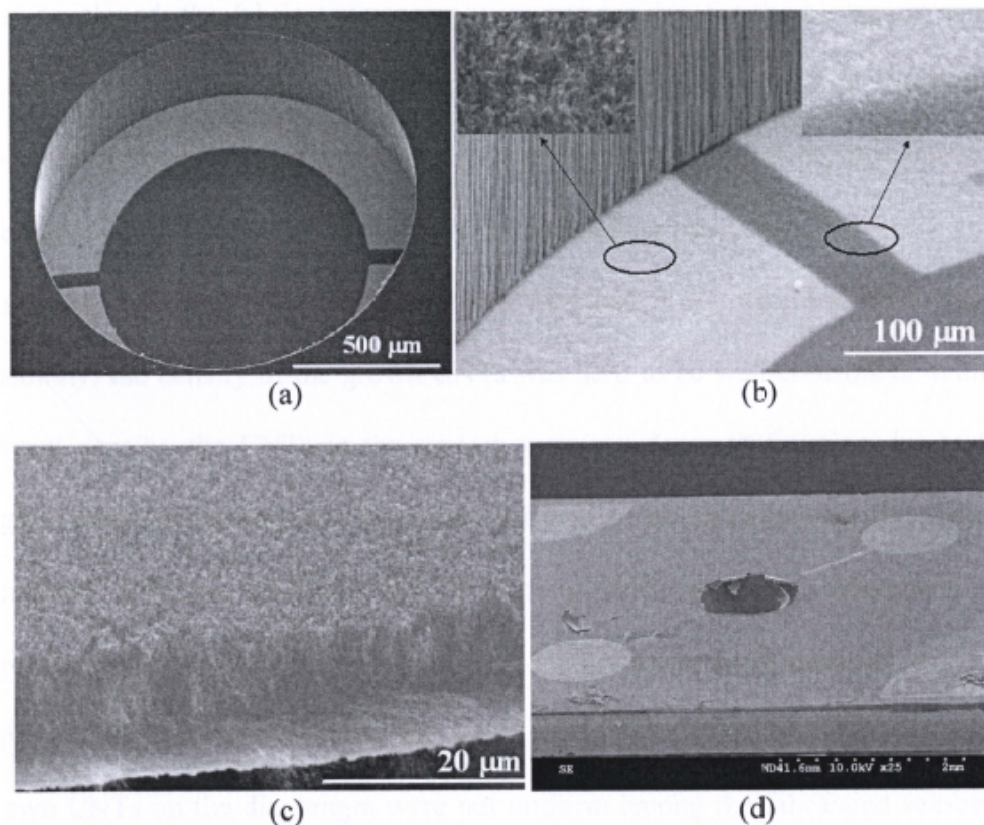


Figure 6.6. SEM images of the PZT diaphragm with CNTs, (a) backside view of PZT diaphragm, (b) a close-up view of bottom surface of the deep hole, (c) cross section of the PZT diaphragm with CNTs, (d) PZT film together with top electrode was peeled off.

Figure 6.6 (c) shows the cross-sectional view of the grown CNTs which are well-aligned. The properties of PZT films have no significant change in some of the devices after the CNT growing process. Nevertheless, most of the PZT films together with the top electrodes were peeled off from the substrate after growing CNT (Figure 6.6 (d)). This is possibly due to the mechanical stresses accumulated

Chapter 6 Development of CNT enhanced piezoelectric biosensor array

in the previous processes and the thermal stresses induced during the high temperature CNT growing process.

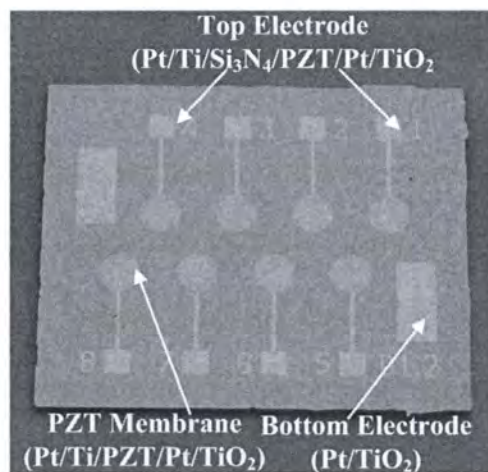
Although a novel method of integrating CNTs onto the piezoelectric diaphragm was developed, the fabricated sensors were not suitable for the biological sensing due to the following reasons. Firstly, the yield of producing CNT incorporated sensors with good electrical and mechanical properties is relatively low due to the mechanical and thermal stresses during the fabrication processes. The stresses were caused by the nature of the processes and therefore, it is unlikely to be overcome. Secondly, the density of the grown CNTs was hard to be well-controlled. With the current density, the CNTs in the sensors were too dense to function due to their highly hydrophobic nature. CNTs were difficult to be immersed by the chemical treatment solutions. Without the hydrophilic treatment, the subsequent bio-immobilization was difficult to be realized. Lastly, it was a challenge to control the uniformity of the CNTs within the holes with high aspect ratio. The lengths of grown CNTs on the diaphragm were not uniform among the fabricated sensors; in fact, as mentioned previously, the lengths of the CNTs in different location were varied even within one sensor. This non-uniform grown CNTs will definitely affect the sensors performance in terms of uniformity and reproducibility. As a conclusion, it is not practical to use the CNT-integrated sensors developed by the above-described method for the biosensing application. A new technique to fabricate CNT enhanced biosensors is thus required.

6.3 Development of piezoelectric diaphragm-based biosensor with CNT deposition

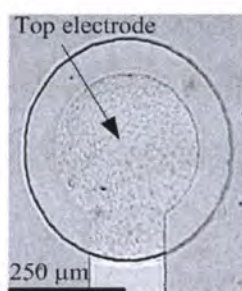
6.3.1 Device fabrication

The piezoelectric sensor arrays were fabricated with similar processes as described in chapter 4.3.1 with the exception of the top electrode design and the diameter of the reaction chamber. In chapter 4, the top electrode fully covered the piezoelectric diaphragm. However, beside the original design, two more designs, namely, small solid shape and ring shape were added in this section to investigate the impact of the diaphragm structure on the sensor sensitivity. The diameters of the reaction chambers for the sensor array varied from 0.4 mm to 1.2 mm and they have the same diameter within one sensor chip. As seen from the fabrication results shown in Figure 6.7 (a), one sensor chip consists of 8 individual sensors which have fully covered top electrodes. Figure 6.7 (b) and (c) shows the enlarged image of the sensor top electrode with small solid and ring shape, respectively. The diameter of the small solid top electrode is 0.7 times that of the solid electrode, therefore, the surface covered by the small solid electrode is just half of the solid electrode. The ring shaped electrode has the same area as that of the small solid electrode.

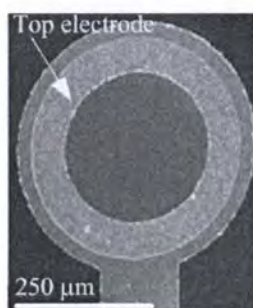
Chapter 6 Development of CNT enhanced piezoelectric biosensor array



(a) Sensor arrays with solid top electrodes



(b) Sensor with small solid top electrode



(c) Sensor with ring shaped top electrode

Figure 6.7: Pictures of the fabricated sensor array with different top electrode shape. (a) Solid top electrode, (b) small solid electrode, (c) ring shaped electrode.

6.3.2 Characterization of the sensor array

After the fabrication, the frequencies of the sensor arrays were measured by an impedance analyzer. The frequencies shown in Figure 6.8 are the average measured values of the 8 individual sensors. It is clear that for the same shape, the frequency decreases as the diaphragm diameter increases for all the three shapes of top electrodes. This result is expected since the mass of the diaphragm is proportional to its diameter. Referring to the resonant frequency definition by Eq.3.2 in chapter 3, the frequency is inversely proportional to the mass of the diaphragm when the rigidity of the diaphragm remains unchanged for the same electrode. Therefore, the larger diaphragm has a bigger mass and result in a lower resonant frequency.

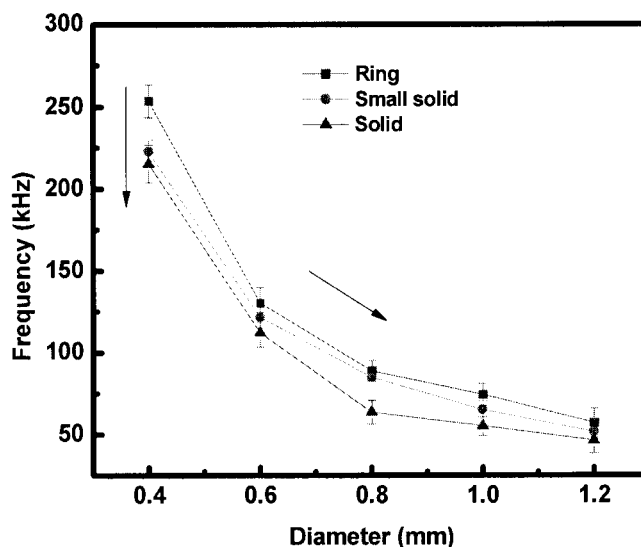


Figure 6.8: Relationship between the resonant frequency of sensors with different top electrode shape and the sensor diaphragm diameter.

Chapter 6 Development of CNT enhanced piezoelectric biosensor array

For the diaphragms with the same diameter, the results presented in Figure 6.8 reveals that the diaphragms with ring shaped top electrode have the highest frequency, while those with solid top electrode have the lowest frequency. Although the three top electrodes have different shapes, they have negligible impacts on the rigidity due to the small thickness of the top electrode. Hence, the diaphragm mass of the sensor is the dominant to affect its resonant frequency. Among the three electrodes, the mass of the solid electrode is the highest which leads to the lowest resonant frequency. Ideally, the sensors with ring and small solid shaped top electrodes have the same diaphragm mass due to the same surface areas. However, the wire connected to the small solid top electrode was also located on the diaphragm, which resulted in a larger mass than that of the ring shaped top electrode. Hence the frequency of the small solid is slightly lower than that of the sensor with ring shaped top electrode.

Since the sensor chip was fabricated with the same processes and parameters with those sensors reported in Chapter 4.3, gravimetric sensitivities (S_M) for solid, small solid and ring shaped sensors were calculated to the same as $-45.33 \text{ m}^2/\text{kg}$. However, according to Eq. 3.43, the mass sensitivity (S_m) is proportional to the resonant frequency (f_0) when the sensing area (A) and gravimetric sensitivity (S_M) are the same. Based on the results present in Figure 6.8 and it is obviously that the sensors with ring shaped electrode have the highest resonant frequency; therefore, the ring shaped sensors will have the highest mass sensitivity and be the focus in this project.

Chapter 6 Development of CNT enhanced piezoelectric biosensor array

Sensors with diameters of 0.4 mm are not studied because the reaction chambers are too small for the convenience of the bio-immobilization. Hence, by considering the sensitivity and convenience of bio-immobilization the ring-shaped top electrode sensors with diameters of 0.6 mm and 0.8 mm will be used for further study on the CNT enhanced biosensor.

6.3.3 Optimization of immobilization method

The sensitivity and reproducibility of a biosensor is largely influenced by the amount of probe molecules fixed on the diaphragm surface. Therefore, the binding between the bioreceptors and the sensing surface is crucial in the first step. The biomaterials, frequently refer to proteins in this work, can be fixed onto the solid sensing surface via covalent binding and non-covalent binding. Covalent binding provides a strong covalent bond between the proteins and the sensing surface. By using non-covalent immobilization method, the proteins can be attached to the solid surface by physical force or passive adsorption.

In chapter 4, the proteins were fixed onto the gold-coated solid surface through non-covalent adsorption, as this is the easiest and quickest method. One serious drawback of this method is the weak bonding between the solid sensing surface and the proteins. Some of the attached proteins may be washed away during the cleaning process, which significantly reduces the reliability and reproducibility of this process. Therefore, in this chapter, three types of sensing surface modifications were conducted to optimize the immobilizing technique. The first one was covalent

Chapter 6 Development of CNT enhanced piezoelectric biosensor array

binding of the proteins to the silica surface via a thin layer of 3-Glycidoxypropyl-trimethoxysilane (GPTS). Thin films of GPTS are commonly used to promote covalent adhesion between silica substrate and organic materials for applications ranging from advanced composite to biomolecular micro-devices [140,141].

In the case of GPTS-modified silica surface, CH₃ groups in one end of GPTS are covalently bonded onto the silicon oxide surface via the Si-O bond [142], while the epoxy ring in the other end are not cleaved and are available for the covalent binding with the amine groups from proteins, such as goat antigen. In the second approach, polyethyleneimine (PEI) was coated onto the silica substrate to absorb proteins. PEI is a polymeric amine with a high charge density that allows it to be absorbed tightly on negatively-charged substrates. Although protein adsorption by PEI may be quite random, it is a reversible immobilization process and a very effective tool to achieve very intense adsorptions with low cost [143-145]. In the last approach, proteins will be directly attached onto the sensing surface without any modification.

(i) Experimental details

Three sensor chips with same diameter of 0.8 mm were used for the optimization. In the first sensor chip, a mixed solution of H₂O₂ and H₂SO₄ was added into all the reaction chambers to form the –OH groups on the surface. The sketched immobilization processes are described in Figure 6.9. For the first chip, GPTS (5%) was firstly dropped into all the reaction chambers in the chip, and it was

Chapter 6 *Development of CNT enhanced piezoelectric biosensor array*

kept for 30 min in room temperature. Afterwards, the chip was washed by ethanol (95%) and DI water. After drying by N₂ gas, the chip was placed into a hot chamber with a temperature of 110 °C for 1 hour. Secondly, goat IgG (100 mg/ml) with glycerin (2.5%) was applied into all the reaction chambers and the sensor chip was kept in the hot chamber with temperature of 37 °C for 30 min and followed by TBS and DI water washing. In the third step, blocker casing (200 mg/ml) with 0.05% Tween 20 was used to block the open surfaces.

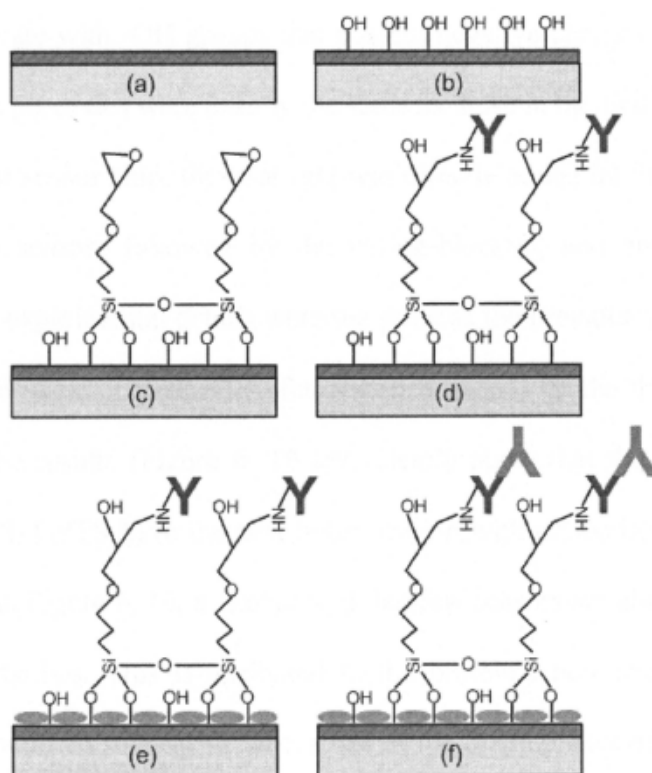


Figure 6.9: Sketched process flow for immobilization of GPTS. (a) plain silicon substrate with SiO₂ film, (b) H₂O₂/H₂SO₄ treatment brings Si-OH groups onto silica surface, (c) GPTS covalently bond to the oxide surface and cross-link the silane groups after thermal curing, (d) goat IgG bond to the GPTS coated surface through the open epoxy ring, (e) blocker blocks the open space on the substrate, (f) anti-goat IgG couples with goat IgG [142].

Chapter 6 Development of CNT enhanced piezoelectric biosensor array

After depositing for 30 min at 37 °C, the sensor chip was washed by TBS and DI water again. Lastly, anti-goat IgG (10 µg/ml) with Cy3 labels was applied into each sensor and cultured for 30 min at 37 °C. After that, the chip was washed and dried out by N₂ gas.

For the second sensor chip, PEI (10 mg/ml) diluted in DI water (2mg/ml) was added into all the sensors and the chip was kept for 1 hour at room temperature, then followed by DI water washing and N₂ drying. PEI can be tightly absorbed by the silica substrate with -OH groups that possess negative charges. The subsequent immobilization processes were exactly the same as those in the first experiment.

For the last sensor chip, the goat IgG was directly added into the plain sensing surface of the sensors followed by the casing-blocking and antibody-capturing processes. The experimental details were the same as the previous two sensor chips. After the immobilization processes, fluorescence images of the three sensor chips were taken. The results (Figure 6. 10 left) clearly show that the goat IgG in the sensor chip with GPTS have the best hybridization with antibodies. As the middle picture shows in Figure 6. 10, it is observed that few sensors are able to successfully detect the antibodies. This is attributed to the protein's non-oriented attachment onto the PEI-modified sensing surface; some of the binding sites of the antigens are attached onto the PEI polymer thus rendering it unable to capture the antibody.

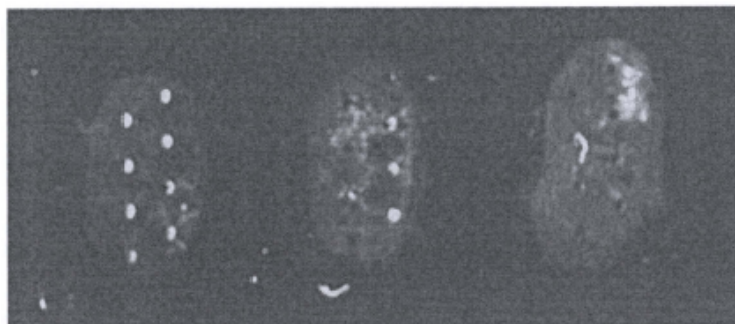


Figure 6. 10: Fluorescence images for the three sensors with different buffer layers. Left: GPTS, Middle: PEI and Right: Plain surface.

No clear fluorescence images of the sensors were founded in the last chip, which implies that either the antigens were washed away during the process or very few antibodies captured by the antigens. Hence, GPTS-modified sensing surface is the best choice for the immobilization. The following sections will discuss the processes and characterization of applying functionalized CNTs into the sensors to enhance the detecting sensitivity and limit of detection.

(ii) Functionalization of CNTs

Functionalized CNTs solutions are typically dispersed onto a silicon substrate surface to facility the characterization. However, CNTs tend to form aggregates and are not soluble in water due to their extremely strong Van der Waals interactions. It is necessary to conduct certain chemical or physical treatments to change the CNTs into hydrophilic.

As the typical experiment reported by Lin et al., a CNT sample (100 mg) was heated and refluxed in an aqueous HNO₃ solution (3.2 M, 50 mL) for 48 hours [146]. The suspension was then centrifuged at 10000 g for 30 minute to recover

Chapter 6 Development of CNT enhanced piezoelectric biosensor array

CNTs, followed by repeated thorough washing with DI, CNT solution was re-centrifuged and the collected solid was vacuum-heated at 120 °C for 4 hour, resulting in a dark and glassy solid product. The sample CNTs were purified after the treatments, as the iron catalyst compounds being removed during this process. CNTs were hydrophilic after this chemical treatment and were used for functionalization.

Before the bio-immobilization, CNTs were functionalized with GPTS, which is generally expected to drastically reduce non-specific binding of biomolecules via hydrophobic interaction. GPTS with the epoxy ring can then be used for covalent attachment of proteins or biomolecules [147]. A CNT pellet was dispersed in 5% (diluted in ethanol) GPTS for 1 h and sonicated for 45 min, followed by 1 h of stirring.

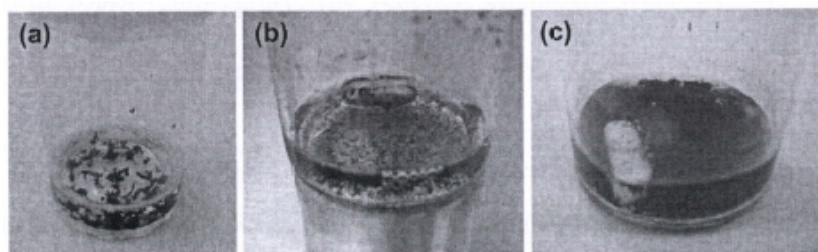


Figure 6.11: Pictures of CNTs solution. a) Un-dispersed CNTs in HNO_3 solution for 1 h, b) GPTS functionalized CNTs after 10 min of sonication, c) uniformly dispersed CNT solution after the complete sonication and stirring process.

Figure 6.11 shows the pictures of CNT solution at different stages. In the beginning, CNTs without any treatment form aggregates and are not soluble in the HNO_3 solution (Figure 6.11 a). Figure 6.11 (b) shows the CNT pictures after HNO_3 treatment and functionalized with GPTS followed by 10 min of sonication. In the end of the process, CNTs are uniformly dispersed in the solution which appears as black

ink (Figure 6.11 c).

(iii) Bio-immobilization

To investigate the effect of the CNTs on the detection sensitivity, two identical sensor arrays were used during the experiment. Before the bio-immobilization, one sensor array was first deposited with CNTs. The sketched immobilization processes are depicted in Figure 6.12. Firstly, the GPTS functionalized CNT solution was dropped into the reaction chambers in the first sensor array by . The reaction chambers for depositing GPTS were pretreated with mixed solution of H₂O₂ and H₂SO₄ at 70 °C to form –OH group to facilitate the covalent bonding between the GPTS-functionalized CNTs and the diaphragm with SiO₂ layer. After 45 min deposition at room temperature, the reaction chambers were washed by ethanol. Secondly, goat IgG (100 µg/ml) was added in both sensor arrays. The two sensor arrays were loaded into the culture chamber (~ 37 °C) for 30 min, and then washed by Tris-Buffered-Saline (TBS washing buffer, pH8.0) and DI water and dried under nitrogen (N₂) air flow. Afterwards, blocker caseins (1 mg/µl) were added to block the unoccupied space to avoid any unexpected physical absorption. The excess blockers were washed away by TBS and DI water. Lastly, anti-goat IgGs with concentration of 0, 0.1, 1, 10, 100, 1000, 10000 and 100000 ng/ml were dropped into 8 sensors in each array for the coupling between the antigens and antibodies. The sensor without any antibodies (0 ng/ml) added was used as reference.

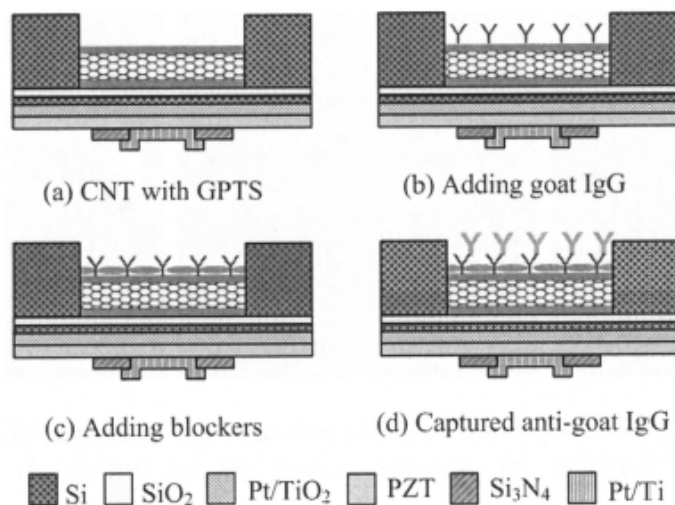


Figure 6.12: Sketched immobilization processes for the CNT enhanced PZT biosensor.

(iv) Characterization of CNT structures

For the convenience of characterization, one drop of CNTs solution was applied onto a small piece of plane silicon oxide wafer. All the experimental conditions were the same as that of the above mentioned CNT enhanced biosensors. Figure 6.13 shows the SEM images of one reaction chamber before and after CNT deposition. As shown in Figure 6.13 (a), the bottom surface of the reaction chamber is smooth; however, it becomes rough after the CNT deposition (Figure 6.13 b). It can be clearly seen the deposited CNTs from the enlarged image shows in Figure 6.13 (c).

Chapter 6 Development of CNT enhanced piezoelectric biosensor array

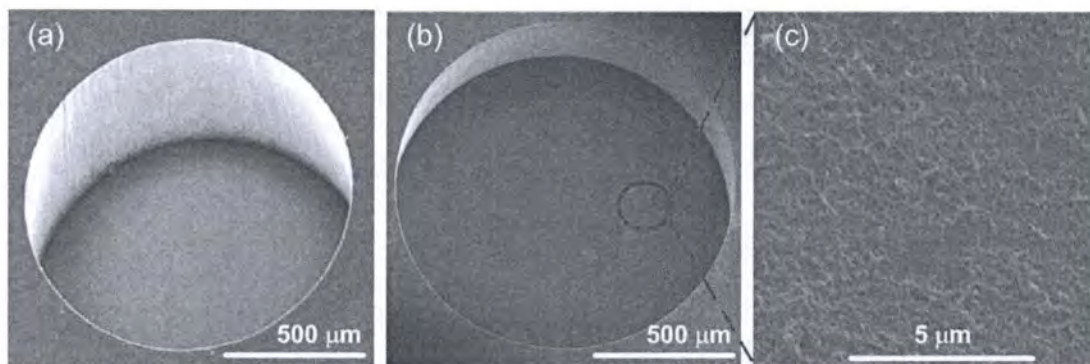


Figure 6.13: SEM images of one reaction chamber, (a) before the CNT deposition, (b) after CNTs deposition on the bottom surface, (c) enlarged image of the deposited CNTs.

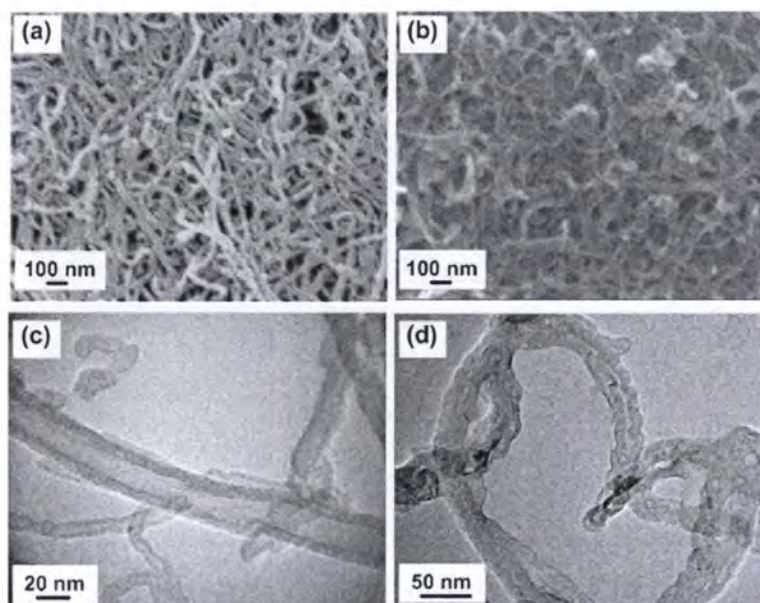


Figure 6.14: FSEM and TEM images of the functionalized CNTs. (a) & (c) are the images of acid pre-treated CNTs, (b) & (d) are the images of CNTs immobilized with goat IgGs.

The FSEM micrograph (Figure 6.14 b) shows that IgG-CNTs exhibit porously-packed nano-structured morphology comparing with that shown in Figure 6.14 (a). TEM image (Figure 6.14 c) of HNO_3 treated CNTs shows smooth side walls, whereas TEM image illustrates unevenly distributed goat IgG molecules attached

Chapter 6 Development of CNT enhanced piezoelectric biosensor array

onto the CNT surfaces (Figure 6.14 d). The CNT diameters were expected to increase after absorbing the bio-molecules and AFM was used to study the diameter variation during the immobilization process. Figure 6.15 shows the AFM images across the different immobilization stage. From the AFM images, it can be seen that the functionalized CNT surfaces are relatively smooth after the HNO₃ treatment. However, in the subsequent processes, CNT diameters are not always uniform along the tube axis, some portions protrude out due to the absorbed biomolecules during each immobilization process.

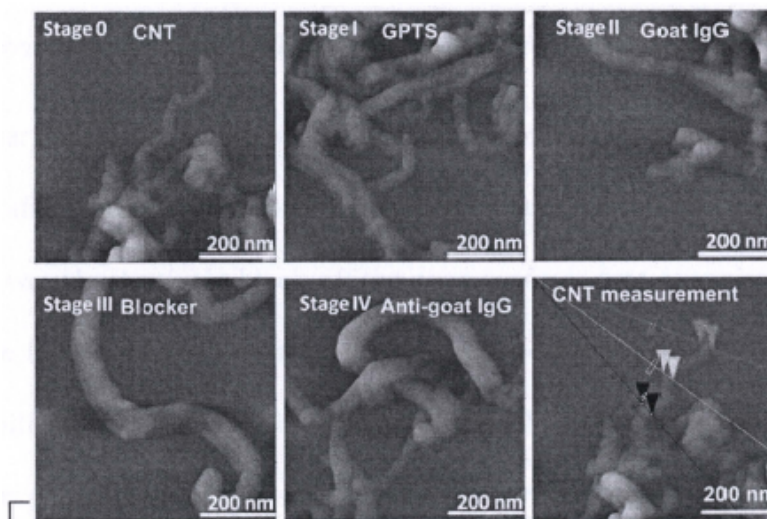


Figure 6.15: AFM image CNTs across immobilization stages. Stages 0-IV are representing CNT, CNT+GPTS, CNT+GPTS+goat IgG, CNT+GPTS+goat IgG+blocker and CNT+GPTS+goat IgG+blocker+anti-goat IgG, respectively. The last picture shows the CNT diameter measurement procedures.

CNT diameters were measured by AFM, and the results shown in Figure 6.16 are the average values after 3 measurements at different portions (shown in the last image in Figure 6.16). As shown in Figure 6.16, acid-treated GPTS-functionalized CNTs possessed an average diameter of 52 nm. Their diameters then gradually increased to 79 nm following the GPTS and goat IgG attachments.

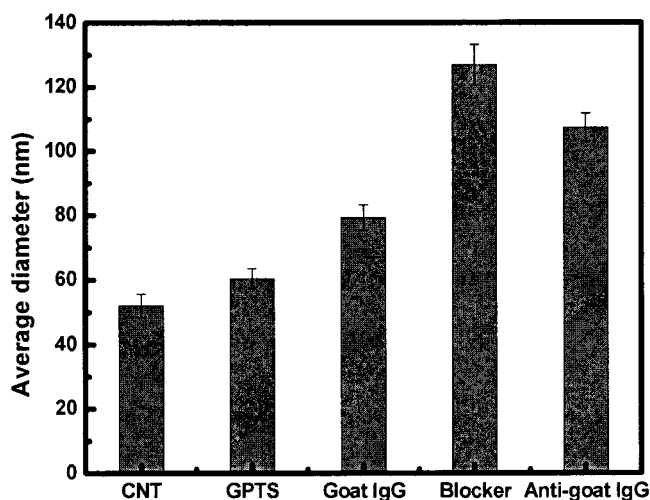


Figure 6.16: Average CNT diameter at different immobilization stages.

However, there is a sharp increase (approximately 37.49%) in the CNT diameters after adding of blocker molecules at stage III. Although the blocker molecules would selectively block off the open surfaces (not occupied by the goat IgG) of the functionalized CNTs, they could also possibly bind on the surfaces of the immobilized goat IgG molecules via passive physical absorption. This would explain the phenomena of the sharp diameter increase. In the last stage IV, the conjugated binding between goat IgG and anti-goat IgG molecules occurred on the surfaces of the functionalized CNTs. This specific hybridization process binds the goat IgG and anti-goat IgG molecules and could have yielded some end-products, which were washed away during the cleaning process. In addition, the passive attached blockers in stage III were properly washed away in the end of stage IV. Therefore, the CNT diameter at stage IV is smaller than that of stage III. Nevertheless, it is still larger than that of the first two stages.

(v) Raman characterization of the functionalized CNTs

The D-band in the Raman spectrum is associated with the level of lattice distortion within the carbon and it is common for disordered sp^2 carbon, whereas the G-band originates from tangential C-C stretching vibrations both longitudinally and transversally on the well-ordered CNT and is influenced by the diameter and chirality of the CNTs [149]. As shown in Figure 6.17, the D- and G-band of the functionalized CNTs at different processes are ~ 1328 and ~ 1584 , respectively.

There is a strong peak around the 500 cm^{-1} region across all the immobilization stages which is known as the radial breathing mode (RBM), indicating the presence of SWCNTs within the CNTs [150]. Another constant peak ($\sim 2625\text{ cm}^{-1}$) can be attributed to the reflection from the SiO_2 wafer substrate.

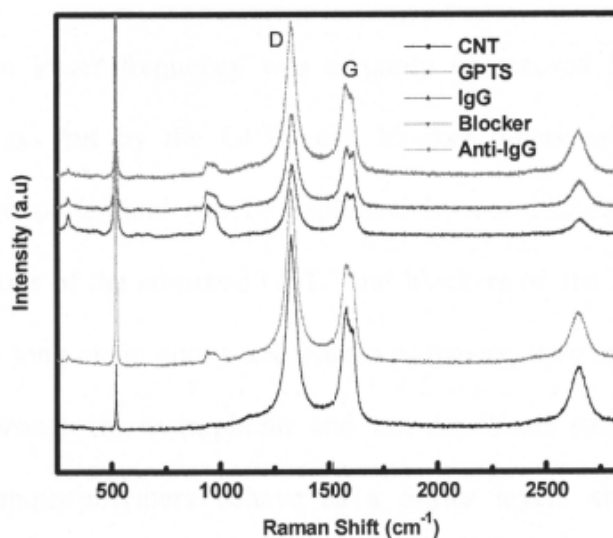


Figure 6.17: Raman spectrum of the CNTs across biomaterial immobilization stages.

Chapter 6 Development of CNT enhanced piezoelectric biosensor array

After GPTS was drafted onto the CNT surface, two weak spikes appear around the region of 280 and 956 cm^{-1} across the subsequent immobilization stages. This may be caused by the CH_2 and CH_3 bonds from the GPTS.

The change of spectral position of G-band after each immobilization process can be found. The G-band and D-band in the CNT Raman spectrum at each process are listed in Table 6.2. It can be observed that both the G-bands and D-bands shift to lower domain after drafting with GPTS and blockers.

Table 6. 1. Summary table of D-Band and G-Band across biomaterial immobilization stages.

Stages	0	I	II	III	IV
D Band (cm^{-1})	1327.8	1326.1	1329.6	1331.3	1326.1
G Band (cm^{-1})	1582.0	1579.4	1588.1	1587.2	1582.9

The shift to lower frequency was certainly not caused by the heating and sonication process but by the GPTS and blocker functionalization [151]. The observed change of G-band can be explained by considering the chemical and physical properties of the adsorbed GPTS and blockers on the MWNTs. As GPTS and blocker are long chain epoxy and elastic polymers, they are attached onto the CNT surface through the hydrophobic and van der Waals attraction forces [148]. These elastic epoxy/polymers behave as a buffer layers and have significant damping effects during vibration caused by the Raman laser, hence the result is reflected in the lower frequency shift of Raman peak.

In contrast, the shift to higher frequency regions of G-bands after immobilizing goat IgG and anti-goat IgGs demonstrated the attachment of antigen and antibody to

Chapter 6 Development of CNT enhanced piezoelectric biosensor array

the GPTS-CNTs, which could increase the elastic constant of GPTS–MWCNTs for the shift [148]. In addition, the D-band in spectrum also shifted to the higher frequency accordingly, which could imply that antigen and antibody were covalently attached to GPTS-functionalized MWCNTs [152]. This is reasonable because goat IgG and anti-goat IgGs are expected to bond with the functionalized CNTs via the opened epoxy ring and antigen-antibody coupling.

Both for defect and graphic band, there is no significant peak intensity variation after drafting GPTS onto the pretreated CNT. However, the peak intensity after immobilizing goat IgG and blockers decreased significantly due to physical strain change in the graphite skeleton caused by the covalently bonded goat IgG [148,153]. After the anti-goat IgGs were captured in the last stage, a large peak intensity increase was observed. The increase in the intensity of the defect band can be attributed to an increased number of sp³-hybridized carbons in the nanotube framework and can be taken as a crude measure of the degree of functionalization [154, 155].

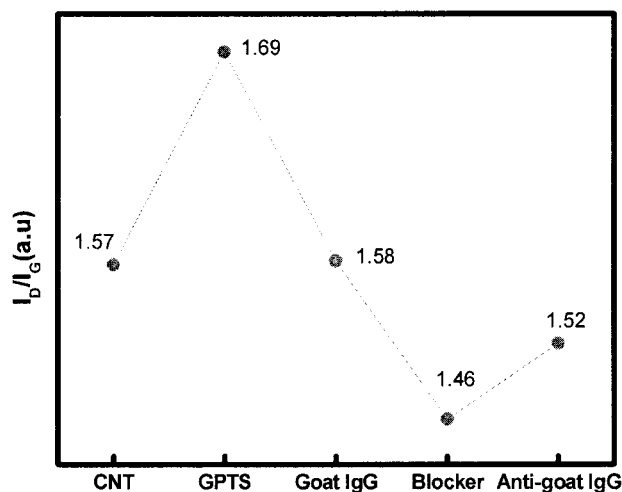


Figure 6.18. Peak intensity Raman ratio (I_D/I_G) across biomaterial immobilization stages.

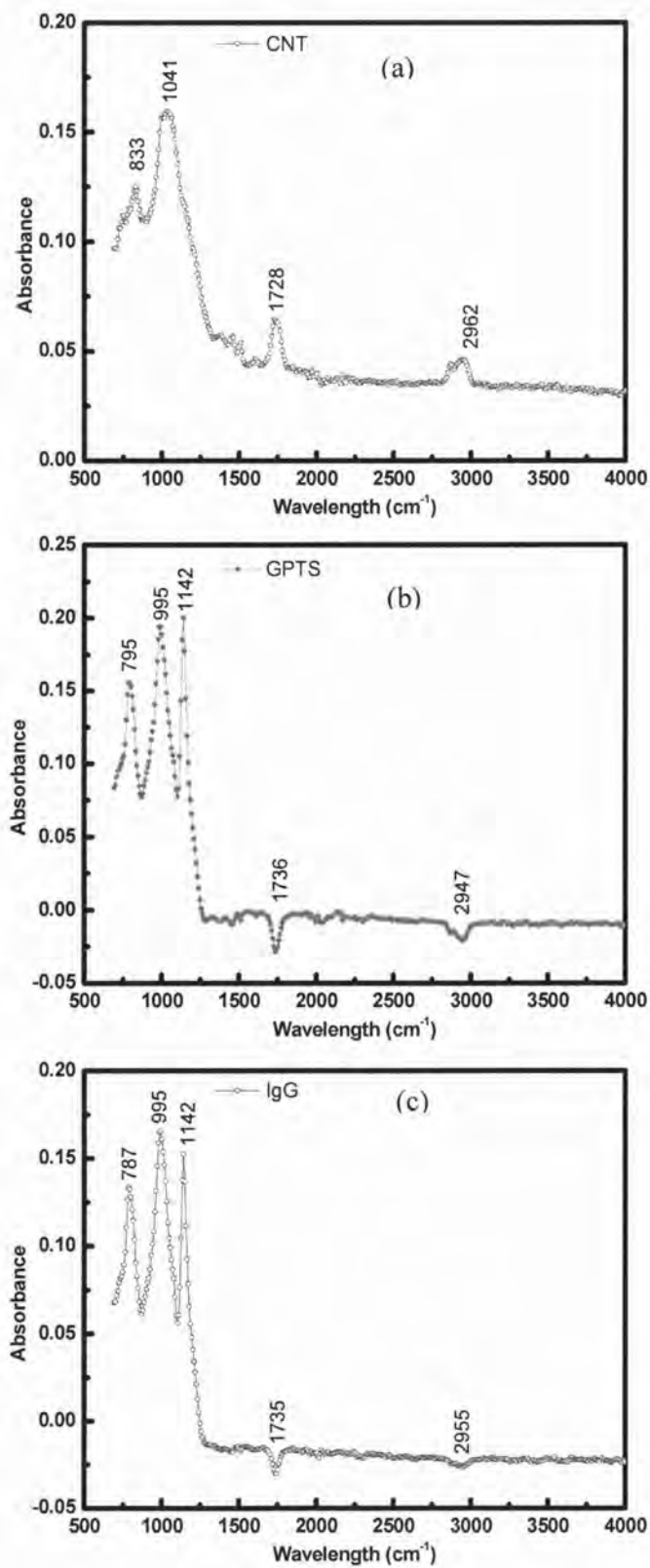
The ratio (I_D/I_G) between the intensity of the D-band and the G-band is related to the degree of disorder of the CNT and is sensitive to the chemical processing. The highest I_D/I_G value occurs after immobilizing GPTS (Figure 6.18), which is attributed to the presence of more structural defects. Some of the CNT bonds were broken and the caps were also opened during the HNO_3 oxidation, the epoxy (GPTS) may have been inserted into the tubes which can be interpreted as defects on the structure [156]. As shown in the above figure, there is an increasing shift in the last step where chemical interactions took place. This covalent bonding process can produce some end products that affect the graphitic structure and amount of defects.

(vi) ATR-FTIR characterization of functionalized CNTs

Attenuated Total Reflection Fourier Transform Infrared Spectroscopy (ATR-FTIR) was used to confirm the sequential steps of the functionalization. As a silicon oxide wafer was used as the substrate during the characterization process (Figure 6.19), the peak represented Si-O ideally should be the same for all the processes. However, due to the multiple treatments, chemical or biological interactions between the different biomaterials, such as GPTS, proteins or blockers, each process became relatively complex, hence, peaks have slight variations. In a conclusion, the first peak from 786 to 833 cm^{-1} showed in the different measured spectrums should be assigned to Si-O bond [157].

In the spectrum shown in Figure 6.19, a consistent peak repeat around 1735 cm^{-1} was due to the C=O from the HNO_3 treated CNTs [159]. It is known that the CNTs oxidized by HNO_3 could open the tube ends and bare polar hydrophilic groups (–COOH, C=O, –OH) on its surface [158]. Figure 6.19 (a) shows the first spectrum for treated CNTs peaks at 1041 and 2962 cm^{-1} were assigned to be C=C. The valley between 2950 and 3200 cm^{-1} indicates the formation of strongly H-bonded NH and OH molecular groups in IgG with CNT [162]. More over, C-N bond stretch vibrations appear at 1033 cm^{-1} . The presence and location of the NH, CN and OH bands suggest that the epoxy ring in GPTS was opened and reacted with the NH_2 groups from the immobilized IgGs.

Chapter 6 Development of CNT enhanced piezoelectric biosensor array



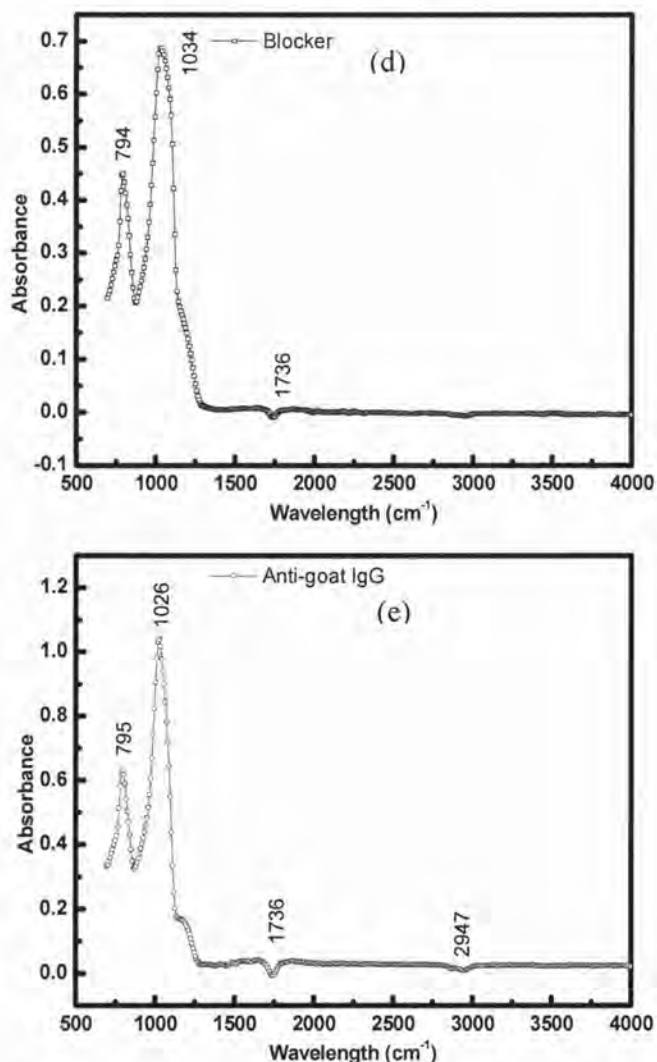


Figure 6.19. ATR-FTIR spectrum across different biomaterial immobilization stages, (a) acid treated CNT, (b) CNTs coated with GPTS, (c) goat IgG bond onto the GPTS draft CNT, (d) blocker added into CNT-GPTS-IgG composite, (e) anti-goat IgG captured by CNT composite.

Comparing Figure 6.19 (d) with (c), no band at 1141 cm⁻¹ in Figure 6.19 (d) indicates that CH₃ is not present in this process. The explanation for this is that CH₃ group was blocked or non-covalent binding by the blockers. In addition, the valley in the range of 2950-3200 cm⁻¹ was depolarized due to the NH or OH groups being blocked by the blockers. In the last process, the spectrum (Figure 6.19 (e)) was

Chapter 6 Development of CNT enhanced piezoelectric biosensor array

quite similar to that shown in the blocking process beside the amplitude. The amplitude of the valley in the range of 2950-3200 cm^{-1} was enhanced and this may be due to the blockers binding to the NH or OH groups being washed away during the immobilization process.

(vii) Resonant frequency measurement

Due to the mass sensitive nature of the PZT biosensor, the resonant frequency decreased after the external bio-entities were captured because the extra weight was added on the piezoelectric sensing surface. In order to have a detailed study on this relationship, the resonant frequencies of the sensors were measured after each immobilization or reaction process. To achieve more accurate results, all the measurements were constantly conducted in gas phase with a temperature of 30 °C. The frequency was measured by an Agilent impedance analyzer together with a probe station after each process. After each immobilization, frequency depression among the sensor array varied from 2500 to 3500 Hz and 950 to 1500 Hz for the sensor array with and without CNTs, respectively. Detailed frequency shifts after immobilizing goat IgGs, blocker and anti-goat IgGs are presented in Figure 6.20. The concentration of the added anti-goat IgG is 100 ng/ml. It is clear that the sensor with CNTs has a much larger frequency shift for the same immobilization process. This can be explained by the fact that more antigens were absorbed by the CNT-modified sensing diaphragm in the first step, resulting in much more available binding sites to catch the antibody in the last process.

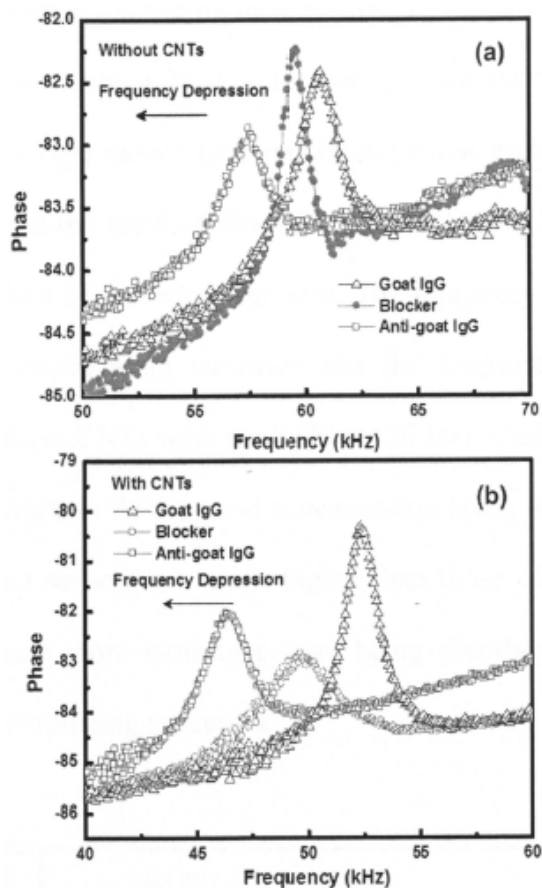
Chapter 6 *Development of CNT enhanced piezoelectric biosensor array*

Figure 6.20. Detailed frequency shift of the two sensor array (a) without CNTs, (b) with CNTs after each immobilization processes.

Therefore, at the same concentration, a larger frequency shift is observed as compared with the sensor without CNT. In Figure 6.20 (a), the frequency depression after adding a high concentration of blocker is smaller than that of after capturing anti-goat IgGs. This indicates that the amount of successful bonded blocker was relatively small, in another words, majority of the surface was occupied by the goat IgGs. However, in Figure 6.20 (b), frequency depression after adding blocker is larger than that of the plain one, which is attributed to certain amounts of blockers being dispersed into the hollow CNT tubes.

Chapter 6 Development of CNT enhanced piezoelectric biosensor array

The calibration curves for the frequency shifts versus concentration of HBsAg and AFP are shown in Figure 6.21. The frequency shifts plotted in the figure were obtained from the average values of 5 measurements at each concentration point and the error bars were the standard deviation of 3 replicates. The data was plotted with the average values of five measurements. The frequency depression increases the anti-goat IgG concentration increases and the frequency changes for both sensors with and without CNTs were negligible (<50 Hz) when the concentration of anti-goat IgG was 0 ng/ml/. At the same concentration level, the frequency changes of the CNT-enhanced sensors are much higher than those of the sensors without CNTs. This is because more molecules were being absorbed or captured by the CNTs during the immobilizing processes.

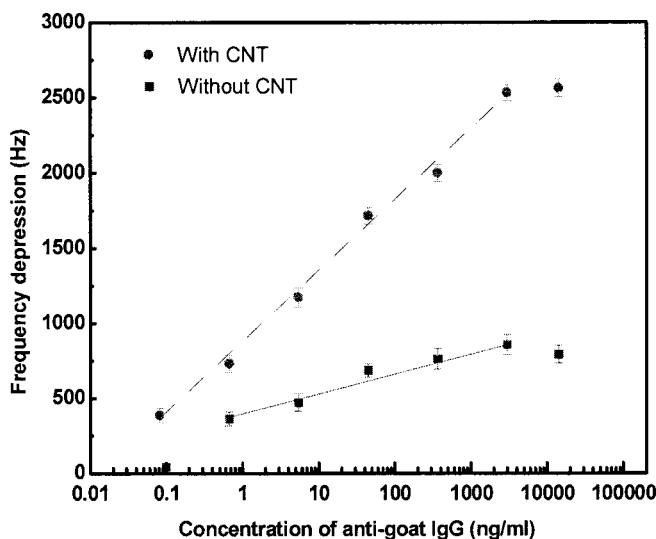


Figure 6.21. Relationship between the frequency depression (Hz) and concentration of the added anti-goat IgG (ng/ml).

The curves are linear in the range from 0.1 to 100000 ng/ml for both of HBsAg

Chapter 6 Development of CNT enhanced piezoelectric biosensor array

and AFP with a determination limit of 0.1 ng/ml, which is 200 times lower than that by QCM [163]. It can be observed that when the concentrations of anti-goat IgG are higher than 10 $\mu\text{g/ml}$; the frequency shifts tend to be saturated as the binding sites in the antigens are fully occupied by the antibodies. This is a typical immunoassay characteristic. This reveals that developed immunochip can sensitively detect goat anti-body in the range of 0.1 - 10000 ng/ml with reasonable standard deviations. At the same concentration level, the frequency changes of the CNT-enhanced sensors are much higher than those of the sensors without CNTs. This is because of more molecules being absorbed or captured by the CNTs during the immobilizing processes. Since the total 3-D sensing surface area of the CNT modified sensors can't be calculated precisely due to the nano size and the uncountable number of the deposited CNTs, Eq. 3.43 is not applicable to estimate the mass sensitivity of CNT enhanced biosensors. However, the mass sensitivity of the sensors without CNTs can be calculated bases on Eq. 3.43 and the known parameters. The diameters of the used sensors without CNTs are 0.6 mm and the resonant frequency before capturing anti-goat IgG, sensing surface area and S_M are 59.5 kHz, 0.28 mm^2 and -45.33 m^2/kg , respectively; hence, the mass sensitivity of sensors is calculated to be 9.63 Hz/ng. From the results presented in Figure 6.21, bases on the average gradient of the two linear curves, the sensitivity of CNT enhanced biosensor is about 3.5 times higher than that without CNTs. Therefore, the sensitivity of the biosensor with CNT enhancement is estimated to be 33.7 Hz/ng, in which is more than 5 times higher than the square diaphragm based biosensors reported in Chapter 4.

6.4 Summary of this chapter

In summary, a novel micro-fabricated CNT enhanced piezoelectric immunochip was demonstrated to be able to detect anti-goat IgG with multiple concentrations. During detection, a clear frequency depression was observed and the frequency depression among the sensor array varied from 2500 to 3500 Hz. The CNT-incorporated immunochip possesses a detection limit of 0.1 ng/ml and a dynamic range of 0.1 to 10000 ng/ml for the detection of Anti-goat IgG, whereas the detection limit and dynamic range for a non-CNT enhanced immunosensor chip are 1 ng/ml and 1 to 10000 ng/ml, respectively. In addition, the sensitivity of a CNT-incorporated biosensor is nearly 4 times higher than that of without CNT enhancement. The results demonstrate that the developed CNT-enhanced piezoelectric immunochip has significant advantages over the conventional one. For demonstration purposes, anti-goat IgG was used as the target analyte, in fact, other analytes, such as HBV and AFT, can be detected by changing the probe molecules. The preliminary results present in this work demonstrated that the developed device can potentially be used for disposable immunosensor chip for rapid and multiple detections with low cost.

Chapter 7

Conclusions and recommendations

In this last chapter, conclusions and recommendations are provided. Two novel designed and fabricated piezoelectric diaphragm-based biosensor arrays, and one CNT enhanced biosensor chip were developed in this project. The research work has been done and the major contributions during this project are concluded in details in section 7.1. The recommendations of further study beyond this thesis in future are also outlined in section 7.2.

7.1 Contributions

In this thesis, a comprehensive study including the theoretical analysis, finite element analysis, fabrication optimization, characterization on the micro-piezoelectric diaphragm-based biosensor array was carried out. The main contributions are summarized in the following points:

- A novel equation for resonant frequency of the micro-machined diaphragms works in a mixed mode of tension, and flexural rigidity is established based on the classic plate theory. Due to the complexity of the micro-fabrication process, the residual stress is unavoidable after the fabrication. Hence, both tension and

stiffness are interacting simultaneously in the micro-sensors. Since there is no mixed mode model available till today, an alternative equation is derived to describe the vibration behavior of the mixed mode of tension and flexural rigidity. The gravimetric sensitivity is also deduced based on the derived mixed mode resonant frequency equation and the results shows that it is independent of the tension and flexural rigidity. It is only determined by the total thickness of the diaphragm and the effects of T or D on the sensor are solely exhibited in the resonant frequency f_0 . This significant result reveals that the troublesome issue of checking the specific resonant behavior of the fabricated diaphragm can be avoided. Based on the gravimetric sensitivity, mass sensitivity is also defined. The derived equation is confirmed by the finite element analysis. The study shows that the diaphragm in the sensor should be designed to be thin and small with low density to achieve high sensitivity. By considering the sensitivity and difficulty of biomaterial immobilization, the designed diaphragm diameter varies from 600 μm to 1000 μm with a thickness of about 1 μm .

- Two novel micro-fabricated piezoelectric diaphragm-based immuno-biosensor chips were developed. The first square sensor array successfully detected anti-goat IgG with mass sensitivity of 6.25 Hz/ng. The preliminary results obtained from this chip confirm the possibility of applying these micro-piezoelectric sensors for biosensing applications. The second circular-type sensor array was developed to increase the sensitivity and the fabrication yield. After optimizing the fabrication and immobilization processes, it was demonstrated that the sensor chip was able to simultaneously detect HBsAg, AFP and HBcAg. A clear

frequency depression was observed and the frequency depression among the sensor array varied from 600 to 800 Hz. The biosensor chip can provide a real determination of HBsAg and AFP with the limit of detection of 0.1 ng/ml in the concentration range of 0.1 to 10000 ng/ml. The sensitivity for detection of HBsAg and AFP was found to be 16.05 Hz/ng and 15.97 Hz/ng, respectively. The gravimetric sensitivity ($-45.33 \text{ m}^2/\text{kg}$) is more than two times higher than that obtained from the square sensor array.

- A systematic and comprehensive study on the influences of various synthesis parameters on the growth of CNT by TCVD. In particular, the effects of pressure, process gas flow rate, growth temperature, growth time, catalyst pretreatment time and catalyst thickness on the overall vertical length of CNT and the quality of CNT were investigated in detail. Vertically-aligned CNTs grown on iron-deposited silicon oxide substrates were characterized by SEM, Raman Spectroscopy and TEM. It was found that both the length and quality of the CNT were affected by the synthesis parameters studied. The overall vertical length and quality of the CNT can be reliably controlled by varying either the growth temperature or C_2H_2 gas flow rate. In addition, the catalyst pretreatment time and temperature also played an important role in controlling the size and density of catalyst particles, which will in turn affect the length and density of the grown CNT. A high quality of long CNT with length up to 380 μm was successfully synthesized based on the optimized parameters. The optimized parameters for TCVD system were used for synthesizing CNTs either directly or deposited on the PZT diaphragm to enhance the performance of the

biosensors.

- Two novel approaches were implemented to develop CNT enhanced piezoelectric biosensors. In the first approach, CNTs were directly grown from the sensor diaphragm. Aligned dense CNTs were successfully synthesized. Unfortunately, most of the top and bottom electrodes in the sensors were peeled off from the substrate due to the high temperature during the CNT growth process, which makes this method impractical for the development of CNT based biosensors. Hence, in the second approach, CNTs were pre-synthesized by TCVD. Afterwards, functionalized CNTs were applied into the reaction chambers in the sensors. Immobilization methods were optimized and the CNT-enhanced biosensors were characterized by FSEM, AFM, Raman spectrum, AT-FIR and impedance analyzer. The developed CNT-incorporated immunochip possesses a detection limit of 0.1 ng/ml and a dynamic range of 0.1 to 10000 ng/ml for the detection of Anti-goat IgG, whereas the detection limit and dynamic range for a non-CNT-enhanced immunosensor chip are 1 ng/ml and 1 to 10000 ng/ml, respectively. In addition, the sensitivity of a CNT-incorporated biosensor is nearly 4 times higher than without CNT enhancement. The results demonstrate that the developed CNT-enhanced piezoelectric immunochip has significant advantages over the conventional one. For demonstration purposes, anti-goat IgG was used as the target analyte. In fact, other analytes, such as HBV and AFT, can be detected by changing the probe molecules. The preliminary results discussed in this chapter indicate that the CNT-enhanced micro-machined piezoelectric diaphragm-based biosensor has very compact size,

high sensitivity, high quality factor, rapid response and can potentially be used for disposable immunosensor with low cost. The preliminary results demonstrate that with further calibration and optimization, the developed piezoelectric immunochip has the potential of being applied in a disposable biochip for rapid and low cost medical diagnosis.

7.2 Future work recommendations

Although the CNT-enhanced piezoelectric diaphragm-based biosensor arrays were developed, the following works are still needed to be studied in future to make them practical for the disposable immunosensors applications.

- Micro-fluid channels need to be incorporated with the developed sensor chip. The dip-and-drop immobilization technique was implemented in this project. However, in the real application, the analytes favors a liquid environment even in the diagnosis process. Micro channels are required to be fabricated and integrated with the developed sensor chip so that the analyte solutions can flow through the micro-diaphragm continuously.
- Electrode design of the piezoelectric sensors needs to be modified if micro-channels are integrated with the sensor chip. The piezoelectric diaphragm worked in the flexural vibration mode in the dry condition during the testing; its quality factor and sensitivity will drop significantly in the liquid media. The electrodes need to be designed as inter-digital transducers, so that shear wave will be generated and propagate from one electrode to another one. The

liquid will have less or negligible impact on the sensor quality factor and sensitivity.

- Online resonant frequency monitoring software or system is required in future for the micro-channel integrated sensor chip. Because the fluids are continuously flowing through the micro-diaphragm, the resonant frequency changes with time as well as the external mass of the captured biomaterials, further study is demanded to develop the online frequency monitoring software or system.

Uniformity of the deposited CNTs needs to be improved. Due to surface tension, the deposited CNTs on the bottom of the micro-reaction chambers are not very uniform. This may affect the uniformity and repeatability of the individual sensors within the chip, hence further study is necessary to explore a new technique to deposit the CNTs uniformly on the bottom of the reaction chambers.

References

1. S. Li, Z. Li, B. B. Chin, and Z.-Y. Cheng, "Development of biosensor based on micro-diaphragm," *In Proceedings of SPIE*, vol. 5389, pp.306-313, 2004.
2. R. Bashir, "BioMEMS: state-of-the-art in detection, opportunities and prospects", *Advanced Drug Delivery Reviews*, vol. 56, pp. 1565, 2004.
3. J. A. Misewich, R. Martel, P. H. Avouris, J. C. Tsang, S. Heinze, and J. Tersoff, "Electrically induced optical emission from a carbon nanotube FET". *Science*, vol. 300, pp. 783, 2003.
4. M. Freitag, J. Martin, A. Misewich, R. Martel, and P. H. Avouris, "Photoconductivity of single carbon nanotube". *Nano Letters*, vol. 3, pp. 1067, 2003.
5. K. Ramanathan, M. Rank, J. Svitel, A. Dzgoev and B. Danielsson. "The development and applications of thermal biosensors for bioprocess monitoring", *Trends in biotechnology*, vol. 19, pp.499, 1999.
6. Janshoff, A., Galla, H .J. and Steinem, C., 2000. *Angewandte Chemie International Edition* 39 4004-4032.
7. MEMS 1999, Emerging applications and Markets, System Planning Corporation, 1999.
8. M. Meyyappan, "Carbon nanotubes: Science and Applications", CRC Press, 2005.
9. M. O'Connell, "Carbon Nanotubes: Properties and Applications", Taylor & Francis Group, LLC, 2006.
10. P. M. Ajayan, "Nanotubes from Carbon. Chem. Rev", Vol. 99. pp: 1787-1799, 1999.
11. M. Monthieux and V.L. Kuznetsov, "Who should be given the credit for the discovery of carbon nanotubes?", *Carbon*, Vol. 44, pp: 1621–1623, 2006.

12. N. Grobert, "Carbon nanotubes – becoming clean", *Materials Today*, Vol. 10, pp: 28, 2007.
13. Y.T. Lee, J. Park, Y.S. Choi, H. Ryu, and H.J. Lee, "Temperature-dependent growth of vertically aligned carbon nanotubes in the range 800-1100°C", *J. Phys. Chem. B*, Vol. 106, pp: 7614 – 7618, 2002.
14. H.J. Jeong, Y.M. Shin, K.S. Kim, S.Y. Jeong, Y.S. Park, Y.C. Choi, and Y.H. Lee, "Temperature and time dependence of the growth of carbon nanotubes by thermal chemical vapor deposition", *AIP Conf. Proc*, Vol. 590, pp: 35, 2001.
15. A. Gupta, D. Akin, and R. Bashir, "Single virus particle mass detection using microresonators with nanoscale thickness", *Appl. Phys. Lett.*, vol. 84, pp. 1976-1978, 2004.
16. Y. Lee, G. Lim, and W. Moon, "A self-excited micro cantilever bio sensor actuated by PZT using the mass micro balancing technique", *Sensors and Actuators A*, Vol 130-131, pp. 105-110, 2006.
17. A. Arnau. "Piezoelectric Transducers and applications", Springer, 2004.
18. Ryszard M. Lee. "Piezoelectric Biosensors: Recent Advances and Applications", *IEEE, International Frequency Control Symposium and PDA Exhibition*, pp. 419, 2001.
19. M. Haug, K.D. Schierbaum, G. Gauglitz and W. Gopel. "Chemical sensors based upon polysiloxanes comparison between optical, quartz microbalance, calorimetric, and capacitance sensors", *Sensors and Actuators B*, vol. 11, pp. 383, 1993.
20. L .Yu, W.Chen, M.Ashok, "Microbial biosensors", *Analytica Acta*, vol.568, pp.200, 2006.
21. P. B Lupaa, L. J Sokoll, D. W Chan. "Immunosensors—principles and applications to clinical chemistry", *Clinical Chimca Acta*, vol. 314, pp.1, 2001.

22. Saraju P. Mohanty, "Biosensors: A Survey Report", University of South Florida Tampa, FL 33620, USA.
23. J. Justin Gooding. "Biosensor technology for detecting biological warfare agents: Recent progress and future trends", *Analytica Chimica Acta*, vol. 559, pp.137, 2006.
24. A. Kumar. "Biosensors Based on Piezoelectric Crystal Detectors: Theory and Application", *The Minerals, Metals & Materials Society*, vol. 52, pp.10, 2000.
25. L. Conte, C. Chothia, J. Janin: "The atomic structure of protein-protein recognition sites", *Journal of molecular biology*, vol. 285, pp.2177, 1999.
26. Y. Li, H. Li, S. J. Smith-Gill, and R. A. Mariuzza, "Three-Dimensional Structures of the Free and Antigen-Bound Fab from Monoclonal Antilysozyme Antibody HyHEL-63", *Biochemistry*, vol. 39, pp.6296, 2000.
27. E. A. H. Hall, "Biosensors", Open University press, 1990.
28. J.M. Cabral, J. F. Kennedy, "Protein immobilization fundamentals and applications", R. F. Taylor (Ed.), Marcel Dekker, New York, 1991.
29. H. H. Weetall, "Covalent coupling methods for inorganic support materials", *Methods in Enzymology*, vol.44, pp.134, 1976.
30. N. Zhang, Carbon nanotubes based functional materials for MSL and Biosensor applications" PhD thesis, The Pennsylvania state university, 2005.
31. U. bilitewski, P.Ruger,R.D.Schmid, *Biosensors and bioelectronics*, vol.6, pp.369,1991.
32. T. Yao, "A Chemically-Modified Enzyme Membrane Electrode as an Amperometric Glucose Sensor", *Analytical Chemical Acta*, vol.148, pp.27, 1983.
33. A.P.F. Turner, "Current Trends in Biosensor Research and Development," *Sensors Actuators*, vol. 17, pp. 433, 1989.

34. R. Raiteri, M. Grattarola, H. Butt, P. Skladal. "Microcantilever based biosensor", *Sensors and Actuators B*, vol. 79, pp.115, 2001.
35. L.G. Carrascosa, M. Moreno, M. A. Lvarez, L.M. Lechuga, "Nanomechanical biosensor: A new sensing tool", *Trends in Analytical Chemistry*, vol. 25, pp. 196, 2006.
36. G. Wu, R. H. Datar, K. M. Hansen, T. Thundat, R. J. Cote, and A. Majumdar, "Bioassay of prostate-specific antigen (PSA) using microcantilever", *Nature biotechnology*, vol. 19, pp.856, 2001.
37. B. Ilic, D. Czaplewski, H.G. Craighead, P. Neuzil, C. Campagnolo, C. Bat, "Mechanical resonant immunospecific biological detector", *Applied Physics Letters*, vol. 77, pp. 450, 2000.
38. F.M. Battiston, J. P. Ramseyer, H.P. Lang, M.K. Baller, Ch. Gerber, J.K. Gimzewski, et al, "A chemical sensor based on a microfabricated cantilever array with simultaneous resonance-frequency and bending readout, *Sensors and Actuators B*, vol. 77, pp.122, 2001.
39. D. R. Baselt, G. U. Lee, Richard J. Colton, "Biosensor based on force microscope technology", *Journal of vacuum science & technology*, vol. 14, pp.789, 1996.
40. H.F. Ji, "A novel self-assembled monolayer (SAM) coated microcantilever for low level caesium detection", *Chemical communications*, vol. 6, pp.457, 2000.
41. K. S. Hwang, J. H. Lee, J. Park, D. S. Yoon, J. H. Park, and T. S. Kim, "In-situ quantitative analysis of prostate-specific antigen (PSA) using nanomechanical PZT cantilever", *Lab on a chip*, vol. 4, pp. 547, 2004.
42. K. H. Lee, Y. D. Su, S. J. Chen, F. G. Tseng, G. B. Lee, K. Lee, "Microfluidic systems integrated with two-dimensional surface plasmon resonance phase

- imaging systems for microarray immunoassay”, *Biosensors and bioelectronics*, vol. 23, pp. 466, 2007.
43. G. Y. Kang , G. Y. Han, J. Y. Kang, I. H. Cho, H. H. Park, S. H. Paek, et, al, “Label-free protein assay with site-directly immobilized antibody using self-actuating PZT cantilever”, *Sensors and actuators B*, vol. 117, pp. 332, 2006.
44. C.K. O’Sullivan, G.G. Guilbault. “Commercial quartz crystal microbalances-theory and applications”, *Biosensors & Bioelectronics*, vol. 14, pp. 663, 1999.
45. Z. Ali. “Acoustic Wave Mass Sensors”, *Journal of Thermal Analysis and Calorimetry*, vol. 55, pp.397, 1999.
46. B. Zimmermann, R. Lucklum, P. Hauptmann, J. Rabe, S. Buttegenbach. “Electrical characterization of high frequency thickness shear mode resonators by impedance analysis”, *Sensors and Actuators B*, vol.6, pp.47, 2001.
47. E. Gizeli, C. Stevenson, J. Goddard and R. Lowes, “Acoustic Love plate sensors: comparison with other acoustic devices utilizing surface SH waves”, *Sensors and Actuators B*, vol.13, pp.638, 1993.
48. S.J. Martin, G.C. Frye, K.O. Wessendorf. “Sensing liquid properties with thickness shear mode resonators”, *Sensors and Actuators A*, vol. 44, pp.209, 1994.
49. C. Campbell Surface, “Acoustic Wave Devices for Mobile and Wireless Communications”, San Diego: Academic Press. 1998.
50. B. Drafts, “Acoustic wave technology sensors”, *IEEE Transactions on Microwave Theory and Techniques*, vol. 49, pp. 795, 2001.
51. I. Mannelli, M. Minunni, S. Tombelli, M. Mascini, “Quartz crystal microbalance (QCM) affinity biosensor for genetically modified organisms (GMOs) detection”, *Biosensors and bioelectronics*, vol. 18, pp. 129, 2003.

-
52. X. T. Mo, Y. P. Zhou, H. Lei, L. Deng, "Microbalance-DNA probe method for the detection of specific bacteria in water", *Enzyme microbial technology*, vol. 30, pp. 583, 2002.
 53. S. W Wenzel, R.M. White. "Analytic comparison of the sensitivities of bulk wave, surface wave and flexural plate wave ultrasonic gravimetric sensors", *Applied Physics Letters*, vol. 54, pp.1976, 1989.
 54. M. Lazerges, H. Perrot, N. Zeghib, E. Antoine, C. Comperec, "In situ QCM DNA biosensor probe modification", *Sensors and actuator B*, vol. 120, pp.329, 2006.
 55. C. Ayela, L. Nicu, "Micromachined piezoelectric membranes with high nominal quality factors in newtonian liquid media: A Lamb's model validation at the microscale", *Sensors and Actuators B*, vol. 123, pp. 860, 2007.
 56. L Nicu , M. Guirardel, F. Chambosse, P. Rougerie, S. Hinh, E. Trevisiol, et, al, "Resonating piezoelectric membranes for microelectromechanically based bioassay: detection of streptavidin-gold nanoparticles interaction with biotinylated DNA", *Sensors and Actuators B*, vol. 110, pp. 125-136, 2005.
 57. K.L. Choy "Progress in Materials Science 48 (2003) 57-170.
 58. R. Thomas et al. *Thin Solid Films* 443 (2003) 14-22.
 59. R. Thomas, D.C. Dube, *Jpn. J. Appl. Phys.* 36 (1997) 7337.
 60. Charles P. Poole, Jr., and Frank J. Owens. 2003. Introduction to nanotechnology, Wiley-interscience.
 61. M.A. Prelas, G. Popovici, and L.K. Bigelow, "Handbook of Industrial Diamonds and Diamond Films", Marcel Dekker, New York, 1997.
 62. H.W. Kroto, J. R. Heath, S. C. O'Brien, R. F. Curl and R. E. Smalley , "C₆₀: Buckminsterfullerene" *Nature*, 318, 162 (1985)
 63. B.T. Kelly, *Physics of Graphite*, Applied Science, London (1981).

64. M. Endo, S. Iijima, M. S. Dresselhaus, "Carbon Nanotubes", Elsevier, 1996.
65. S.B. Sinnott, R. Andrews, D. Qian and A.M. Rao, "Model of carbon nanotube growth through chemical vapor deposition", *Chemical Physics Letters*, vol. 315, pp. 25, 1999.
66. C. Liu, Y.C. Chen, Y. Tzeng, "Effects of carbon in sputter coated iron catalyst on the growth of vertically aligned carbon nanotubes on smooth silicon surfaces by thermal chemical vapor deposition", *Diamond Related Materials*, vol. 13, pp. 1274, 2004.
67. Y.Y. Kang, J. H. Heung, J. W. Kim, R. Lee, S. Gollapudi, S. Subramaniam, et, al, "Introduction to carbon nanotube and nanofiber smart materials", *Composites part B*, vol. 37, pp. 382,2006.
68. J. Wang, M. Musameh, "Carbon Nanotube/Teflon Composite Electrochemical Sensors and Biosensors", *Analytical Chemistry*, vol. 75, pp. 2075, 2003,
69. M. D. Rubianes, G. A. Rivas, "Carbon nanotubes paste electrode", *Electrochemistry Communications*", vol. 5, pp. 689, 2003.
70. F. Valentini, A. Amine, S. Orlanducci, M. Terranova, G. Palleschi, "Carbon Nanotube Purification: Preparation and Characterization of Carbon Nanotube Paste Electrodes", *Analytical Chemistry*, vol. 75, pp. 5413, 2003.
71. L. Gorton, "Carbon paste electrodes modified with enzymes, tissues, and cells", *Electroanalysis*, vol. 7, pp.23, 1995.
72. P. J. Britto, K. S.V. Santhanam, P. M. Ayajan, "Carbon nanotube electrode for oxidation of dopamine", *Bioelectrochemistry and Bioenergetics*, vol. 41, pp. 121, 1996.

-
73. J. J. Gooding, R. Wibowo, J. Q. Liu, W. Yang, D. Losic, S. Orbons, et, al, "Protein Electrochemistry Using Aligned Carbon Nanotube Arrays", *Journal of the American Chemical Society*, vol. 125, pp. 9006, 2003..
 74. M. J. Lobo, A. J. Miranda, P. Tunon, "Amperometric biosensors based on NAD(P)-dependent dehydrogenase enzymes", *Electroanalysis*, vol. 9, pp. 191, 1997.
 75. K. Besteman, J. Lee, F. Wiertz, H. Heering, C. Dekker, "Enzyme-Coated Carbon Nanotubes as Single-Molecule Biosensors", *Nano Letters*, vol. 3, pp.727, 2003.
 76. J. Wang, M. Musameh, Y. Lin, "Solubilization of Carbon Nanotubes by Nafion toward the Preparation of Amperometric Biosensor", *Journal of the American Chemical Society*, vol. 125, pp. 2408, 2003,
 77. J. J. Gooding, "Electrochemical DNA Hybridization Biosensors", *Electroanalysis*, vol. 14, pp. 1149, 2002,
 78. J. Wang, G. Liu, M. Jan, "Ultrasensitive Electrical Biosensing of Proteins and DNA: Carbon-Nanotube Derived Amplification of the Recognition and Transduction Events", *Journal of the American Chemical Society*, vol.126, pp. 3010, 2004.
 79. W. Weaver Jr., S.P. Timoshenko, D.H. Young, "Vibration Problems in Engineering", *John Wiley & Sons*, New Work, (1990).
 80. Eunki Hong, S.V. Krishnaswamy, C.B. Freidhoff, S. Trolrier-McKinstry, *Sensors and Actuators A*, 119, 520 (2005)
 81. Leissa W. Arthur, "Vibration of plates", *Acoustical Society of America*, (1993).
 82. S. P. Timoshenko and S. woinowsky-kringer *Theory of plates and shells*: McGraw-Hill 1959.
 83. S.W.Wenzel and R.M.White, *Appl.Phys.Lett.* 54,20 (1989).

-
84. Thundat, T, Wachter, EA, Sharp, SL, Warmack, RJ, *Appl. Phys. Lett.*, 66, 1695 (1995).
 85. Thundat, T, *Microscale Thermophysical Engineering*, 1, 185 (1997).
 86. Ilic, B, Czaplewski, D, Craighead, HG, Neuzil, P, Campagnolo, C, and Batt, C, *Appl. Phys. Lett.* 77, 450 (2000).
 87. Kazuki Kawata, Hiroyuki Sugimura and Osamu Takai, *Thin Solid Film*, Vol.390, Issues 1-2, (2001)
 - 88 Wang, Z., Zhu, W., Zhao, C., and Tan, O. K., 2003. *Materials Science and Engineering B* 99, 56-62.
 - 89 Zhu, W., Wang, Z., Zhao, C., Tan, O. and Hng, H., 2002. *Japanese Journal of Applied Physics*, 41, 6969-6975.
 - 90 Karyakin, A.A., Presnova, G.V., Rubtsova, M.Y., Egorov, A.M., 2000. *Analytical Chemistry* 72, 3805-3811.
 - 91 Lazcka, O., Campo, F.J.D., Munoz, F.X., 2007. *Biosens. Bioelectron* 22, 1205-1217.
 - 92 Tombelli, S., Mascini, M., 2000. *Analytical Letters* 33, 2129 – 2151.
 - 93 Ito, K., Hashimoto, K., Ishimori, Y., 1996. *Analytica Chimica Acta* 327, 29-35.
 - 94 S. Jiang, S.L. Nail “Effect of process conditions on recovery of protein activity after freezing and freeze-drying” *European Journal of Pharmaceutics and Biopharmaceutics* 45 (1998) 249–257.
 - 95 T. Arakawa, S.J. Prestrelski, W.C. Kenney, J.F. Carpenter, Factors affecting short-term and long-term stabilities of proteins, *Adv. Drug Del. Rev.* 10 (1993) 1–28.
 - 96 J.F. Carpenter, S.J. Prestrelski, T.J. Anchordoguy, T. Arakawa, Interactions of proteins with stabilizers during freezing and drying, in: J.L. Cleland, R. Langer

- (Eds.), Formulation and Delivery of Proteins and Peptides, American Chemical Society, Washington, DC, 1994, pp. 134–147.
- 97 Park, I.S., Kim, W.Y., Kim, N., 2000. *Biosens. Bioelectron* 15, 167-172.
- 98 Yao, S.Z., Zhou, T.A., 1988. *Analytica Chimica Acta* 212, 61-72.
- 99 Yang Xin, Zhimin Li, LeVar Odum, and Z.-Y. Cheng, Zhuo Xu, "Piezoelectric diaphragm as a high performance biosensor platform", *APPLIED PHYSICS LETTERS* 89, 223508, 2006.
- 100 Goran stemme, resonant silicon sensors, *journal of micromechanics and micromaching*, 1, pp. 113-125, 1991.
- 101 H. A. C. Tilmans, M. Elwenspoek, and J. H. J. Fluitman, "Micro resonant force gauges," *Sensors and Actuators A: Physical*, vol. 30, pp. 35-53, 1992.
- 102 K. Y. Yasumura, T. D. Stowe, E. M. Chow, T. Pfafman, T. W. Kenny, B. C. Stipe, and D. Rugar, "Quality factors in micron- and submicron-thick cantilevers," *Journal of Microelectromechanical systems*, vol. 9, pp. 117-125, Mar 2000.
- 103 Z. Hao, A. Erbil, and F. Ayazi, "An analytical model for support loss in micromachined beam resonators with in-plane flexural vibrations," *Sensors and Actuators A: Physical*, vol. 109, pp. 156-164, 2003.
- 104 K. L. Ekinici and M. L. Roukes, "Nanoelectromechanical systems," *Review of Scientific Instruments*, vol. 76, Jun 2005.
- 105 Ye, Y.K., Zhao, J.H., Yan, F., Zhu, Y.L., Ju, H.X., 2003. *Biosensors and Bioelectronics* 18, 1501-1508.
- 106 Shen, G., Wang, H., Tan, S., Li, J., Yu, R., 2005. *Analytica Chimica Acta* 540, 279-284.
- 107 Zhou, X., Liu, L., Hu, M., Wang, L., Hu, J., 2002. *Journal of Pharmaceutical and*

- Biomedical Analysis 27, 341-345.
- 108 Zhang, Y., Zhang, Z., Yang, F., 2007. Journal of Chromatography B 857, 100-107.
109. S.L. Zhan, Y.J. Tian, Y.B. Cui, H. Wu, Y.G. Wang, S.F. Ye, Y.F. Chen, "Effect of process conditions on the synthesis of carbon nanotubes by catalytic decomposition of methane", *China Particuology*, Vol. 5, pp: 213–219, 2007.
110. E. Terrado, E. Muñoz, W.K. Maser, A.M. Benito, M.T. Martínez, "Important parameters for the catalytic nanoparticles formation towards the growth of carbon nanotube aligned arrays", *Diamond & Related Materials*, Vol. 16, pp: 1082–1086, 2007.
111. R.E Morjan, O.A. Nerushev, M. Sveningsson, L.K.L. Falk, F. Rohmund E.E.B Campbell, "Parametric study of nanotube growth from C₂H₂ and C₆₀ on supported iron catalyst particles", AIP Conf. Proc., Vol. 633, pp: 186, 2002.
112. C.J. Lee, J. Park and J.A. Yu, "Catalyst effect on carbon nanotubes synthesized by thermal chemical vapor deposition", *Chem. Phys. Lett*, Vol. 360, pp: 250, 2002.
113. C. Klinke, J.-M. Bonard and K. Kern, "Comparative study of the catalytic growth of patterned carbon nanotube films", *Surf. Sci.*, Vol. 492, pp: 195, 2001.
114. Y.Y. Wei, Gyula Eres, V.I. Merkulov, D. H. Lowndes, "Effect of catalyst film thickness on carbon nanotube growth by selective area chemical vapor deposition", *Appl. Phys. Lett.*, Vol. 78, pp: 1394. 2001.
115. O.A. Nerushev, S. Dittmar, R.-E. Morjan, F. Rohmund, E.E.B. Campbell, "Particle size dependence and model for iron-catalyzed growth of carbon nanotubes by thermal chemical vapor deposition", *J. Appl. Phys.*, Vol. 93, pp: 4185, 2003.

-
116. A. Rizzo, R. Rossi, M.A. Signore, E. Piscopiello, L. Capodiecì, R. Pentassuglia, T. Dikonimos, R. Giorgi, "Effect of Fe catalyst thickness and C_2H_2/H_2 flow rate ratio on the vertical alignment of carbon nanotubes grown by chemical vapour deposition", *Diamond and Related Materials*, 2008.
117. H.C. Wen, K. Yang, K.L. Ou, W.F. Wu, R.C. Luo, C.P. Chou, "Carbon nanotubes grown using cobalt silicide as catalyst and hydrogen pretreatment", *Microelectronic Engineering*, Vol. 82, pp: 221–227, 2005.
118. C. Ducati, I. Alexandrou, M. Chhowalla, G. A. J. Amaratunga, J. Robertson, "Temperature selective growth of carbon nanotubes by chemical vapor deposition", *J. Appl. Phys.*, Vol. 92, pp: 3299, 2002.
119. H. Cui, G. Eres, J.Y. Howe, A. Puretkzy, M. Varela, D.B. Geohegan and D.H. Lowndes, "Growth behavior of carbon nanotubes on multilayered metal catalyst film in chemical vapor deposition", *Chem. Phys. Lett.*, Vol. 374, pp: 222-228, 2003.
120. S.A. Moshkalyova, A.L.D. Moreaub, H.R. Guttie´rrezb, M.A. Cottab, J.W. Swart, "Carbon nanotubes growth by chemical vapor deposition using thin film nickel catalyst", *Materials Science and Engineering B*, Vol. 112, pp:147-153, 2004.
121. C.J. Lee, J. Park, Y. Huh and J.Y. Lee, "Temperature effect on the growth of carbon nanotubes using thermal chemical vapor deposition", *Chem. Phys. Lett.*, Vol. 343, pp: 33, 2001.
122. O.A. Nerushev, R.E. Morjan, D.I. Ostrovskii, M. Sveningsson, M. Jonsson, F. Rohmund, E.E.B. Campbell, "The temperature dependence of Fe-catalysed growth of carbon nanotubes on silicon substrates", *Physica B*, Vol. 323, pp: 51–59, 2002.

-
123. A.Y. Cao, X.F. Zhang, C.L. Xu, J. Liang, D.H. Wu, X.H. Chen, B.Q. Wei, P.M. Ajayan, "Grapevine-like growth of single walled carbon nanotubes among vertically aligned multiwalled nanotube arrays", *Appl. Phys. Lett.*, Vol. 79, pp: 1252, 2001.
124. S.S. Fan, M.G. Chapline, N.R. Franklin, T.W. Tombler, A.M. Cassell, H.J. Dai, *Science*, Vol. 283, pp: 512, 1999.
125. Michael J. Bronikowski, "CVD growth of carbon nanotube bundle arrays", *Carbon*, Vol. 44, pp: 2822–2832, 2006.
126. H.P. Liu, G.A. Cheng, R.T. Zheng, Y. Zhao, C.L. Liang, "Layered growth of aligned carbon nanotubes arrays on silicon wafers", *Journal of Molecular Catalysis A: Chemical*, Vol. 247, pp: 52–57, 87, 2006.
127. H. Yan, Q.W. Li, J. Zhang, Z.F. Liu, "Possible tactics to improve the growth of single-walled carbon nanotubes by chemical vapor deposition", *Carbon*, Vol. 40, pp: 2693–2698, 2002.
128. W.Z. Li, J.G. Wen, Y. Tu, Z.F. Ren, "Effect of gas pressure on the growth and structure of carbon nanotubes by chemical vapor deposition", *Applied Physics A: Materials Science & Processing*, Vol. 73, pp: 259-264, 2001.
129. X.B. Wang, W.P. Hu, Y.Q. Liu, C.F. Long, Y. Xu, S.Q. Zhou, et al., "Bamboo-like carbon nanotubes produced by pyrolysis of iron (II) phthalocyanine", *Carbon*, Vol. 39, pp: 1533-6, 2001.
130. X.C. Zhou, S.J. Shea, S.F.Y. Li, "Amplified microgravimetric gene sensor using Au nanoparticle modified oligonucleotides", *Chem. Commun.* vol. 11, pp. 953-954, 2000.
131. S. Han, J. Lin, M. Satjapipat, A.J. Baca, F. Zhou, "A threedimensional heterogeneous DNA sensing surface formed by attaching oligodeoxynucleotide-capped gold nanoparticles onto a gold-coated quartz crystal", *Chem. Commun.* vol.

- 2, pp.609-610, 2001.
132. H.Q. Zhao, L. Lin, J.R. Li, J.A. Tang, M.X. Duan, L. Jiang, "DNA biosensor with high sensitivity amplified by gold nanoparticles", *J. Nanoparticle Res.* vol. 3, pp. 321-323, 2001.
133. P. Ramirez, "Carbon nanotubes for science and technology" *Bell Labs Tech J.* vol. 10, pp. 171-185, 2005.
134. J. H. He, S. Q. Sun, J. S. Ye, T. M Lim, "Self-Assembly Carbon Nanotubes on Cantilever Biosensor for Sensitivity", *J. Phys.: Conference Series*, vol. 34, pp. 423-428, 2006.
135. J. Wang, "Carbon-nanotube based electrochemical biosensors: A Review", *Electroanalysis*, vol. 17, pp.7-14, 2005.
136. Q. Zhao, Z. Gan, Q. Zhuang, "Electrochemical Sensors Based on Carbon Nanotubes", *Electroanalysis*, Vol. 14, pp.1609-1613, 2002.
137. M. Musameh, J. Wang, A. Merkoci, Y. Lin, "Low-potential stable NADH detection at carbon-nanotube-modified glassy carbon electrodes", *Electrochem. Commun.*, vol.4, pp. 743-746, 2002.
138. J. Wang, A. Kawde, M. Mustafa, "Carbon-nanotube-modified glassy carbon electrodes for amplified label-free electrochemical detection of DNA hybridization", *Analyst*, vol. 128, pp. 912-916, 2003.
139. T. Xu, Z. H. Wang, J. M. Miao, X. F. Chen, and C. M. Tan, "Aligned carbon nanotubes for through wafer interconnects", *Applied Physics Letters*, Vol. 91, pp. 042108, 2007.
140. Paul A. Heiney, Kirsten Grüneberg, and Jiyu Fang, Charles Dulcey and Ranganathan Shashidhar "Structure and Growth of Chromophore-Functionalized (3-Aminopropyl) triethoxysilane Self-Assembled on Silicon", *Langmuir*, 16, pp

- 2651-2657, 2000,
141. Sumanda Bandyopadhyay, P. P. De, D. K. Tripathy, S. K. De, 3-Aminopropyltriethoxysilane as a promoter in the crosslinking of carboxylated nitrile rubber by surface-oxidized carbon black, *Journal of Applied Polymer Science*, Vol. 61, pp.1813-1820,1996.
 142. K. Y. Wong, U.J. Krull, "Surface characterization of 3-glycidoxypropyltrimethoxysilane films on silicon-based substrates", *Anal Bioanal Chem*. Vol. 383, pp. 187-200, 2005.
 143. Mateo C, Abian O, Fern'andez-Lafuente R, Guisan JM. Reversible enzyme immobilization via very strong and non-distorting adsorption on supports polyethyleneimine composites. *Biotechnol Bioeng* 2000;68:98-105.
 144. Pessela BCC, Fernandez-Lafuente R, Fuentes M, Vian A, Garc'ia JL, Carrascosa AV, et al. Reversible immobilization of the thermophile-galactosidase via ionic adsorption on PEI-coated Sepabeads. *Enzyme Microb Tech* 2003;32:369-74.
 145. Bryjak J. Storage stabilization of enzyme activity by poly (ethyleneimine). *Bioprocess Eng* 1995;13:177-81.
 146. Lin Y, Rao A M, Sadanadan B, Kenik E A and Sun Y P, "Functionalizing Multiple-Walled Carbon Nanotubes with Aminopolymers", *J. Phys. Chem. B*. vol. 106, pp 1294-1298, 2002.
 147. Yu L, Li C M and Zhou Q, "Efficient probe immobilization on poly for sensitive protein detection, *Frontiers in Bioscience*, 10, 2848-2855, 2005.
 148. V.A. Sinani, M.K. Gheith, A.A. Yaroslavov, A.A. Rakhnyanskaya, K. Sun, A.A. Mamedov, et al., "Aqueous Dispersions of Single-wall and Multiwall Carbon Nanotubes with Designed Amphiphilic Polycations", *J. Am. Chem. Soc.* 127 (2005) 3463-3472.

-
149. A. Kukovecz, C. Kramberger, V. Georgakilas, M. Prato, H. Kuzmany, "A detailed Raman study on thin single-wall carbon nanotubes prepared by the HiPCO process", *Eur. Phys. J., B* 28 (2002) 223-230.
150. M. S. Dresselhaus, G. Dresselhaus, R. Saito and A. Jorio, 2005. Raman spectroscopy of carbon nanotubes. *Physics Report* 409: 47-99.
151. Yang D Q, Rochette J F and Sacher E "Functionalization of Multiwalled Carbon Nanotubes by Mild Aqueous Sonication", 2005 *J. Phys. Chem. B* 109 7788-7794.
152. Liu Y, Liang P, Zhang H Y and Guo D S, "Cation-controlled aqueous dispersions of alginic-acid-wrapped multi-walled carbon nanotubes", 2006 *Small vol.7*,pp. 874.
153. G.X. Chen, H.S. Kim, B.H. Park, J.S.Yoon, "Controlled functionalization of multiwalled carbon nanotubes with various molecular-weight poly(l-lactic acid)", *J. Phys. Chem. B* 109 (2005) 22237–22243.
154. Li Niu, Yanling Luo, Zhanqing Li A highly selective chemical gas sensor based on functionalization of multi-walled carbon nanotubes with poly(ethylene glycol), *Sensors and Actuators B* 126 (2007) 361-367.
155. Jeffrey L. Bahr and James M. Tour, "Highly Functionalized Carbon Nanotubes Using in Situ Generated Diazonium Compounds", *Chem. Mater.* **2001**, *13*, 3823-3824.
156. A.G. Osorio , I.C.L. Silveira, V.L. Bueno, C.P. Bergmann, H₂SO₄/HNO₃/HCl-Functionalization and its effect on dispersion of carbon nanotubes in aqueous media, *Applied Surface Science* 255 (2008) 2485–2489.
157. Iva Movre Sapic, Lahorija Bistricec, Vesna Volovsek, Vladimir Dananic, Kresimir Furic "DFT study of molecular structure and vibrations of 3-glycidoxypropyltrimethoxysilane", *Spectrochimica Acta Part A* 72 (2009) 833-

- 840.
158. A. Kukovecz, C. Kramberger, M. Holzinger, H. Kuzmany, J. Schalko, M. Mannsberger, A. Hirsch, "On the Stacking Behavior of Functionalized Single-Wall Carbon Nanotubes", *J. Phys. Chem. B* 106 (2002) 6374-6380.
159. Sobhi Daniel , Talasila Prasada Rao, Kota Sreenivasa Rao, Sikhakolli Usha Rani , G.R.K. Naidu, Hea-Yeon Lee, Tomoji Kawai "A review of DNA functionalized/grafted carbon nanotubes and their characterization, *Sensors and Actuators B* 122 (2007) 672–682.
160. S.G. Wang, R. Wang, P.J. Sellin, Q. Zhang, DNA biosensors based on self-assembled carbon nanotubes, *Biochem. Biophys. Res. Commun.* 325 (2004) 1433–1437.
161. R.N. Jana, H. Bhunia "Thermal stability and proton conductivity of silane based nanostructured composite membranes" *Solid State Ionics* 178 (2008) 1872–1878.
162. R.M. Badger, S.H. Bauer, Spectroscopic Studies of the Hydrogen Bond. II. The Shift of the O-H Vibrational Frequency in the Formation of the Hydrogen Bond *J. Chem. Phys.* 5 (1937) 839-851.
163. Zhang, B., Zhang, X., Yan, H.h., Xu, S.j., Tang, D.h., Fu, W.l., 2007. *Biosens. Bioelectron.* 23, 19-25.

Publication List

1. Ting Xu, Jianmin Miao, Zhihong Wang, Ling Yu and Chang Ming Li, "Micro-piezoelectric immunoassay chip for simultaneous detection of Hepatitis B virus and α -fetoprotein", *Sensors and Actuators B: Chemical*, 2010, in press.
2. Ting Xu, Jianmin Miao, Chang Ming Li, Yingshuai Liu, "Investigation of the Effect of Adsorption Induced Surface Stress on the Resonant Frequency of PZT Membrane based biosensors", *Journal of Nanoscience and Nanotechnology*, 2010, in press.
3. Jingyu Lu, Ting Xu, Jianmin Miao, "Temperature Control of Microheaters for Localized Carbon Nanotube Synthesis", *Journal of Nanoscience and Nanotechnology*, 2010, in press.
4. M. Olfatnia, V. R. Singh, T. Xu, J. M. Miao, and L. S. Ong, "Analysis of the vibration modes of piezoelectric circular microdiaphragms " *Journal of micromechanics and microengineering*, vol. 20, p. 085013, 2010.
5. M Olfatnia, Ting Xu, J M Miao, L S Ong and Z H Wang, "Investigation of residual stress and its effects on vibrational characteristics of piezoelectric based multilayered micro-diaphragms", *Journal of Micromechanics and Microengineering*. vol. 20, p. 5007, 2010.
6. M. Olfatnia, Ting Xu, Jianmin Miao, Linseng Ong, "Effect of non-uniform adsorption of proteins on the response of microdiaphragm based biosensors", *Sensor Letters*. vol. 8, pp. 258-261, 2010.
7. M. Olfatnia, T. Xu, J. M. Miao, L. S. Ong, X. M. Jing, and L. Norford, "Piezoelectric circular microdiaphragm based pressure sensors," *Sensors and Actuators A: Physical*, in press, 2010.
8. M. Olfatinal, Ting Xu, Ong Lin Seng, Jianmin Miao, "Micro-diaphragm resonating biosensors in high frequency modes", *Journal of Nanoscience and Nanotechnology*, 2010, in press.
9. X.M. Jing, J.M. Miao, T. Xu, M. Olfatnia, L. Norford, Vibration characteristics of micromachined piezoelectric diaphragms with a standing beam subjected to airflow, *Sensors and Actuators A: Physical*, accept, 2010.
10. Ting Xu, Jianmin Miao, Hui Li and Zhihong Wang, "Local synthesis of aligned carbon nanotube bundle arrays by using integrated micro-heaters for interconnect applications", *Nanotechnology*, Vol. 20, pp. 295303, 2009.
11. Ting Xu, Mohammed Ashraf, Jianmin Miao, Franck Chollet and Nay Lin, *Materials Letters*. Vol. 63, pp. 867-869, 2009.
12. Nay Lin, Wang Huili, Xu Ting, Pradeep Dixit, Jianmin Miao, "Study of multi walled carbon nanotubes growth on multi-metal layers for advanced interconnect applications in microelectronic devices". *Journal of the Electrochemical society*, Vol. 156, K23, 2009. This paper is also accepted by *Virtual Journal of Nanoscale Science & Technology*, Volume 19, Issue 14.
13. Ting Xu, Zhihong Wang, Jianmin Miao, "Fabrication of Carbon-Nanotube Enhanced Piezoelectric Membrane for biosensor application", *International Journal of Nanotechnology*. Vol.6, No.7/8 pp.762-771, 2009.

14. Ting Xu, Zhihong Wang, Jianmin Miao, Ling Yu, Changming Li, "Micro-machined piezoelectric membrane based immunosensor array", *Biosensors & Bioelectronics*, Vol. 24 pp. 638–643, 2008.
15. Zhihong Wang, Jianmin Miao, Chee Wee Tan, Ting Xu, "Fabrication of piezoelectric MEMS devices-from thin film to bulk PZT wafer", *Journal of electroceramics*, DOI 10.1007/s10832-008-9454-x, PP. 1573-8663. 2008.
16. Ting Xu, Zhihong Wang, Jianmin Miao, Xiaofeng Chen and C. M. Tan, "Aligned carbon nanotubes for through-wafer interconnects," *Applied Physics Letters*, Vol. 91, No. 4, pp. 042108, 2007. This paper is also accepted by *Virtual Journal of Nanoscale Science & Technology*, Volume 16, Issue 6.

Conference Paper:

1. Ting Xu, Mohammed Ashraf, Pradeep Dixit, Nay Lin, Jianmin Miao and Franck Chollet , "Regular nanopitched carbon nanotube array using nanosphere lithography for electronics applications" paper presented at *ICMAT 2007, Singapore 1-6, July 13, 2007*.
2. N Lin, Ting Xu, XF Chen, JM Miao, WK Wong, KC Teo, "The Influence of Buffer Layer on CNT Growth on Copper Thin Film for Microelectronic Devices" paper presented at *ICMAT 2007, Singapore, 1-6, July 13, 2007*.
3. Zhihong Wang, Jianmin Miao, Ting Xu, Ling Yu, Changming Li, and Xiaofeng Chen, "Biosensors Based on Flexural Mode Piezo-Diaphragm" presented at *Nano/Micro Engineered and Molecular Systems, 2008. NEMS 2008, 3rd IEEE International Conference, Sanya, Hainan, China, 6-9 Jan. 2008. Page(s):374–378*.
4. Ting Xu, Zhihong Wang, Jianmin Miao, and Xiaofeng Chen, "Through wafer interconnects by carbon nanotubes", presented at *Nano/Micro Engineered and Molecular Systems, 2008. NEMS 2008, 3rd IEEE International Conference Sanya, Hainan, China, 6-9 Jan. 2008. Page(s):471-475*.
5. Ting Xu, Zhihong Wang, Jianmin Miao, "Fabrication of Carbon-Nanotube Enhanced Piezoelectric Membrane-based Biosensor", presented in *IEEE International Nanoelectronics Conference (INEC), Shanghai, China, 24-27 March 2008*.
6. Ting Xu, Zhihong Wang and Jianmin Miao, "A Novel Growth Method of Aligned Carbon Nanotubes at Low Temperature by Integrated Micro-Heaters for Through-Wafer Interconnects", has been accepted as oral presentation by *The 58th Electronic Components and Technology Conference (ECTC), Lake Buena Vista, Florida, USA, May 27-30, 2008. Pages: 1395-1399*.
7. Ting Xu, Zhihong Wang, Jianmin Miao, Ling Yu, Changming Li, "Self-polarized piezoelectric biosensor array for multiple immunoassays applications" in *IEEE MEMS, Sorrento, Italy, January 25-29, 2009*.
8. Zhihong Wang, Ting Xu, Jianmin Miao, G. Barbastathis, and M. Triantafyllou, "Micromachined piezoelectric microphone with high signal/noise ratio", *The 15th International Conference on Solid-State Sensors, Actuators and Microsystems (Transducers 2009)*, June 21 - 25, Denver, Colorado, U.S.A., 2009.
9. Ting Xu, Zhihong Wang, Jianmin Miao, Yingshuai Liu, Changming Li, "A high sensitivity carbon nanotubes integrated PZT diaphragm-based immunosensor

- array”, *The 15th International Conference on Solid-State Sensors, Actuators and Microsystems (Transducers 2009)*, June 21 - 25, Denver, Colorado, U.S.A., 2009.
10. Jianmin Miao, Ting Xu, Zhihong Wang, Ling Yu and Chang Ming Li, “Micromachined Piezoelectric Biosensor Array”, *International Conference On MEMS 2009 (ICMEMS)*, in Chennai, India from 3 - 5 January, 2009.
 11. Olfatnia Mohammad, Ting Xu, Ong Lin Seng, Jianmin Miao, “Micro-diaphragm resonating biosensors in high frequency modes”, presented in *IEEE International Nanoelectronics Conference (INEC)*, Hong Kong, China, 3-8 January, 2010.
 12. Jingyu Lu, Ting Xu, Jianmin Miao, “Temperature Control of Microheaters for Localized Carbon Nanotube Synthesis”, presented in *IEEE International Nanoelectronics Conference (INEC)*, Hong Kong, China, 3-8 January, 2010.
 13. Ting Xu, Jianmin Miao, “Investigation of Influence of Synthesis Parameters on Length and Purity of the CNTs Grown by Thermal Chemical Vapor Deposition”, presented in *IEEE International Nanoelectronics Conference (INEC)*, Hong Kong, China, 3-8 January, 2010.
 14. Ting Xu, Jianmin Miao, Chang Ming Li, Yingshuai Liu, “Investigation of the Effect of Adsorption Induced Surface Stress on the Resonant Frequency of PZT Membrane based biosensors”, *5th IEEE International Conference on Nano/Micro Engineered and Molecular Systems (IEEE NEMS)*, Jan 20-23, 2010, Xiamen, China.
 15. Ting Xu, Jianmin Miao, Chang Ming Li, Yingshuai Liu, “GPTS Functionalized Carbon Nanotubes Integrated with PZT Sensors for Detection of Anti-goat IgG”, *5th IEEE International Conference on Nano/Micro Engineered and Molecular Systems (IEEE NEMS)*, Jan 20-23, 2010, Xiamen, China.
 16. M Olfatnia, Ting Xu, J M Miao, L S Ong, “Frequency Response of Piezoelectric Microdiaphragm Based Biosensor under Immobilization of Goat immunoglobulin G”, *5th Asia-Pacific Conference on Transducers and Micro-Nano Technology, University of Western Australia, Perth Western Australia, 6–9 July, 2010*.
 17. X. M. Jing, J. M. Miao, T. Xu, L. Norford, “Hair-like Airflow Sensing with Piezoelectric, Vibrating Diaphragm”, *The 9th Annual IEEE Conference on Sensors November 1-4, 2010, Hilton Waikoloa Village, USA*.